Maxim N. Popov

The $TiO_2(100)\|(0001)Al_2O_3$ interface

A density-functional study

Dissertation

written at the Montanuniversität Leoben,
Chair of Atomistic Modeling and Design of Materials

under supervision of
Univ. Prof. Dr. Dr. h.c. C. Draxl

Leoben, April 2013

Summary

Materials made of alternating thin layers of Al_2O_3 and TiO_2 are of high interest for industry and materials science. Present and potential applications of such materials include, e.g., optical coatings and multilayer optical windows, as well as hardness-enhanced multilayer films for high-temperature applications. Al_2O_3/TiO_2 laminates are even considered as a possible candidate to replace the SiO_2 films for gate dielectric applications in transistors. Despite the effort done to investigate TiO_2/Al_2O_3 interfaces using experimental methods, there is nothing reported in the existing body of literature about atomistic modeling of this interface. It is the primary goal of this work, thus, to fill this gap, and to stimulate further work in the atomistic investigation of TiO_2/Al_2O_3 interfaces, especially using first principles methods. The methodological basis of this work consists of density functional theory (DFT) and linear elasticity theory. The former is the standard method in computational solid-state physics and materials science for dealing with matter at the level of atoms, that allows to calculate electronic structure and related properties. The latter is a well established framework for description of strain, stress, and elasticity of materials at a macroscopic level. Using experimental data on the phase composition of the film and the epitaxial relationships of TiO_2 deposited on (0001) sapphire, a model of the interface is established. In order to cope with the lattice misfit between the substrate and the overlayer, the *stress balancing* method is introduced, that allows to minimize the total strain energy of a superlattice using linear elasticity theory. The local arrangement of atoms in the vicinity of the interface is obtained by atomic relaxation. The structural features of the optimized geometries are analyzed by means of radial- and angular-distribution functions. The values for the work of separation, for both the static and the relaxed case, are obtained. It is found that the maximal adhesion strength is achieved, when the stacking sequence that is intrinsic for TiO_2 along [100] and for Al_2O_3 along [001] is preserved across the interface. The electronic properties, including the spatial charge distribution, and the total, partial, and local densities of electronic states are investigated in detail. In order to investigate the mechanical properties of the system, the bulk modulus (B), the Young's modulus (E[001]), and the shear modulus (G(001)[010]) are calculated. The numerical values of these moduli are also estimated using the effective elastic constants within the framework of the Grimsditch-Nizzoli method.

Zusammenfassung

Materialien, die aus abwechselnden Lagen von Al_2O_3 und TiO_2 bestehen, sind von großem Interesse für Forschung und Technologie. Derzeitige und potentielle Anwendungen dieser Materialien umfassen zum Beispiel optische Schichten und mehrlagigen optische Fenster, sowie mehrlagige Schichten mit erhöhter Härte für Hochtemperaturanwendungen. Al_2O_3/TiO_2–Laminate gelten sogar als mögliche Kandidaten als Ersatz für Dünnschichten aus SiO_2 die als “Gate-Dielektrika” in Transistoren verwendet werden. Obwohl große Anstrengungen zur Untersuchung von Al_2O_3/TiO_2–Grenzflächen durch experimentelle Methoden unternommen wurden, gibt es in der bestehenden Literatur keine Berichte über die atomistische Modellierung einer solchen Grenzfläche. Es ist daher das oberste Ziel dieser Arbeit, diese Lücke zu schließen und weitere Arbeiten im Bereich der atomistischen Untersuchung von TiO_2/Al_2O_3–Grenzflächen anzuregen.

Die methodologische Grundlage dieser Arbeit bilden die Dichtefunktionaltheorie (DFT) und die lineare Elastizitätstheorie. Erstere ist die Standardmethode zur Berechnung der elektronischen Struktur in computerbasierter Festkörperphysik und Materialwissenschaften. Letztere ist ein etablierter Rahmen für die Beschreibung von Verzerrung, Spannung und Elastizität. Unter Benützung von experimentellen Daten für eine dünne, auf (0001) Saphir aufgewachsene TiO_2-Schicht, wie der Phasenzusammensetzung dieser Schicht und der epitaktischen Beziehungen, wird ein Modell für die Grenzfläche erstellt. Um die Gitterfehlanpassung zwischen Substrat und Überschicht zu behandeln, wird die Methode des *stress balancing* eingeführt, die es erlaubt, die gesamte Verzerrungsenergie des Supergitters im Rahmen der linearen Elastizitätstheorie zu minimieren. Die lokale Anordnung der Atome in der Nähe der Grenzfläche wird dabei durch atomare Relaxation bestimmt. Die strukturellen Eigenschaften der optimierten Geometrie werden mit Hilfe radialer und winkelabhängiger Verteilungsfunktionen analysiert. Die Werte der *work of separation* werden sowohl für den statischen als auch für den relaxierten Fall bestimmt. Es wird gezeigt, dass die stärkste Adhäsion dann erreicht wird, wenn die intrinsische Stapelfolge für TiO_2 entlang [100] und Al_2O_3 entlang [001] durch die Grenzfläche hindurch beibehalten wird. Verschiedene elektronische Eigenschaften werden berechnet, darunter die räumliche Ladungsverteilung und die totale, partielle und lokale elektronische Zustandsdichte. Um die mechanischen Eigenschaften zu untersuchen werden der Kompressionsmodul, der Elastizitätsmodul (E[001]) und der Schermodul (G(001)[010]) berechnet. Die Größe dieser Moduln werden auch mit Hilfe der effektiven elastischen Konstanten im Rahmen der Grimsditch-Nizzoli-Methode abgeschätzt.

Contents

1 Introduction **1**
- 1.1 Oxide-oxide interfaces . . . 1
- 1.2 The TiO_2-Al_2O_3 interface . . . 2
- 1.3 Structure of the thesis . . . 2

2 Hard coatings **5**
- 2.1 Introduction . . . 5
- 2.2 Important classes of hard materials . . . 5
- 2.3 The relationships between structure and properties . . . 8

3 Theoretical background **9**
- 3.1 Elasticity in solids . . . 9
  - 3.1.1 Introduction . . . 9
  - 3.1.2 Scalars, vectors, and tensors . . . 9
  - 3.1.3 Stress tensor . . . 13
  - 3.1.4 Strain tensor . . . 14
  - 3.1.5 Elasticity tensor . . . 18
- 3.2 Density functional theory . . . 21
  - 3.2.1 Approximations for E_{xc} . . . 24

4 The TiO_2-Al_2O_3 system **25**
- 4.1 Introduction . . . 25
- 4.2 Experimental data . . . 25
- 4.3 Bulk materials . . . 26
  - 4.3.1 Computational parameters . . . 26
  - 4.3.2 Al_2O_3 . . . 27
  - 4.3.3 TiO_2 . . . 28
- 4.4 Interface model . . . 29
- 4.5 Conclusions . . . 32

5 Stress balancing method **35**
- 5.1 Introduction . . . 35
- 5.2 One-dimensional case . . . 36

5.3 Three-dimensional case: slabs of equal thickness 37
5.4 Three-dimensional case: slabs of different thickness 39
5.5 Results 40
5.6 Conclusions 41

6 Optimization of the interface structure 43
6.1 Introduction 43
6.2 Results 43
  6.2.1 A first view 44
  6.2.2 Relaxation profiles 45
  6.2.3 Radial distribution functions 47
  6.2.4 Angular distribution functions 51
6.3 Conclusions 53

7 The work of separation 55
7.1 Introduction 55
7.2 Computation method 55
7.3 Results 56
7.4 Convergence studies 56
  7.4.1 Brillouin zone sampling 57
  7.4.2 Wavefunction expansion 57
  7.4.3 Thickness of slabs 59
7.5 Conclusions 65

8 Electronic structure 67
8.1 Introduction 67
8.2 Plane-averaged charge 67
8.3 Density of states 70
8.4 Löwdin charges 71
8.5 The effect of Hubbard U 75
8.6 Conclusions 76

9 Mechanical moduli 79
9.1 Introduction 79
9.2 Effective elastic constants of the superlattice 79
9.3 Polynomial fitting procedure 81
9.4 Bulk modulus 83
  9.4.1 Computational procedure 83
  9.4.2 Fitting the *ab initio* dataset 83
  9.4.3 Results and analysis 86
9.5 Young's modulus 86
  9.5.1 Computational procedure 87
  9.5.2 Fitting the *ab initio* dataset 87

9.5.3 Results and analysis 89
9.6 Shear modulus 91
9.6.1 Computational procedure 91
9.6.2 Fitting the *ab initio* dataset 92
9.6.3 Results and analysis 94
9.7 Conclusions 95

10 Summary and conclusions 97

A Elastic constants and crystal symmetry 99
A.1 General remark 99
A.2 Results for all crystal systems 100

Acknowledgement 103

List of Abbreviations 105

List of Figures 107

List of Tables 109

Bibliography 111

List of Publications 119

Chapter 1

Introduction

1.1 Oxide-oxide interfaces

Ceramic materials, which are mostly oxides, are among the oldest materials classes used by mankind. They have been extensively used to produce a variety of goods ranging from tableware to construction materials. Nowadays, in addition to the traditional use, the oxide-based materials are employed, e.g., in diverse protective coatings [1], and composite materials [2–5]. The development of modern experimental analytical techniques [6], as well as the theoretical advances, allows us to look at oxide materials from a new perspective. The phenomena taking place at oxide/oxide interfaces in composite materials have become a hot topic in research [7]. A range of materials of interest becomes wider and wider every year. To give an idea about oxide/oxide interfaces described in literature so far, a short overview is given below.

The structure of the NiO-ZrO_2 interface was investigated using electron energy loss spectroscopy (EELS) and Z-contrast scanning transmission electron microscopy (STEM) in [8–10]. A theoretical investigation of NiO(111)/(100)ZrO_2 is presented in [11]. A lot of work has been done on oxide/MgO interfaces. Sayle and colleagues [12] reported the results of force-field modelling of CaO/MgO, BaO/MgO, SrO/MgO interfaces. The results of the experimental and theoretical investigations of the $SrTiO_3$(100)/(100)MgO interface are reported in [13] and [14], respectively. The Fe_3O_4(111)/(111)MgO polar oxide interface is extensively studied by a range of experimental methods in [15], as well as theoretically [16]. The magnetic and electronic properties of NiO(001)/(001)MgO [17] and Fe_2O_3(0001)/(111)MgO [18] are calculated from first principles. The structure of the TiO_2/$LaAlO_3$ interface is presented in [19]. Calculations of the ZrO_2/SiO_2 interface are described in [20]. The interfaces of the oxide/Fe_2O_3 type drew the attention [21–24] of researchers due to their unique electronic and magnetic properties. One more favorite system of latest research is $LaAlO_3$/$SrTiO_3$

(LAO/STO), which is investigated in [25–28]. Stengel and Vanderbilt [29] developed a theory of polar discontinuities at (oxide/oxide) interfaces, and applied it to LAO/STO. A comprehensive overview of the latest successes in exploring the rich physics of oxide/oxide interfaces, and the emerging new materials based on oxide/oxide interfaces is given in [30].

1.2 The TiO_2-Al_2O_3 interface

Nanolaminate materials made of alternating thin layers of Al_2O_3 and TiO_2 are of high interest. Among the present and the potential applications of such materials are the production of optical coatings [31] and multilayer optical windows [32], and hardness-enhanced multilayer films for high-temperature applications [33]. It was also discovered that a $Al_2O_3/TiO_2/Al_2O_3$ thin film is a possible candidate to replace the SiO_2 thin films, used as a gate dielectric in transistors [34].

Significant experimental work has been done on materials with TiO_2/Al_2O_3 interfaces. Spectroscopic investigations of TiO_2/Al_2O_3 interfaces using x-ray absorption spectroscopy (XAS) and resonant photoemission spectroscopy (RPES) [35–37] showed the existence of Ti-O-Al cross-linking bonds, and interface-induced changes of the electronic structure. Huang and co-workers [38] reported high-resolution transmission electron microscopy (HR-TEM) results for rutile-TiO_2 thin film grown on a $(\bar{1}10\bar{2})$ Al_2O_3 substrate. A couple of interface features was noted in [38], important for understanding the interface at the atomic level: 1) a substantial similarity was discovered in the local atomic patterns of the substrate and the film; 2) it was found that the TiO_2 film had a large lattice misfit, which led to the generation of structural defects, like twins, misfit dislocations, and stacking faults. Structural similarities are also noted in [39] as a guiding motive, that defines the epitaxy of a TiO_2 thin film on the r-plane $((1\bar{1}02))$ of sapphire, as well as its phase. Despite the effort done to investigate the TiO_2/Al_2O_3 interfaces using experimental methods, there is nothing reported in the existing body of literature about atomistic modeling of the interface. It is the primary goal of this work, thus, to fill this gap, and to initiate further work in the atomistic investigation of the TiO_2/Al_2O_3 interfaces, using first principles methods. The properties studied in this work comprise the interface geometry and atomic stacking, adhesive properties, electronic properties, and mechanical moduli.

1.3 Structure of the thesis

The thesis has the following structure:

- Hard coatings: An introduction to hard coatings is given and some basic facts about these materials are reported.

- Theoretical background: The basic facts about tensors are introduced, and the foundations of the elasticity of solids are described. Further, density–functional theory, which is our framework for calculating the electronic structure, together with total energies, forces and stresses, is presented.

- The system: The experimental data of the real system (a TiO_2 thin film grown on (0001) sapphire) used as a prototype for atomistic studies is reported, and the epitaxial relationships and the atomic stacking are discussed.

- Stress-balancing method: A new general methond to cope with the lattice mismatch problem, derived from the principles of linear elasticity, is introduced.

- Optimization of the interface structure: An overview of the methods of optimization used in atomistic modelling is given. Then, the results of the atomic geometry optimization are presented and analyzed in terms of radial and angular distribution functions.

- Work of separation: The results of the work of separation obtained in the work are reported, and the effects of atomic stacking at the interface and ionic relaxation are discussed.

- Electronic structure: The spatial distribution of charge and the electronic structure are analyzed, and the influence of the interface is discussed.

- Mechanical moduli: The mechanical moduli for selected directions are evaluated. Moreover, a comparison to the moduli obtained using the concept of effective elasticity as introduced by Grimsditch and Nizzoli [40, 41] is made.

- Summary and conclusions: The work ends with a summary, conclusions, and suggestions for further work in the field.

Chapter 2

Hard coatings

2.1 Introduction

According to Ref. [42], a material, which can be sustainably used in given conditions, i.e., environment is said to be hard to those conditions. Thus, according to Ref. [42], hard materials can be classified as:

1. Tribologically hard: wear resistant, with low friction.
2. Optically hard: laser, and photonically inert.
3. Radiation hard: with high threshold energies for energetic particles such as gamma rays, neutrons, and beta particles.
4. Electrically hard: wide bandgap.

In our work the main focus is put on the tribologically or, in a broader sense, mechanically hard materials, used to coat cutting and forming tools, and, thus, hereafter such materials are referred to simply as hard materials. When the hardness of a substance is above 20 GPa it is considered as hard. If a material has hardness above 40 GPa it is called superhard, and materials with hardness, which exceeds the value of 80 GPa, are classified as ultra-hard ones [43].

2.2 Important classes of hard materials

One of the classifications of hard materials is based on the chemical bonding character [44]. In this context, three classes are distinguished: *metallic* hard materials (borides, carbides, and nitrides of transition metals), *covalent* hard materials (borides, carbides, and nitrides of Al, Si, and B, as well as diamond), and *ionic* (ceramic) hard materials (oxides of Al, Zr, Ti, and Be). Some of the properties of the most important hard materials are summarized in Tables 2.1-2.3. Comparison of the data allows to identify some qualitative trends, which relate the bonding type to the properties. For instance, the bulk modulus for ionic hard materials is the lowest among this three classes. The linear thermal (LTE) coefficients usually increase from covalent to metallic and to ionic materials.

Table 2.1: Properties of metallic hard materials [44].

Phase	Density [g/cm^3]	Melting point [^{o}C]	Hardness [HV]	E modulus [GPa]	Spec.el. resistivity [$\mu\Omega$ cm]	Thermal exp. coeff. 10^{-6} [K^{-1}]
TiB_2	4.50	3225	3000	560	7	7.8
TiC	4.93	3067	2800	470	52	8.0-8.6
TiN	5.40	2950	2100	590	25	9.4
ZrB_2	6.11	3245	2300	540	6	5.9
ZrC	6.63	3445	2560	400	42	7.0-7.4
ZrN	7.32	2982	1600	510	21	7.2
VB_2	5.05	2747	2150	510	13	7.6
VC	5.41	2648	2900	430	59	7.3
VN	6.11	2177	1560	460	85	9.2
NbB_2	6.98	3036	2600	630	12	8.0
NbC	7.78	3613	1800	580	19	7.2
NbN	8.43	2204	1400	480	58	10.1
TaB_2	12.58	3037	2100	680	14	8.2
TaC	14.48	3985	1550	560	15	7.1
CrB_2	5.58	2188	2250	540	18	10.5
Cr_3C_2	6.68	1810	2150	400	75	11.7
CrN	6.12	1050	1100	400	640	(2.3)
Mo_2B_5	7.45	2140	2350	670	18	8.6
Mo_2C	9.18	2517	1660	540	57	7.8-9.3
W_2B_5	13.03	2365	2700	770	19	7.8
WC	15.72	2776	2350	720	17	3.8-3.9
LaB_6	4.73	2770	2530	(400)	15	6.4

Table 2.2: Properties of covalent hard materials [44].

Phase	Density [g/cm^3]	Melting point [^{o}C]	Hardness [HV]	E modulus [GPa]	Spec.el. resistivity [$\mu\Omega$ cm]	Thermal exp. coeff. 10^{-6} [K^{-1}]
B_4C	2.52	2450	3-4000	441	0.5×10^6	4.5(5.6)
BN(cubic)	3.48	2730	~5000	660	10^{18}	-
C(diamond)	3.52	3800	~8000	910	10^{20}	1.0
B	2.34	2100	2700	490	10^{12}	8.3
AlB_{12}	2.58	2150	2600	430	2×10^{12}	-
SiC	3.22	2760	2600	480	10^5	5.3
SiB_6	2.43	1900	2300	330	10^7	5.4
Si_3N_4	3.19	1900	1720	210	10^{18}	2.5
AlN	3.26	2250	1230	350	10^{15}	5.7

Table 2.3: Properties of ionic (ceramic) hard materials [44].

Phase	Density [g/cm^3]	Melting point [^{o}C]	Hardness [HV]	E modulus [GPa]	Spec.el. resistivity [$\mu\Omega$ cm]	Thermal exp. coeff. 10^{-6} [K^{-1}]
Al_2O_3	3.98	2047	2100	400	10^{20}	8.4
Al_2TiO_5	3.68	1894	-	13	10^{16}	0.8
TiO_2	4.25	1867	1100	205	-	9.0
ZrO_2	5.76	2677	1200	190	10^{16}	11(7.6)
HfO_2	10.2	2900	780	-	-	6.5
ThO_2	10.0	3300	950	240	10^{16}	9.3
BeO	3.03	2550	1500	390	10^{23}	9.0
MgO	3.77	2827	750	320	10^{12}	13.0

2.3 The relationships between structure and properties

The macroscopic properties of materials are tightly connected to their structure (electronic, atomic, and microstructure), thus the investigation of structure/property relationships plays the central role in material science [42]. So, the hardness of a material is dictated by its intrinsic hardness, i.e., the characteristic hardness of single-crystal bulk of the material, and by microstructural features (defects, dislocations, grain boundaries, precipitates, etc.).

The strength of interatomic forces and the crystal structure determine the elastic properties of a material, and, to a big extent, its intrinsic hardness [42]. It is also required for intrinsic hardness, that a material can resist to disclocation generation and propagation [42]. The latter is easiest achieved in materials with highly directional bonds, i.e., in covalent hard materials. So, diamond, a purely covalent material, is one of the hardest materials known. Most of materials, though, have a mixed type of bonding. It is established, that, in general, the hardness decreases as the fraction of covalent bonding in total material bonding decreases. It can be illustrated with the three compounds TiC, TiN, and TiO [42]. All of them have the same crystal structure (NaCl type), their lattice parameters are similar. Yet, the approximate hardness of TiC is 3000 kg·mm^{-2}, for TiN it is 2000 kg·mm^{-2}, and the hardness of TiO is around 1000 kg·mm^{-2}. Which is consistent with the decrease of the covalent contribution in bonding, and the increase of ionic one in the sequence from TiC to TiN to TiO. Thus, getting the understanding of the bonding between atoms in materials is of vital importance.

Most of the real hard materials used for coatings (thin films on tools) are rarely sigle-crystals. Usually, they have a complicated microstructure with a lot of grain boundaries, defects, etc. Microstructure of a material can change its hardness drastically. In thin metal alloy films, for instance, the decrease of the grain size in a certain range leads to their hardening, which is described by Hall-Petch relation

$$H(d) = H_0 + k \cdot d^{-\frac{1}{2}}, \tag{2.1}$$

where H_0 is the intrinsic hardness, k is a constant, which depends on material, and d is grain size.

Chapter 3

Theoretical background

3.1 Elasticity in solids

3.1.1 Introduction

In the present section, a short overview of the most common classes of mathematical objects used to describe the physics of diverse natural phenomena, including elasticity of solids, is provided. These classes of objects are scalars, vectors, and tensors. The latter class is the most general one out of the three, and includes the former two as sub-classes, thus each of them is seen as an instance of a certain type of tensors. Among the variety of approches to introduce tensors, we choose the one based on the description of the transformation laws of the tensor coordinates upon the change of the basis. The simplest tensors are illustrated by physical examples. The section is mainly based on the excellent classical textbook on tensors by J.F. Nye [45], the great collection of mathematical facts by G.B. Arfken and H.J. Weber [46], and a concise and very clearly written introduction to tensorial analysis by R.A. Sharipov [47]. The section is organized in the following way: We start with basic remarks on scalars, vectors, and tensors in order to facilitate the discussion of the rest of the section, which is devoted to special kinds of tensors, namely, the stress tensor, the strain tensor, and the elasticity tensor.

3.1.2 Scalars, vectors, and tensors

Scalars

Physical quantities which can be completely specified by giving a single number are called *scalars*. The temperature of a body, its macroscopic density or mass all have no directional dependence, and are examples of scalar quantities. For scalars have no directional dependence, they are invariant under the change of the coordinate system (basis), i.e.

$$s' = s, \tag{3.1}$$

where s and s' are the values of a scalar in coordinate systems $OX_1X_2X_3$ and $OX'_1X'_2X'_3$, respectively. Scalars are said to be rank-0 tensors for a reason to be explained later on.

Vectors

As opposed to scalars there are physical quantities which can only be specified by reference to directions. These physical quantities are called *vectors*. Velocity, acceleration, or mechanical force are examples of vectors. In order to specify a force acting at a point, one needs to provide both the magnitude of the force and its direction. If we choose three mutually perpendicular axes with unit lenght $\mathbf{e_1}$, $\mathbf{e_2}$, $\mathbf{e_3}$ (they form a cartesian basis in $\mathbf{R}^3$), we can uniquely represent a vector $\mathbf{v}$ as

$$\mathbf{v} = v^1\mathbf{e}_1 + v^2\mathbf{e}_2 + v^3\mathbf{e}_3 = \sum_{i=1}^{3} v^i\mathbf{e}_i = v^i\mathbf{e}_i, \tag{3.2}$$

where v^1, v^2, and v^3 are the projections of $\mathbf{v}$ on $\mathbf{e}_1$, $\mathbf{e}_2$, and $\mathbf{e}_2$, respectively. In the very latest equality the Einstein's summation rule is used.

Suppose we change the basis, so that the new basis ($\mathbf{e}'_1$, $\mathbf{e}'_2$, and $\mathbf{e}'_3$) is connected to the old one ($\mathbf{e}_1$, $\mathbf{e}_2$, and $\mathbf{e}_3$) by the relations

$$\mathbf{e}'_i = S_i^j\mathbf{e_j}, \tag{3.3}$$

$$\mathbf{e}_i = T_i^j\mathbf{e}'_j, \tag{3.4}$$

where S_i^j is a projection of $\mathbf{e}'_i$ on $\mathbf{e}_j$, whereas T_i^j is a projection of $\mathbf{e}_i$ on $\mathbf{e}'_j$. The numbers S_i^j form *the direct transition matrix* $\mathbf{S}$:

$$\mathbf{S} = \begin{bmatrix} S_1^1 & S_2^1 & S_3^1 \\ S_1^2 & S_2^2 & S_3^2 \\ S_1^3 & S_2^3 & S_3^3 \end{bmatrix}. \tag{3.5}$$

The inverse transition matrix is made of T_i^j as follows

$$\mathbf{T} = \begin{bmatrix} T_1^1 & T_2^1 & T_3^1 \\ T_1^2 & T_2^2 & T_3^2 \\ T_1^3 & T_2^3 & T_3^3 \end{bmatrix}. \tag{3.6}$$

These two transition matrices are related to each other by the formula

$$\mathbf{S} \cdot \mathbf{T} = \mathbf{I}, \tag{3.7}$$

where **I** is the identity matrix. The components of a vector **v** in the new basis can be found from the relation

$$\mathbf{v} = v^i \mathbf{e}_i = v^i T_i^j {\mathbf{e}'}_j = \left(T_i^j v^i\right) {\mathbf{e}'}_j = v'^j {\mathbf{e}'}_j, \tag{3.8}$$

therefore

$$v'^j = T_i^j v^i \quad \text{or} \quad v'^i = T_j^i v^j. \tag{3.9}$$

A mathematical object dual to vector is called a *co-vector*. Its transformation law is very similar to the one of vector, and is given by the expression

$$\mathbf{v} = v_i \mathbf{e}^i = v_i S_j^i \mathbf{e}'^j = \left(S_j^i v_i\right) \mathbf{e}'^j = v'_j \mathbf{e}'^j, \tag{3.10}$$

therefore

$$v'_j = S_j^i v^i \quad \text{or} \quad v'_i = S_i^j v_j. \tag{3.11}$$

Vectors along with co-vectors are the instances of rank-1 tensors.

Tensors

When dealing with diverse properties of solids, it might happen that scalars and vectors are not sufficient. The classical illustration of this phenomenon is conductivity. Consider a conductor exposed to the electric field given by the vector **E**. The current density **j**, i.e., current per unit cross-section normal to the current, depends on the degree of isotropy of the conductor. In case of an isotropic conductor which obeys Ohm's law, **j** is parallel and proportional to **E** (Fig. 3.1a)

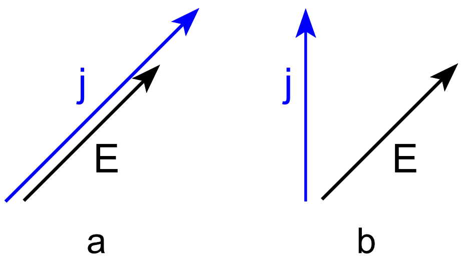

Figure 3.1: The relation between the electric current density **j** and the electric field **E** in (a) an isotropic conductor and (b) an anisotropic conductor.

$$\mathbf{j} = \sigma \mathbf{E} \quad \textit{or} \quad j_1 = \sigma E_1, \quad j_2 = \sigma E_2, \quad j_3 = \sigma E_3, \tag{3.12}$$

where σ is the conductivity. If the conductor is anisotropic, then the connection between the electric field and the current density is more complicated. For a general anisotropic solid every component of $\mathbf{j}$ is linearly related to all components of $\mathbf{E}$ (Fig. 3.1b):

$$\begin{aligned} j_1 &= \sigma_{11}E_1 + \sigma_{12}E_2 + \sigma_{13}E_3 \\ j_2 &= \sigma_{21}E_1 + \sigma_{22}E_2 + \sigma_{23}E_3 \\ j_3 &= \sigma_{31}E_1 + \sigma_{32}E_2 + \sigma_{33}E_3 \end{aligned} \tag{3.13}$$

where σ_{11}, σ_{12}, ..., σ_{33} are constants. The σ_{ij}'s have the physical meaning of a proportionality coefficient between the current density induced along the i-th axis, while the electric field is applied along the j-th axis. Thus, in order to specify the conductivity of a crystal, one has to specify 9 numbers σ_{ij} $(i, j = 1..3)$. These numbers can be compiled in a square 3-by-3 matrix:

$$\begin{bmatrix} \sigma_{11} & \sigma_{12} & \sigma_{13} \\ \sigma_{21} & \sigma_{22} & \sigma_{23} \\ \sigma_{31} & \sigma_{32} & \sigma_{33} \end{bmatrix}.$$

This matrix is the coordinate representation of the conductivity tensor, where σ_{ij}'s are the components of the tensor. The conductivity tensor is an example of a rank-2 tensor. Table 3.1 contains more examples of second-rank tensor properties. In general, if a property T relates two vectors $\mathbf{p}$ and $\mathbf{q}$ in such a way that

Table 3.1: Some examples of second-rank tensors relating two vectors [45].

Tensor property	Vector given or applied	Vector resulting or induced
Electrical conductivity	electric field	electric current density
Thermal conductivity	temperature gradient	heat flow density
Permittivity	electric field	dielectric displacement
Dielectric susceptibility	electric field	dielectric polarization
Permeability	magnetic field	magnetic induction
Magnetic susceptibility	magnetic field	intensity of magnetization

$$\begin{array}{rcccccc} p_1 & = & T_{11}q_1 & + & T_{12}q_2 & + & T_{13}q_3 \\ p_2 & = & T_{21}q_1 & + & T_{22}q_2 & + & T_{23}q_3 \\ p_3 & = & T_{31}q_1 & + & T_{32}q_2 & + & T_{33}q_3 \end{array}$$

where T_{ij}'s are constants, T is said to be a rank-2 tensor with the components:

$$\begin{bmatrix} T_{11} & T_{12} & T_{13} \\ T_{21} & T_{22} & T_{23} \\ T_{31} & T_{32} & T_{33} \end{bmatrix}.$$

It is useful now to compare the properties of the considered quantities (in three-dimensional space) with the emphasis on transformation laws of their coordinate

Table 3.2: Transformation laws for tensors [45]

Name	Rank of tensor	Transformation law	
		New in terms of old	Old in terms of new
Scalar	0	$\phi' = \phi$	$\phi = \phi'$
Vector	1	$p'_i = a_{ij} p_j$	$p_i = a_{ji} p'_j$
-	2	$T'_{ij} = a_{ik} a_{jl} T_{kl}$	$T_{ij} = a_{ki} a_{lj} T'_{kl}$
-	3	$T'_{ijk} = a_{il} a_{jm} a_{kn} T_{lmn}$	$T_{ijk} = a_{li} a_{mj} a_{nk} T'_{lmn}$
-	4	$T'_{ijkl} = a_{im} a_{jn} a_{ko} a_{lp} T_{mnop}$	$T_{ijkl} = a_{mi} a_{nj} a_{ok} a_{pl} T'_{mnop}$

representations given in Table 3.2: 1) a rank-0 tensor, also known as a scalar, is specified by a single number unrelated to any axes of reference;
2) a rank-1 tensor (a vector or a co-vector) is specified by 3 components, each of which is associated with one of the axes of reference;
3) a rank-2 tensor is specified by 9 components, each of which is associated with a pair of axes (taken in a particular order).

Generally, a rank-N tensor is specified by 3^N components, each of which is associated with N axes, taken in a particular order.

It is important to distinguish between the tensor itself and its coordinate representation in a particular coordinate system. When a coordinate system is rotated, the coordinates of a tensor, generally, change, while the tensor remains unchanged.

3.1.3 Stress tensor

In order to introduce the notion of stress, we give here a definition of Nye [45]: "A body which is acted on by external forces, or, more generally, a body in which one part exerts a force on neighbouring parts, is said to be in a state of stress. If we consider a volume element situated within a stressed body, we may recognize two kinds of forces acting upon it. First of all, there are body forces, such as gravity, which act troughout the body on all its elements and whose magnitudes are proportional to the *volume* of the element. Secondly, there are forces exerted on the surface of the element by material surrounding it. These forces are proportional to the *area* of the surface of the element, and the force per unit area is called 'stress'."

Stress can be homogeneous or inhomogeneous. The homogeneous stress is the one for which the forces acting on the surface of an element of fixed shape and orientation are independent of the position of the element in the body, otherwise the stress is inhomogeneous.

We consider only homogeneously stressed bodies, when all parts of the body are in statical equilibrium, with no body-forces or body-torques present. In the further discription a unit cube within the body (Fig. 3.2) is considered, whose edges are parallel to the cartesian axes. A stress acts upon each face of the cube, exerted by the material outside the cube. The stress across each face can be expressed by three components. The stress notation is the following: σ_{ij} denotes the component of stress in the $+Ox_i$ direction transmitted across the cube face which is perpendicular to Ox_j. $\sigma_{11}, \sigma_{22}, \sigma_{33}$ are the normal components of stress, while $\sigma_{12}, \sigma_{21}, \sigma_{23}$ etc. are the shear components. The stress is a tensorial property, and is described by a rank-2 tensor. σ_{ij}'s are the components of the stress-tensor in the fixed cartesian basis $Ox_1x_2x_3$. A positive value of σ_{11}, σ_{22} or σ_{33} corresponds to tensile stress, while a negative value is an indication of compressive stress. Additional information on the stress-tensor, including strict derivations and proofs can be found somewhere else [45].

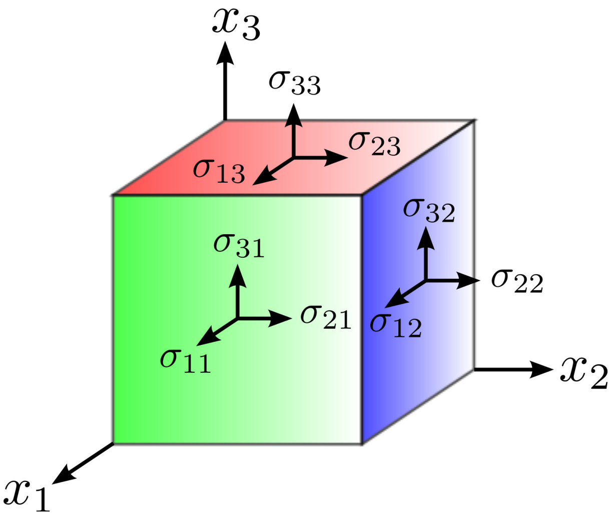

Figure 3.2: The forces on the faces of a unit cube in a homogeneously stressed body.

3.1.4 Strain tensor

The problem of specifying the state of deformation of a solid body, which we take up in this chapter, may be approached by considering first the simpler one-dimensional and two-dimensional cases.

1D-strain

Fig. 3.3a shows an elastic string, it is fixed at the origin 0. After stretching

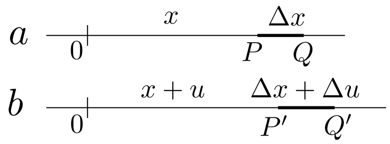

Figure 3.3: The deformation of an extendible string: (a) unstretched, (b) stretched.

(Fig. 3.3b), two arbitrary points P and Q on the string move to P' and Q', respectively. Let

$$\begin{aligned} P = x \quad &\text{and} \quad P' = x + u, \\ Q = x + \Delta x \quad &\text{and} \quad Q' = x + u + \Delta x + \Delta u, \\ PQ = \Delta x \quad &\text{and} \quad P'Q' = \Delta x + \Delta u. \end{aligned}$$

When considering strain, we are interested in the relative changes only, thus the strain of the section PQ is defined as:

$$\frac{P'Q' - PQ}{PQ} = \frac{\Delta u}{\Delta x}.$$

Making a limiting transition we come up with the strict definition of the strain:

$$e = \lim_{\Delta x \to 0} \frac{\Delta u}{\Delta x} = \frac{du}{dx}.$$

The variation of the displacement u with x is shown in Figs. 3.4 a and b. If u is a linear functiuon of x (Fig. 3.4a), then the string is stretched homogeneously. A more general case of inhomogeneous stretching is shown in Fig. 3.4b.

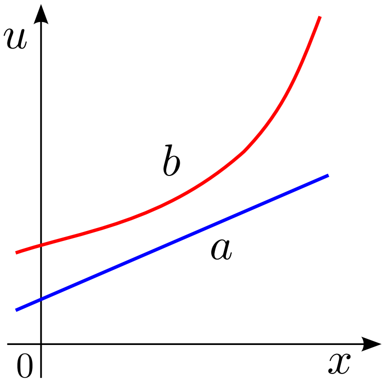

Figure 3.4: The displacement u as a function of x in an extended string; (a) homogeneous stretching, (b) inhomogeneous stretching.

2D-strain

Let us now consider how to specify the deformation of an elastic plane sheet. As for the 1D-case, we choose a Cartesian basis, and study how the displacement of the points of the sheet changes with their coordinates. Hereafter only small displacements are considered. Assume the section $\boldsymbol{PQ}$ (Fig. 3.5), where

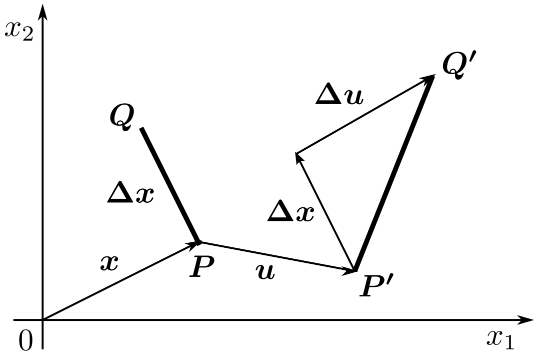

Figure 3.5: Two-dimensional strain.

$\boldsymbol{P} = (x_1, x_2)$ and $\boldsymbol{Q} = \boldsymbol{P} + \boldsymbol{\Delta x} = (x_1 + \Delta x_1, x_2 + \Delta x_2)$, maps to $\boldsymbol{P'Q'}$ upon deformation, with $\boldsymbol{P'} = \boldsymbol{P} + \boldsymbol{u}$ and $\boldsymbol{Q'} = \boldsymbol{Q} + \boldsymbol{u} + \boldsymbol{\Delta u}$. It is evident that $\boldsymbol{PQ} = \boldsymbol{\Delta x}$, $\boldsymbol{P'Q'} = \boldsymbol{\Delta x} + \boldsymbol{\Delta u}$, thus the relative deformation is $\boldsymbol{P'Q'} - \boldsymbol{PQ} = \boldsymbol{\Delta u}$. As $\boldsymbol{u} = \boldsymbol{u}(x_1, x_2)$, i.e., it is a function of x_1 and x_2, one can write its differential $\boldsymbol{\Delta u} = (\Delta u_1, \Delta u_2)$:

$$\Delta u_1 = e_{11}\Delta x_1 + e_{12}\Delta x_2, \tag{3.14}$$

$$\Delta u_2 = e_{21}\Delta x_1 + e_{22}\Delta x_2, \tag{3.15}$$

where $e_{ij} = \frac{\partial u_i}{\partial x_j} \quad (i, j = 1, 2)$. Written in a compact way it turns:

$$\Delta u_i = \frac{\partial u_i}{\partial x_j}\Delta x_j = e_{ij}\Delta x_j.$$

As far as the set of e_{ij} connects two vectors, the Δu_i and the Δx_j, it is a coordinate representation of a rank-2 tensor. Any second-rank tensor can be decomposed into the sum of a symmetrical and an antisymmetrical tensor. In case of $[e_{ij}]$ we write:

$$e_{ij} = \epsilon_{ij} + \varpi_{ij},$$

where $\epsilon_{ij} = \frac{1}{2}(e_{ij} + e_{ji})$, and $\varpi_{ij} = \frac{1}{2}(e_{ij} - e_{ji})$. This division of $[e_{ij}]$ into two parts is illustrated in Fig. 3.6. It is clear, that $[\epsilon_{ij}]$ describes the very strain, and is a symmetrical tensor, for

$$\epsilon_{ij} = \frac{1}{2}(e_{ji} + e_{ij}) = \epsilon_{ji}.$$

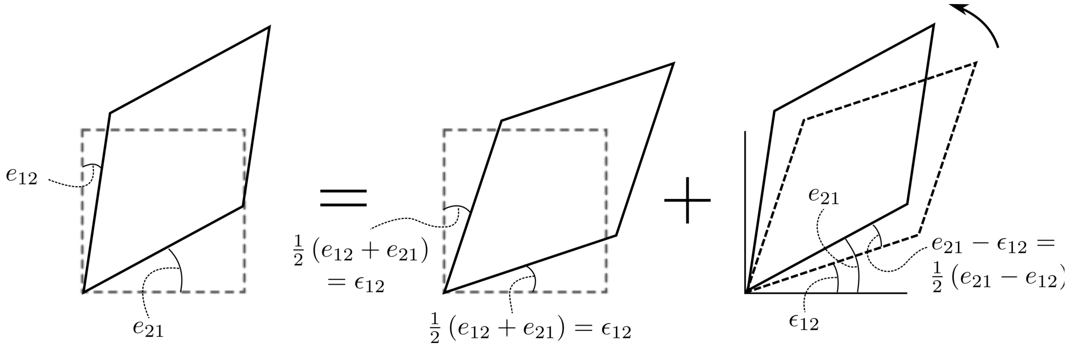
e_{12}
e_{21}
$=$
$\frac{1}{2}(e_{12}+e_{21})$
$= \epsilon_{12}$
$\frac{1}{2}(e_{12}+e_{21}) = \epsilon_{12}$
$+$
e_{21}
$e_{21} - \epsilon_{12} =$
$\frac{1}{2}(e_{21} - e_{12})$
ϵ_{12}

Figure 3.6: A two-dimensional illustration of the proposition: a general deformation (left-hand diagram) equals a strain (central diagram) plus a rotation (right-hand diagram).

Instead $[\varpi_{ij}]$ describes a rigid rotation, and is an antisymmetrical tensor, for

$$\varpi_{ij} = -\frac{1}{2}\left(e_{ji} - e_{ij}\right) = -\varpi_{ji}.$$

Finally, we can compile the components of the strain tensor in the matrix form:

$$\begin{bmatrix} \epsilon_{11} & \epsilon_{12} \\ \epsilon_{21} & \epsilon_{22} \end{bmatrix} = \begin{bmatrix} e_{11} & \frac{1}{2}(e_{12}+e_{21}) \\ \frac{1}{2}(e_{12}+e_{21}) & e_{22} \end{bmatrix}.$$

The diagonal components of $[\epsilon_{ij}]$ are the extensions per unit length parallel to Ox_1 and Ox_2, whereas ϵ_{12} measures the shear strain.

3D-strain

Specifying the strain in the three-dimensional case is just a straightforward extension of the two former cases. Again, the variation of the displacement u_i as a function of x_i is used to define nine tensor components:

$$e_{ij} = \frac{\partial u_i}{\partial x_j} \quad (i, j = 1, 2, 3).$$

The strain tensor $[\epsilon_{ij}]$ is defined as the symmetrical part of $[e_{ij}]$:

$$\epsilon_{ij} = \frac{1}{2}\left(e_{ij} + e_{ji}\right).$$

The components of strain tensor ϵ_{ij} can be put in a matrix:

$$\begin{bmatrix} \epsilon_{11} & \epsilon_{12} & \epsilon_{31} \\ \epsilon_{12} & \epsilon_{22} & \epsilon_{23} \\ \epsilon_{31} & \epsilon_{23} & \epsilon_{33} \end{bmatrix} = \begin{bmatrix} e_{11} & \frac{1}{2}(e_{12}+e_{21}) & \frac{1}{2}(e_{13}+e_{31}) \\ \frac{1}{2}(e_{12}+e_{21}) & e_{22} & \frac{1}{2}(e_{23}+e_{32}) \\ \frac{1}{2}(e_{13}+e_{31}) & \frac{1}{2}(e_{23}+e_{32}) & e_{33} \end{bmatrix}.$$

As for the two-dimensional case, the diagonal components of ϵ_{ij} are the stretches or tensile strains along the corresponding axes. While the other components indicate the shear strains.

3.1.5 Elasticity tensor

Hooke's law

If a solid body is exposed to a stress its volume and shape change. When the stress is below a certain limit, which is individual for each material, the body recovers its initial state after the stress is removed. This is called elastic deformation. It might happen that the applied stress is above the elastic limit, and the body deforms irreversibly, or plastically. It was established that in the case of a small enough stress, the strain ϵ can be calculated as a linear function of the stress σ. Hooke's law for an isotropic solid is:

$$\epsilon = s\sigma,$$

where s is a constant, which is called the elastic compliance constant or the compliance. The inverse of the formula is:

$$\sigma = c\epsilon, \qquad c = 1/s,$$

where c is the elastic stiffness constant, or the stiffness (also known as Young's Modulus). In the general case of an anisotropic solid, homogeneous stress and strain are described as rank-2 tensors. Therefore, the generalized form of Hooke's law may be written as:

$$\epsilon_{ij} = s_{ijkl}\sigma_{kl}, \quad (i,j,k,l = 1,2,3)\,,$$

where s_{ijkl} are the compliances of the crystal. When written in the inverse form one gets:

$$\sigma_{ij} = c_{ijkl}\epsilon_{kl},$$

where the c_{ijkl} are the stiffness constants of the crystal.

If two rank-2 tensors A_{ij} and B_{kl} are related by the equation

$$A_{ij} = C_{ijkl}B_{kl},$$

the quantities C_{ijkl} form a rank-4 tensor. It follows, therefore, that the elastic compliance s_{ijkl} and stiffness constants c_{ijkl} form rank-4 tensors. There are in total $3^4 = 81$ components of a general elastic compliance or stiffnes tensor, yet not all of them are independent. As stress tensor σ_{ij} and strain tensor ϵ_{kl} are symmetric, each of them has just 6 independent components instead of 9. It follows then that, for example, the elastic stiffness tensor gives the connection between 6 independent components of stress and 6 independent components of strain, leading to the conclusion that there are only $6 \times 6 = 36$ independent components of the elastic stiffness tensor instead of 81. The same is valid for the components of elastic compliance tensor. When thermodynamics (see 3.1.5) and the symmetry (see Appendix A) of a crystal are taken into consideration, the number of independent components might be reduced even further.

The matrix notation

The symmetry of s_{ijkl} and c_{ijkl} in the first two and the last two suffixes makes it possible to use the so-called matrix notation. The stress components and the strain components are written in this notation with a single suffix running from 1 to 6:

$$\begin{bmatrix} \sigma_{11} & \sigma_{12} & \sigma_{31} \\ \sigma_{12} & \sigma_{22} & \sigma_{23} \\ \sigma_{31} & \sigma_{23} & \sigma_{33} \end{bmatrix} \rightarrow \begin{bmatrix} \sigma_1 & \sigma_6 & \sigma_5 \\ \sigma_6 & \sigma_2 & \sigma_4 \\ \sigma_5 & \sigma_4 & \sigma_3 \end{bmatrix},$$

$$\begin{bmatrix} \epsilon_{11} & \epsilon_{12} & \epsilon_{31} \\ \epsilon_{12} & \epsilon_{22} & \epsilon_{23} \\ \epsilon_{31} & \epsilon_{23} & \epsilon_{33} \end{bmatrix} \rightarrow \begin{bmatrix} \epsilon_1 & \frac{1}{2}\epsilon_6 & \frac{1}{2}\epsilon_5 \\ \frac{1}{2}\epsilon_6 & \epsilon_2 & \frac{1}{2}\epsilon_4 \\ \frac{1}{2}\epsilon_5 & \frac{1}{2}\epsilon_4 & \epsilon_3 \end{bmatrix}.$$

The factor $\frac{1}{2}$ is introduced to make the further equations compact. In the elastic compliance s_{ijkl} and the elastic stiffness c_{ijkl} the first and the last pair of indices are abbreviated into a single one running from 1 to 6 according to Table 3.3. At the same time, for the sake of compactness of equations in matrix notation, factors of 2 and 4 are introduced for compliances as follows:

Table 3.3: Relationships between tensor and matrix indices.

tensor notation	11	22	33	23, 32	31, 13	12, 21
matrix notation	1	2	3	4	5	6

$$s_{ijkl} = s_{mn} \text{ when m and n are 1, 2 or 3,}$$
$$2s_{ijkl} = s_{mn} \text{ when either m or n are 4, 5 or 6,}$$
$$4s_{ijkl} = s_{mn} \text{ when both m and n are 4, 5 or 6.}$$

Using the matrix notation, the tensor equation

$$\epsilon_{ij} = s_{ijkl}\sigma_{kj} \quad (i, j, k, l = 1, 2, 3)$$

turns into

$$\epsilon_i = s_{ij}\sigma_j \quad (i, j = 1, 2, ..., 6)\,.$$

For the c_{ijkl} there is no need to introduce factors of 2 or 4. It is enough to introduce them in one of the s_{ij} or c_{ij}, the standard convention is to put factors into s_{ij}. Thus:

$$c_{ijkl} = c_{mn} \quad (i,j,k,l = 1,2,3; m,n = 1,...,6)$$

The generalized Hooke's law is written then as:

$$\sigma_i = c_{ij}\epsilon_j \quad (i,j = 1,2,...,6)\,.$$

The arrays of s_{ij} and c_{ij} written out as 6 × 6 matrices are:

$$\begin{pmatrix} s_{11} & s_{12} & s_{13} & s_{14} & s_{15} & s_{16} \\ s_{21} & s_{22} & s_{23} & s_{24} & s_{25} & s_{26} \\ s_{31} & s_{32} & s_{33} & s_{34} & s_{35} & s_{36} \\ s_{41} & s_{42} & s_{43} & s_{44} & s_{45} & s_{46} \\ s_{51} & s_{52} & s_{53} & s_{54} & s_{55} & s_{56} \\ s_{61} & s_{62} & s_{63} & s_{64} & s_{65} & s_{66} \end{pmatrix} \quad \text{and} \quad \begin{pmatrix} c_{11} & c_{12} & c_{13} & c_{14} & c_{15} & c_{16} \\ c_{21} & c_{22} & c_{23} & c_{24} & c_{25} & c_{26} \\ c_{31} & c_{32} & c_{33} & c_{34} & c_{35} & c_{36} \\ c_{41} & c_{42} & c_{43} & c_{44} & c_{45} & c_{46} \\ c_{51} & c_{52} & c_{53} & c_{54} & c_{55} & c_{56} \\ c_{61} & c_{62} & c_{63} & c_{64} & c_{65} & c_{66} \end{pmatrix}$$

It is important to emphasize, that, though both c_{ij} and s_{ij} have two suffixes, they are not the components of a rank-2 tensor, thus the transormation law of rank-2 tensors is not applicable to c_{ij} or s_{ij}.

The energy of a strained crystal

Imagine a unit cubic crystal subjected to a moderate homogeneous strain ϵ_i. If the strain components are sligntly changed to $\epsilon_i + d\epsilon_i$, then it can be shown [45] that the work done by the stress components σ_i, acting on the cube faces reads

$$dW = \sigma_i d\epsilon_i \quad (i = 1,2,...,6)\,.$$

If the deformation process is isothermal and reversible the work done is equal to the increase in the free energy $d\Psi$, per unit volume,

$$d\Psi = dW = \sigma_i d\epsilon_i.$$

Provided Hooke's law is obeyed the increase of the free energy turns into

$$d\Psi = c_{ij}\epsilon_j d\epsilon_i.$$

Thus,

$$\frac{\partial \Psi}{\partial \epsilon_i} = c_{ij}\epsilon_j.$$

After differentiating both sides of this equation with respect to ϵ_j we get

$$\frac{\partial}{\partial \epsilon_j}\left(\frac{\partial \Psi}{\partial \epsilon_i}\right) = c_{ij}.$$

As Ψ is a function of the state of the body [45], which depends on the strain components, the order of differentiation makes no difference, i.e.

$$\frac{\partial^2\Psi}{\partial\epsilon_i\partial\epsilon_j} = \frac{\partial^2\Psi}{\partial\epsilon_j\partial\epsilon_i}.$$

Hence,

$$c_{ij} = c_{ji},$$

and

$$s_{ij} = s_{ji}.$$

The symmetry of the (c_{ij}) and (s_{ij}) matrices further reduces the number of independent elastic constants from 36 to 21.

Integrating equation (18) and using (19) we find that the work necessary to produce a strain ϵ_i, called the strain energy, is

$$\frac{1}{2}c_{ij}\epsilon_i\epsilon_j$$

per unit volume of the crystal.

3.2 Density functional theory

A rigorous quantum mechanical treatment of atoms, molecules, or solids requires solving the many-body Schrödinger equation. In its time-independent formulation it takes the form

$$\hat{H}_{n,e}|\Phi\rangle = E_{n,e}|\Phi\rangle, \tag{3.16}$$

where

$$\hat{H}_{n,e} = \hat{T}_n + \hat{T}_e + \hat{U}_{n-n} + \hat{U}_{n-e} + \hat{U}_{e-e}. \tag{3.17}$$

Here, $\hat{H}_{n,e}$ is a many-body Hamiltonian that embodies the kinetic energy and all interactions in the system composed of the nuclei and the electrons. $E_{n,e}$ is the spectrum of the Hamiltonian, $|\Phi\rangle$ represents the eigenstates of the Hamiltonian, $\hat{T}_n$ is the kinetic energy operator of the nuclei, $\hat{T}_e$ is the kinetic energy operator of the electrons, $\hat{U}_{n-n}$ is the potential energy operator of the nucleus-nucleus interaction, $\hat{U}_{n-e}$ is the potential energy operator of the nucleus-electron interaction, and $\hat{U}_{e-e}$ is the potential energy operator of the electron-electron interaction. Due to a significant difference in the masses of nuclei and electrons – nuclei are 10^3–10^4 times heavier than electrons – electrons adjust to a change of the position of nuclei almost instantaneously, and thus, it is a common practice to separate the electronic and the nuclear degrees of freedom. That is, the problem of interacting nuclei and electrons reduces to that of interacting electrons in a constant Coulomb potential V of steady nuclei. This simplification is known as Born-Oppenheimer approximation. Ommiting nuclear kinetic energy and nucleus-nucleus interaction operators, equations 3.16 and 3.17 turn into

$$\hat{H}|\Psi\rangle = E|\Psi\rangle, \tag{3.18}$$

where

$$\hat{H} = \hat{T} + \hat{V} + \hat{U}, \tag{3.19}$$

and

$$\hat{T} = \hat{T}_e, \tag{3.20}$$

$$\hat{V} = \hat{U}_{n-e}, \tag{3.21}$$

$$\hat{U} = \hat{U}_{e-e}. \tag{3.22}$$

Here, $|\Psi\rangle$ symbolizes the eigenstates of $\hat{H}$. $|\Psi\rangle$ can be represented in the position basis as $\Psi(\boldsymbol{r}_1, \boldsymbol{r}_2, ..)$ – a many-body wavefunction of interacting electrons in an external potential of nuclei. It is possible to solve Eq. 3.18 for systems composed of few electrons, i.e., to find the many-body wavefunction. Despite a certain success of this approach in describing small molecules, its computational demands rapidly become prohibitive as the number of the considered electrons increases. This problem is known as Van Vleck catastrophe or the exponential wall problem [48].

To cope with systems of many electrons, an elegant idea was proposed by Hohenberg and Kohn [49] in 1964, that can be described by the two following theorems:

1. The full many-particle ground state is a unique functional of the ground state electronic density [49], i.e.,

   $$\Psi_0(\boldsymbol{r}_1, \boldsymbol{r}_2, .., \boldsymbol{r}_N) = \Psi_0[n_0(\boldsymbol{r})], \tag{3.23}$$

   where Ψ_0 is the ground state wavefunction of N interacting electrons in the external potential $V(\boldsymbol{r})$, $\boldsymbol{r}_i$ are the positions of electrons, and $n_0(\boldsymbol{r})$ is the ground state electronic density – a function of three spatial coordinates given by a vector $\boldsymbol{r}$.

2. The ground state electronic density $n_0(\boldsymbol{r})$ minimizes the energy functional $E[n(\boldsymbol{r})]$, i.e.,

   $$E[n_0(\boldsymbol{r})] \leq E[n(\boldsymbol{r})], \tag{3.24}$$

   where

   $$E[n(\boldsymbol{r})] = \langle\Psi[n(\boldsymbol{r})]|\hat{H}|\Psi[n(\boldsymbol{r})]\rangle = \tag{3.25}$$

   $$= \langle\Psi[n(\boldsymbol{r})]|\hat{T} + \hat{U} + \hat{V}|\Psi[n(\boldsymbol{r})]\rangle = \tag{3.26}$$

   $$= \langle\Psi[n(\boldsymbol{r})]|\hat{T} + \hat{U}|\Psi[n(\boldsymbol{r})]\rangle + \langle\Psi[n(\boldsymbol{r})]|\hat{V}|\Psi[n(\boldsymbol{r})]\rangle = \tag{3.27}$$

   $$= F[n(\boldsymbol{r})] + \int V(\boldsymbol{r})n(\boldsymbol{r})d\boldsymbol{r}. \tag{3.28}$$

> Here, $F[n(\boldsymbol{r})]$ is a universal functional of the electronic density $n(\boldsymbol{r})$, which desribes the kinetic and potential energies of interacting electrons.

The exact form of $F[n(\boldsymbol{r})]$ is not known; however, Kohn and Sham [50] wrote it as

$$F[n(\boldsymbol{r})] = T_s[n(\boldsymbol{r})] + \frac{1}{2}\int \frac{n(\boldsymbol{r})n(\boldsymbol{r}')}{|\boldsymbol{r}-\boldsymbol{r}'|} d\boldsymbol{r}d\boldsymbol{r}' + E_{xc}[n(\boldsymbol{r})], \tag{3.29}$$

where $T_s[n(\boldsymbol{r})]$ is the kinetic energy functional for *non-interacting* electrons, the second term is the Hartree energy, and $E_{xc}[n(\boldsymbol{r})]$ is referred to as the *exchange-correlation* energy functional. Taking into account 3.29, Kohn and Sham concluded that the ground state density can be obtained by solving the *single-particle* equation [48]

$$\left(-\frac{1}{2}\nabla^2 + v_{eff}(\boldsymbol{r})\right)\phi_j(\boldsymbol{r}) = \epsilon_j \phi_j(\boldsymbol{r}), \tag{3.30}$$

where the effective potential $v_{eff}(\boldsymbol{r})$ is defined as

$$v_{eff}(\boldsymbol{r}) = V(\boldsymbol{r}) + \int \frac{n(\boldsymbol{r}')}{|\boldsymbol{r}-\boldsymbol{r}'|} d\boldsymbol{r}' + v_{xc}(\boldsymbol{r}), \tag{3.31}$$

and the total electronic density is given by

$$n(\boldsymbol{r}) = \sum_{j=1}^{N} |\phi_j(\boldsymbol{r})|^2. \tag{3.32}$$

The last term in Eq. 3.31, i.e., $v_{xc}(\boldsymbol{r})$ is called the exchange-correlation potential and is defined as functional derivative of the exchange-correlation energy functional

$$v_{xc}(\boldsymbol{r}) = \frac{\delta}{\delta \tilde{n}(\boldsymbol{r})} E_{xc}[\tilde{n}(\boldsymbol{r})]|_{\tilde{n}(\boldsymbol{r})=n(\boldsymbol{r})}. \tag{3.33}$$

Equations 3.30–3.32 are known as Kohn-Sham (KS) equations. After solving them self-consistently, the ground state energy is given by

$$E = \sum_{j=1}^{N} \epsilon_j + E_{xc}[n(\boldsymbol{r})] - \int v_{xc}(\boldsymbol{r})n(\boldsymbol{r})d\boldsymbol{r} - \frac{1}{2}\int \frac{n(\boldsymbol{r})n(\boldsymbol{r}')}{|\boldsymbol{r}-\boldsymbol{r}'|} d\boldsymbol{r}d\boldsymbol{r}'. \tag{3.34}$$

Unfortunately, the exact expressions for $E_{xc}[n(\boldsymbol{r})]$, and thus for $v_{xc}(\boldsymbol{r})$, are not known. Therefore, the crucial point for practical applications of the KS equations is to find a good approximation to the exchange-correlation functional.

3.2.1 Approximations for $\mathbf{E}_{xc}$

Historically, the first and simplest approximation for the exchange-correlation functional is the local-density approximation (LDA), that assumes E_{xc} to be locally equal to that of the homogeneous electron gas of density $n(\boldsymbol{r})$:

$$E_{xc}^{\mathrm{LDA}}[n(\boldsymbol{r})] = \int \epsilon_{xc}^{\mathrm{hom}}(n(\boldsymbol{r}))n(\boldsymbol{r})d\boldsymbol{r}. \tag{3.35}$$

Here $\epsilon_{xc}^{\mathrm{hom}}(n(\boldsymbol{r}))$ is the exchange-correlation energy per electron of the homogeneous electron gas [50–52]. Despite the clearly unrealistic assumption of the homogeneity, LDA gives a reasonable agreement with experimental values of stuctural parameters of molecules and solids, typically, underestimating them by a few percent. Binding energies, however, are overestimated by as much as 10-20%.

The next step in search for an approximation to $E_{xc}[n(\boldsymbol{r})]$ that would perform better than LDA, was to incorporate the explicit dependence on the density gradient in the exchange-correlation functional

$$E_{xc}^{\mathrm{GGA}}[n(\boldsymbol{r})] = \int f(n(\boldsymbol{r}), |\nabla n(\boldsymbol{r})|)n(\boldsymbol{r})d\boldsymbol{r}, \tag{3.36}$$

giving rise to a family of generalized gradient approximations (GGAs) [53]. Most popular formulations of GGA are the Perdew-Wang functional (PW91) [54], the Perdew-Burke-Ernzerhof functional (PBE) [55] and its improved version PBEsol [56], revPBE [57], and RPBE [58]. GGAs give much better results for atomisation energies and enthalpies of formation, compared to LDA [53–55, 59–62]. However, in contrast to LDA, GGAs tend to overestimate the lattice parameters and, thus, may give incorrect results for related properties, like elasticity, phonons, etc. [63].

Even more complex approximations to $E_{xc}[n(\boldsymbol{r})]$ which are aiming at improving over LDA and GGA, comprise meta-GGA's [64, 65], for which the dependence on the kinetic energy density is included, and hybrid functionals [66–68], which use an admixture of exact exchange via the Hartree-Fock formalism.

We use the Perdew-Burke-Ernzerhof functional (PBE96) in this work.

Chapter 4

The TiO_2-Al_2O_3 system

4.1 Introduction

One of the purposes of this chapter is to introduce the experimentally known facts about the TiO_2-Al_2O_3 interface in thin films used as a prototype material for this study. These films were produced at [69, 70] by sputter deposition and analyzed by X-ray diffraction (XRD) and X-ray pole figures methods at [71, 72] as described in [73]. Another aim of this chapter is calculating structural and elastic properties of bulk Al_2O_3 and TiO_2, and comparing them to experimental and theoretical results from literature. At the end of the chapter, results on the atomic stacking at the interface are presented, and a preliminary model of the interface is described.

4.2 Experimental data

It is found in [73] that the only phase of the TiO_2 film deposited on α-Al_2O_3 (0001) substrate is rutile. Moreover, the [100] axis of rutile-TiO2 coincides with the [001] axis of α-Al_2O_3 [73]. The epitaxial relationships established in [73] are $[010]TiO_2 \,||\, [010]Al_2O_3$ and $[001]TiO_2 \,||\, [210]Al_2O_3$. It is noticeable, that the found crystallographic relations allow for a simple geometrical explanation. The graphical representation, obtained using XCrySDen [74], is given in Fig. 4.1. The symmetries of the two lattices are very close to each other. Both of them exhibit hexagon-like patterns of the oxygen and metal (Al, Ti) sub-lattices. Topologically, the coincidence is achieved by placing the rutile-TiO_2 (100) $[00\bar{3}] \times [010]$ supercell [75] on the Al_2O_3 (001) $[210] \times [010]$ one. This leads to the following interface crystallography (adopting the notation by Ashcroft and Mermin [76]): (100) $TiO_2 \,||\,$ (001) Al_2O_3, with [001] $TiO_2 \,||\, \langle 210 \rangle$ Al_2O_3 and [010] $TiO_2 \,||\, \langle 010 \rangle$ Al_2O_3. Since aluminum oxide possesses a three-fold symmetry axis along [001], there are three equivalent ways of matching at this interface.

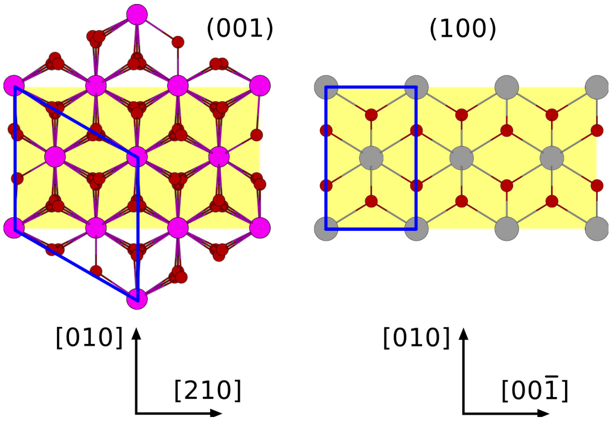

Figure 4.1: Epitaxy of rutile on sapphire. Ball-stick models of $\alpha-Al_2O_3$ (left) and rutile-type TiO_2 (right) crystal structures, viewed along the [001] and [100] axis, respectively. Magenta, red, and gray circles correspond to aluminum, oxygen, and titanium atoms, respectively. The blue frames represent unit-cell borders. The yellow areas denote the units, which allow for coincidence. Reproduced from [73].

4.3 Bulk materials

4.3.1 Computational parameters

The calculations are carried out in the framework of density functional theory (DFT), using the plane-wave ultra-soft pseudopotentials as implemented in the Quantum ESPRESSO [77] code. The PBE GGA [78] exchange-correlation functional is used to account for exchange-correlation effects. The partitioning of electronic shells into pseudo-core/valence is done in the following way: In Ti, $3s^2 3p^6 4s^2 3d^2$ are treated as valence electrons, using the Vanderbilt pseudoization scheme; in Al, the $3s^2 3p^1$ shells are considered as valence states, and the Rappe-Rabe-Kaxiras-Joannopoulos (RRKJ) [79, 80] pseudoization scheme with non-linear core corrections is applied; in O, $2s^2 2p^4$ are dealt with as valence electrons, using the RRKJ pseudoization, again. Other computational parameters are compiled in Table 4.1.

Table 4.1: Computational parameters.

Compound	PW cut-off [Ry]	Density cut-off [Ry]	Monkhorst-Pack mesh
Al_2O_3	35	350	4x4x4 (shifted)
TiO_2	50	500	6x6x9 (shifted)

4.3.2 Al_2O_3

Crystallographic data of the most studied phases of Al_2O_3 is collected in Table 4.2. In addition, there is evindence for the existence of more exotic phases, like β, γ', δ, ϵ, η, κ, κ', μ, and ν [81]. As the substrate used in the process of TiO_2 film growth was α-Al_2O_3, only this phase is considered in further calculations. The crystal structure of α-Al_2O_3 is shown in Fig. 4.2. Wyckoff positions of aluminum and oxygen atoms in the primitive unit-cell of α-Al_2O_3 are given in Table 4.3.

Table 4.2: Phases of alumina (Al_2O_3) together with the corresponding lattice parameters [81].

Phase	Spacegroup	a, b, c [Å]	c/a	α, β, γ
α	$R\bar{3}c$ D_{3d}^6	a=4.7589 c=12.991	2.730	
γ	Fd3m O_h^7	a=7.911		
θ	C2/m C_{2h}^3	a=11.83 b=2.92 c=5.64		β=104.0
λ	Pbmm D_{2h}^5	a=7.63 b=7.63 c=2.89		

The calculated lattice parameters of α-Al_2O_3 are summarized in Table 4.4. Except a slight overestimation of the unit-cell volume, which is typical for GGA, a good agreement with experimental values is found.

Following Ref. [86] we have calculated elastic constants of α-Al_2O_3, which are given in Table 4.5. The deviation from experimental elastic constants is about 10%. One detail has to be mentioned here: the sign of C_{14} was long believed to be negative, but it was recently proved by Gladden et al.[89] to be positive . The value of C_{14} from Ref. [87] is highlighted using bold digits, since in this work a non-standard setup was used, leading to a negative sign.

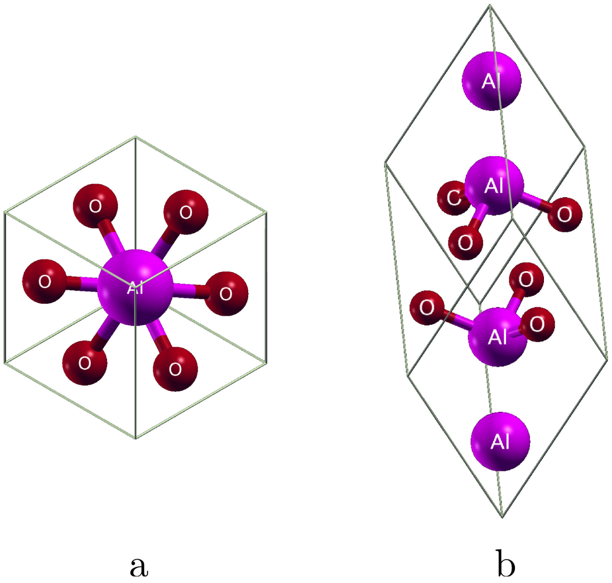

Figure 4.2: Top view (a) and side-view (b) of the unit-cell of α-Al_2O_3.

4.3.3 TiO_2

The most known phases of titanium dioxide are described in Table 4.6. The only phase of TiO_2 found in the thin film is the rutile-phase, thus further calculations are restricted to rutile-TiO_2. Its crystal structure is shown in Fig. 4.3. The Wyckoff positions of the Ti and the O atoms in the primitive unit-cell of rutile-type TiO_2 are presented in Table 4.7, while the corresponding bulk lattice parameters are presented in Table 4.8. The agreement of the lattice parameters calculated in this work with both, experimental and theoretical results present in literature, is again very good, as shown in Table 4.8. Also, the elastic constants of rutile-TiO_2,

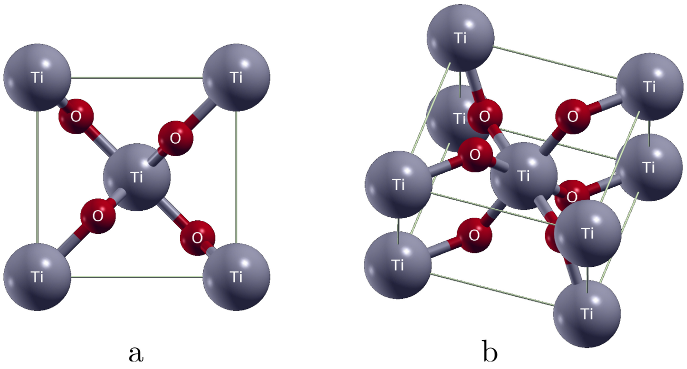

Figure 4.3: Top view (a) and side-view (b) of the unit-cell of rutile-TiO_2.

Table 4.3: Wyckoff positions of atoms in the primitive (rhomobohedral) unit-cell of α-Al_2O_3 (spacegroup #167) [82]. The values of x obtained in this work are the following: x_{Al}=0.35212, and x_O=0.94382.

Atom	Wyckoff position	Multiplicity	Coordinates
Al	c	4	(x, x, x) (-x+1/2, -x+1/2, -x+1/2) (-x, -x, -x) (x+1/2, x+1/2, x+1/2)
O	e	6	(x, -x+1/2, 1/4) (1/4, x, -x+1/2) (-x+1/2, 1/4, x) (-x, x+1/2, 3/4) (3/4, -x, x+1/2) (x+1/2, 3/4, -x)

Table 4.4: Lattice parameters of bulk α-Al_2O_3 in Å. Subscripts hex and rho correspond to hexagonal (conventional) and rhombohedral (primitive) unit cells, respectively.

Source	a_{hex}	c_{hex}	a_{rho}	α_{rho}
Expt. [83]	4.760	12.993	5.129	55.290°
Expt. [84]	4.758	12.990	5.128	55.286°
This work (PBE)	4.782	13.056	5.154	55.281°
Ref. [85] (PBE)	4.800	13.065	5.165	55.433°

which are presented in Table 4.9, are in good agreement with those provided in literature.

4.4 Interface model

To identify possible stackings at the interface, we analyze the atomic-layer stacking of bulk sapphire and rutile. The cross-sections of both oxides are given in Fig. 4.4. The repeat unit of the α-Al_2O_3 stacking along [001] is an -[Al-O-Al]- block. Thus, there are three different terminations possible, when cleaved along (001). For convenience, hereafter they are refered to as A_1, A_2, and A_3, each one corresponding to the crystal below one of the dashed lines in Fig. 4.4. The A_1 or single-Al termination is the stoichiometric one, whereas A_2 (O-termination) and A_3 (double-Al termination) break stoichiometry. The sequence -[O-Ti-O]- is the stacking repeat unit of rutile TiO_2 along [100]. Similar to sapphire, it allows for three possible terminations, upon cleavage along (100). Later we refer to them

Table 4.5: Elastic constants of bulk α-Al_2O_3 in GPa. The boldfaced value is negative due the non-standard setup used in the corresponding reference.

Source	C_{11}	C_{12}	C_{13}	C_{14}	C_{33}	C_{44}
Expt. [87]	495	160	115	**-23**	497	146
Expt. [88]	512	178	149	21	525	146
This work (GGA)	462	144	104	20	466	137
DFT (GGA) [87]	437	144	101	21	443	125

Table 4.6: Phases of titania (TiO_2) together with the corresponding lattice parameters [90].

Phase	Spacegroup	a, b, c [Å]	c/a
Brookite	Pbca D_{2h}^{15}	a=9.1819 b=5.4558 c=5.1429	
Anatase	$I4_1$/amd D_{4h}^{19}	a=3.7852 c=9.5139	2.5134
Rutile	$P4_2$/mnm D_{4h}^{14}	a=4.593659 c=2.958682	0.644080

Table 4.7: Wyckoff positions of atoms in the primitive unit-cell of rutile-TiO_2 (spacegroup #136) [91]. The value of x obtained in this work is 0.30505.

Atom	Wyckoff position	Multiplicity	Coordinates
Ti	a	2	(0, 0, 0) (1/2, 1/2, 1/2)
O	f	4	(x, x, 0) (-x, -x, 0) (-x+1/2, x+1/2, 1/2) (x+1/2, -x+1/2, 1/2)

Table 4.8: Lattice parameters of bulk TiO_2 (rutile) in Å.

Source	a	c	c/a
Expt. [92]	4.582	2.953	0.644
Expt. [93]	4.634	2.991	0.645
This work (PBE)	4.633	2.960	0.638
Ref. [94]	4.639	2.983	0.643

Table 4.9: Elastic constants of bulk rutile-TiO_2 in GPa.

Source	C_{11}	C_{12}	C_{13}	C_{33}	C_{44}	C_{66}
Expt. [95]	267	180	146	479	123	189
Expt. [87]	269	177	146	480	124	192
This work (GGA)	259	170	148	474	115	213
DFT (GGA) [87]	270	172	147	467	115	216

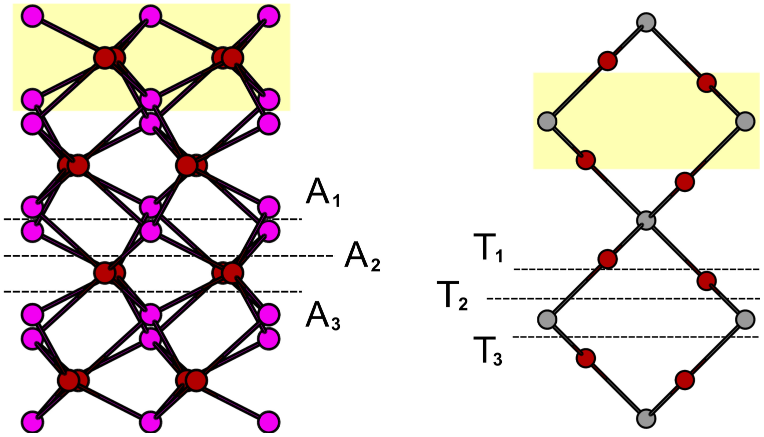

Figure 4.4: Atomic layer stacking in $\alpha-Al_2O_3$ (left) projected onto (210), and in rutile-type TiO_2 (right) projected onto (001). The minimal repeat units are highlighted. Dashed lines indicate possible cleavage planes. Reproduced from [73].

as single-O temination or T_1, Ti-termination or T_2, and double-O termination or T_3. The T_1 maintains stoichiometry, but the latter two are non-stoichiometric. Since each termination of Al_2O_3 can in principle be combined with any termination of TiO_2, there are 9 possible variants of stacking at the interface. However, due to the variance of atomic densities at different planes, some ways of stacking could be selected as more stable *a priori*, because they reveal better atomic coordination at the interface. This observation, based on the crystal chemistry method by Andeen *et al.* [96] allows to reduce the range of considered structures to four sequences, namely, A_2-T_2, A_2-T_3, A_3-T_2, and A_3-T_3. Two atomic-layer arrangements, A_2-T_2 (-Al-Al-O-|-Ti-O-O-) and A_3-T_3 (-O-Al-Al-|-O-O-Ti-), have similar structure, both having bulk-like metal-oxygen-metal stacking, and therefore should have similar properties. The A_2-T_3 (-Al-Al-O-|-O-O-Ti-) stacking is very unfavorable, as it leads to an oxygen aggregate surrounded by metal atoms, which is unlikely due to the highly reactive nature of oxygen. And, finally, A_3-T_2 (-O-Al-Al-|-Ti-O-O-) represents oxygen-poor stacking with loose coordination.

In order to study the different interface structures we use the supercell approach [75]. The supercells are constructed by repeating layers of TiO_2 and Al_2O_3 periodically, thus forming sandwich-like super-lattices, i.e., no vacuum is included. Special care is taken to keep inversion symmetry, since this decreases computation time, allows to avoid dipoles (and therefore dipole corrections), and leads to only one single interface type in the supercell.

The difference between the lattice parameters of the materials forming the interface, also known as the lattice misfit problem, is a source of complications, as we have to construct a supercell, which contains both materials, and fulfills periodic boundary conditions at the same time. The treatment of this problem highly depends on how large the misfit is. Small misfits are commonly considered in the framework of pseudomorphic growth, i.e., the over-layer is supposed to accept the substrate lattice parameters. The supercell of a system with a large misfit, in turn, is constructed by using multiple unit-cells of both counterparts in an appropriate ratio [97]. As to moderate misfits, there is no general approach available so far. In Chapter 5 we introduce an approach, named "*stress balancing*", to cope with the problem. The idea behind the method is to extend the pseudomorphic growth model by taking into account linear elasticity in the most general, i.e., tensorial, description.

4.5 Conclusions

It is established experimentally, that TiO_2 grows as rutile-phase on (001) α-Al_2O_3 substrate. The epitaxial relationships obtained by XRD, and lattice symmetry analysis are the following: (100) TiO_2 || (001) Al_2O_3, with [001] TiO_2 || $\langle 210 \rangle$ Al_2O_3 and [010] TiO_2 || $\langle 010 \rangle$ Al_2O_3.

Structural parameters and elastic conststants of bulk Al_2O_3 and TiO_2 obtained in this work, have shown a good performance of the pseudo-potentials evidenced by reasonable correspondence to available experimental and theoretical results.

Finally, a model of the interface stacking is proposed, that is further used in the following chapters to construct superlattices containing a range of TiO_2-Al_2O_3 interfaces with different atomic stacking. These superlattices are used then to study their thermodynamic, electronic, and mechanic properties.

Chapter 5

Stress balancing method

5.1 Introduction

Lattice misfit plays an important role in film growth. A moderate misfit leads to pseudomorphic growth mode up to a certain critical film thickness, after that misfit dislocations appear [98–100]. Accomodation of high misfit is more complicated. For instance, Erwin and colleagues [101] observed experimentally and explained theoretically a tilt mechanism allowing for an epitaxial interface between materials with strong lattice misfit. The problem of misfit accomodation in atomistic modeling is an issue, especially for superlattices. There is a universal approach [102], that is based on combining multiples of unit-cells of both materials forming the superlattice along each misfit direction such that the misfit strain is minimized. While this method is computationally effective for huge misfits, it becomes prohibitively inefficient for *ab initio* modeling of systems with moderate misfit. Moveover, for some combinations of materials there is no coincidence-site lattice (CSL); therefore, for such systems, any supercell leads to misfit strain. In such cases, an optimal supercell must be constructed in a way, that leads to a minimum of elastic strain energy. Such a method, based on linear elasticity, was proposed for cube-on-cube epitaxy by Van de Walle and Martin [103]. Here, we propose a general approach – termed *stress balancing* – that extends the method of Van de Walle and Martin to any type of epitaxy.

The chapter is organized in the following way: First, a brief explanation of the core idea of the method is given using a one-dimensional mechanical model. Then, the approach is illustrated in three dimensions. After that, the results for TiO_2-Al_2O_3 are presented, and the chapter is concluded.

5.2 One-dimensional case

The easiest way to illustrate the method is to consider the 1D case. Imagine two springs, each with different force constants and lengths, attached to a fixed wall on one side, and to a second wall on the other, movable only in the direction parallel to the springs, as depicted in Fig. 5.1. The equilibrium configuration of the system, i.e., the optimal distance, is defined by the minimum of elastic deformation energy, or, equivalently, by zero net-force (stress). Symbolically it can be represented as follows. The potential energy is

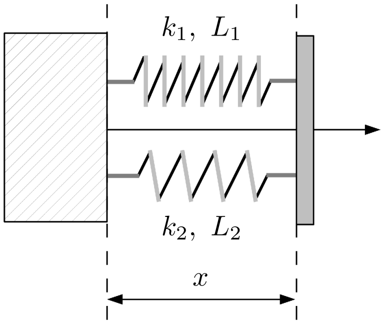

Figure 5.1: One-dimensional illustration of the *stress balancing* approach. Two springs are mounted to a steady wall (left box), and to a movable one (right box). The two springs possess the different force constants k_1 and k_2 (to model different elasticity), and equilibrium lengths L_1 and L_2 (to model a misfit). Reproduced from [73].

$$U(x) = U_1(x) + U_2(x) = \frac{k_1}{2}(x - L_1)^2 + \frac{k_2}{2}(x - L_2)^2. \tag{5.1}$$

Here, k_1 and k_2 are the force constants of the first and the second spring, while L_1 and L_2 are their equilibrium lengths (see Fig. 5.1). The net-force reads

$$\begin{aligned} F = -\frac{dU}{dx} = -\frac{dU_1}{dx} - \frac{dU_2}{dx} = F_1 + F_2 = \\ = k_1(L_1 - x) + k_2(L_2 - x). \end{aligned} \tag{5.2}$$

The equilibrium conditions are

$$U(x_0) = \min U(x), \tag{5.3}$$

and, equivalently,

$$F = F_1 + F_2 = 0. \tag{5.4}$$

The latter condition, i.e., balance of forces (or stresses in the higher-dimensional cases) gives rise to the name of the method. The extension of the method to the 3-dimensional case demands to take the anisotropic nature of elasticity in matter into account. This leads to a slightly more complicated algebra, while, formally, the basic equations of *stress balancing* remain the same and will be described in the following.

5.3 Three-dimensional case: slabs of equal thickness

In three dimensions, we derive equations for a particular type of epitaxy – rectangle-on-rectangle – that is inspired by the TiO_2-Al_2O_3 interface. The method, however, is general and can be applied to any kind of epitaxy. The illustration of the geometrical setup for the *stress balancing* is given in Fig. 5.2. A three-dimensional sketch of the supercell, that contains two parallel slabs in registry to each other is shown in the left panel of Fig. 5.2. In the right panel of Fig. 5.2, there is a scheme of the overlayer and the substrate surfaces projected onto $\boldsymbol{x}_1\boldsymbol{x}_2$-plane, that are depicted as overlayed rectangles. The coherency strains have not been imposed on them yet. These rectangles are completely described in a given cartesian frame by the coordinates of their top right vertices. The dashed line indicates the frame to which both rectangles have to adjust in order to achieve coincidence. Geometrically, the frame is also fully described by its vertex $\boldsymbol{A}(A_1, A_2)$. The directions x_1, x_2, and x_3 in Fig. 5.2 correspond to [001] TiO_2 // ⟨210⟩ Al_2O_3, [010] TiO_2 // ⟨010⟩ Al_2O_3, and [100] TiO_2 // [001] Al_2O_3, respectively.

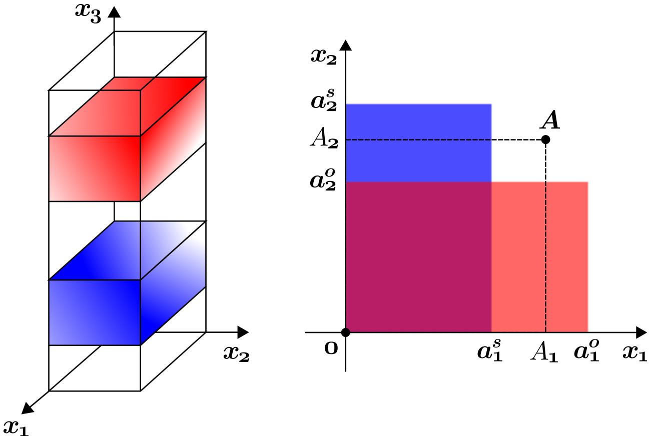

Figure 5.2: Geometrical setup for the illustration of the *stress balancing* method. The left panel contains a three-dimensional sketch of the supercell. On the right, there is an in-plane scheme of the interface with undistorted surfaces of the substrate (blue rectangle) with its vertex coordinates $(a_1^s; a_2^s)$, the overlayer (red rectangle) with vertex coordinates $(a_1^o; a_2^o)$, and the frame (dashed line) with coordinates $(A_1; A_2)$ to which both rectangles have to adjust in order to achieve coincidence. Reproduced from [73].

First, consider the in-plane relations. Since the deformed lattices of substrate and over-layer have to match, it is convenient to write strain equations introducing the two parameters P_1 and P_2, so that $A_1 = a_1^{\mathrm{s}} + P_1(a_1^{\mathrm{o}} - a_1^{\mathrm{s}})$, $A_2 = a_2^{\mathrm{o}} + P_2(a_2^{\mathrm{s}} - a_2^{\mathrm{o}})$. Here, A_1 and A_2 are the in-plane lattice constants of the combined system, and

$0 \leq P_i \leq 1$. Defining the lattice misfits μ_1 and μ_2 as

$$\mu_1 = \frac{a_1^{\mathrm{o}} - a_1^{\mathrm{s}}}{a_1^{\mathrm{s}}}, \tag{5.5}$$

$$\mu_2 = \frac{a_2^{\mathrm{o}} - a_2^{\mathrm{s}}}{a_2^{\mathrm{s}}}, \tag{5.6}$$

$$\tag{5.7}$$

we write down the in-plane strain components for the substrate as follows:

$$\begin{aligned} e_1^{\mathrm{s}} = \frac{A_1}{a_1^{\mathrm{s}}} - 1 = \frac{a_1^{\mathrm{s}} + P_1(a_1^{\mathrm{o}} - a_1^{\mathrm{s}})}{a_1^{\mathrm{s}}} - 1 = \\ = \frac{a_1^{\mathrm{o}} - a_1^{\mathrm{s}}}{a_1^{\mathrm{s}}} P_1 = \mu_1 P_1 \end{aligned} \tag{5.8}$$

$$\begin{aligned} e_2^{\mathrm{s}} = \frac{A_2}{a_2^{\mathrm{s}}} - 1 = \frac{a_2^{\mathrm{o}} + P_2(a_2^{\mathrm{s}} - a_2^{\mathrm{o}})}{a_2^{\mathrm{s}}} - 1 = \\ = \frac{a_2^{\mathrm{o}}}{a_2^{\mathrm{s}}} - P_2 \frac{a_2^{\mathrm{o}} - a_2^{\mathrm{s}}}{a_2^{\mathrm{s}}} - 1 = \mu_2 + 1 - P_2\mu_2 - 1 = \\ = \mu_2 - \mu_2 P_2 = \mu_2(1 - P_2). \end{aligned} \tag{5.9}$$

The corresponding components of the overlayer are:

$$\begin{aligned} e_1^{\mathrm{o}} = \frac{A_1}{a_1^{\mathrm{o}}} - 1 = \frac{a_1^{\mathrm{s}} + P_1(a_1^{\mathrm{o}} - a_1^{\mathrm{s}})}{a_1^{\mathrm{o}}} - 1 = \\ = \frac{a_1^{\mathrm{s}}}{a_1^{\mathrm{o}}} \left(1 + P_1 \frac{a_1^{\mathrm{o}} - a_1^{\mathrm{s}}}{a_1^{\mathrm{s}}}\right) - 1 = \\ = \left(\frac{1}{1+\mu_1}\right) \cdot (1 + P_1\mu_1) - 1 = \frac{\mu_1}{1+\mu_1}(P_1 - 1) \end{aligned} \tag{5.10}$$

$$\begin{aligned} e_2^{\mathrm{o}} = \frac{A_2}{a_2^{\mathrm{o}}} - 1 = \frac{a_2^{\mathrm{o}} + P_2(a_2^{\mathrm{s}} - a_2^{\mathrm{o}})}{a_2^{\mathrm{o}}} - 1 = \\ = P_2 \frac{a_2^{\mathrm{s}} - a_2^{\mathrm{o}}}{a_2^{\mathrm{o}}} = -\frac{a_2^{\mathrm{s}}}{a_2^{\mathrm{o}}} \cdot \frac{a_2^{\mathrm{o}} - a_2^{\mathrm{s}}}{a_2^{\mathrm{s}}} P_2 = -\frac{\mu_2}{1+\mu_2} P_2. \end{aligned} \tag{5.11}$$

The strain components e_3^{s} and e_3^{o} (normal to the interface) are not directly coupled to each other. As to the shear strain components (e_4, e_5, and e_6) of both slabs, they are equal to the supercell shear strain by construction. Applying Hooke's law, all stress components are expressed as follows:

$$\boldsymbol{\sigma}^{\mathrm{s}} = \mathbf{C}^{\mathrm{s}} \cdot \mathbf{e}^{\mathrm{s}} \tag{5.12}$$

$$\mathbf{e}^{\mathrm{s}} = [e_1^{\mathrm{s}} \quad e_2^{\mathrm{s}} \quad e_3^{\mathrm{s}} \quad e_4 \quad e_5 \quad e_6] \tag{5.13}$$

$$\boldsymbol{\sigma}^{\mathrm{o}} = \mathbf{C}^{\mathrm{o}} \cdot \mathbf{e}^{\mathrm{o}} \tag{5.14}$$

$$\mathbf{e}^{\mathrm{o}} = [e_1^{\mathrm{o}} \quad e_2^{\mathrm{o}} \quad e_3^{\mathrm{o}} \quad e_4 \quad e_5 \quad e_6] \tag{5.15}$$

where $\mathbf{e}^{\mathrm{s}}$ ($\mathbf{e}^{\mathrm{o}}$) and $\mathbf{C}^{\mathrm{s}}$ ($\mathbf{C}^{\mathrm{o}}$) are the substrate (over-layer) strain-vector and elasticity matrix, respectively. The equilibrium condition for the supercell is the same as in the 1D case:

$$\boldsymbol{\sigma}^{\mathrm{s}} + \boldsymbol{\sigma}^{\mathrm{o}} = 0 \tag{5.16}$$

In coordinate form, the equation turns to the following set of equations:

$$\begin{aligned}
\sigma_1^{\mathrm{s}} + \sigma_1^{\mathrm{o}} &= 0, && (5.17)\\
\sigma_2^{\mathrm{s}} + \sigma_2^{\mathrm{o}} &= 0, && (5.18)\\
\sigma_3^{\mathrm{s}} &= 0, && (5.19)\\
\sigma_3^{\mathrm{o}} &= 0, && (5.20)\\
\sigma_4^{\mathrm{s}} + \sigma_4^{\mathrm{o}} &= 0, && (5.21)\\
\sigma_5^{\mathrm{s}} + \sigma_5^{\mathrm{o}} &= 0, && (5.22)\\
\sigma_6^{\mathrm{s}} + \sigma_6^{\mathrm{o}} &= 0. && (5.23)
\end{aligned}$$

The different form of equations 5.19 and 5.20 as compared to the rest of equations is the consequence of the geometrical setup – the relaxation along x_3 is not restricted due to the presence of a gap between the slabs. The analysis of the set of equations 5.17 – 5.23 shows that there are 7 variables, namely: P_1, P_2, e_3^{s}, e_3^{o}, e_4, e_5, e_6, and 7 equations. Therefore, the problem is reduced to a 7th order linear system, and it possesses just one solution.

5.4 Three-dimensional case: slabs of different thickness

Equations 5.17 – 5.23 use the assumption of equal thickness of the two slabs forming the superlattice. In the case of different thickness, for instance d_{s} for the substrate and d_{o} for the overlayer, these equations have to be rewritten in the following way

$$\begin{aligned}
w_{\mathrm{s}} \cdot \sigma_1^{\mathrm{s}} + w_{\mathrm{o}} \cdot \sigma_1^{\mathrm{o}} &= 0, && (5.24)\\
w_{\mathrm{s}} \cdot \sigma_2^{\mathrm{s}} + w_{\mathrm{o}} \cdot \sigma_2^{\mathrm{o}} &= 0, && (5.25)\\
\sigma_3^{\mathrm{s}} &= 0, && (5.26)\\
\sigma_3^{\mathrm{o}} &= 0, && (5.27)\\
w_{\mathrm{s}} \cdot \sigma_4^{\mathrm{s}} + w_{\mathrm{o}} \cdot \sigma_4^{\mathrm{o}} &= 0, && (5.28)\\
w_{\mathrm{s}} \cdot \sigma_5^{\mathrm{s}} + w_{\mathrm{o}} \cdot \sigma_5^{\mathrm{o}} &= 0, && (5.29)\\
w_{\mathrm{s}} \cdot \sigma_6^{\mathrm{s}} + w_{\mathrm{o}} \cdot \sigma_6^{\mathrm{o}} &= 0, && (5.30)
\end{aligned}$$

where w_s and w_o are the weight factors defined by the relationships

$$w_\mathrm{s} = \frac{d_\mathrm{s}}{d_\mathrm{s} + d_\mathrm{o}}, \tag{5.31}$$

$$w_\mathrm{o} = \frac{d_\mathrm{o}}{d_\mathrm{s} + d_\mathrm{o}}. \tag{5.32}$$

5.5 Results

Based on the bulk lattice parameters from Section 4.3 and epitaxial relationships discussed in Section 4.2, we determine the lattice misfits of the TiO_2-Al_2O_3 interface. Their values are summarized in Table 5.1. As a next step, we are looking for the supercell geometry with minimum elastic strain energy, by using the bulk elastic properties of substrate and overlayer. The latter relate the stresses to the strains via Hooke's law. In order to express these relations numerically, we transform the bulk elastic tensors to the common coordinate system given by the supercell geometry, applying the following transformation [45]:

$$\tilde{C}_{ijkl} = S_i^p S_j^q S_k^r S_l^s C_{pqrs}. \tag{5.33}$$

Here, C and $\tilde{C}$ are the bulk and slab elastic tensors, respectively, and S is the mapping matrix from the standard bulk to the slab Cartesian coordinate system. Every index (i, j, k, l, p, q, r, s) runs from 1 to 3. The mapping matrices are:

$$S_{\mathrm{Al_2O_3}} = \begin{bmatrix} \frac{\sqrt{3}}{2} & -\frac{1}{2} & 0 \\ \frac{1}{2} & \frac{\sqrt{3}}{2} & 0 \\ 0 & 0 & 1 \end{bmatrix} \quad S_{\mathrm{TiO_2}} = \begin{bmatrix} 0 & 1 & 0 \\ 0 & 0 & 1 \\ 1 & 0 & 0 \end{bmatrix}.$$

Interface structure, bulk lattice parameters, and elastic tensors are the only quantities required as input for the *stress balancing* method. In principle, whenever possible one has to use the flavor of the method that allows to take into account the ratio between the thicknesses of slab of the overlayer and the substrate as described in Section 5.4. However, here the modification of the method is used, that assumes equally thick slabs of the overlayer and the substrate, employing derivations from Section 5.3. It is done this way in order to ensure a common framework (fixed in-plane lattice parameters) for the convergence studies of the work of separation as a function of slab thickness. The numerical values as resulting from the method are provided in Table 5.2.

5.6 Conclusions

In this chapter, an approach named *stress balancing* was introduced to cope with the problem of the lattice misfit. The method was applied to construct a TiO_2-

Table 5.1: The lattice misfit along the ith direction ($i = 1, 2$), $\mu_i = (a_i^{\mathrm{o}} - a_i^{\mathrm{s}})/a_i^{\mathrm{s}}$, where superscripts "s" and "o" correspond to the lattice parameters of substrate and overlayer, respectively. For Al_2O_3 the lattice parameters of the conventional (hexagonal) unit cell are used.

Direction i	1	2
	$[00\bar{1}]TiO_2 \,\|\|\, \langle 210\rangle Al_2O_3$	$[010]TiO_2 \,\|\|\, \langle 010\rangle Al_2O_3$
a_i^s	$\sqrt{3} \times a_{Al_2O_3}$	$a_{Al_2O_3}$
a_i^o	$3 \times c_{TiO_2}$	a_{TiO_2}
μ_i [%]	7.2	-3.1

Table 5.2: Supercell parameters leading to minimal strain energy according to the *stress balancing* model. The symbols e_3^s and e_3^o are used for the strain components normal to the interface of substrate and over-layer slabs, respectively.

a [Bohr]	b [Bohr]	e_3^{s}	e_3^{o}	α	β	γ
16.171	8.930	0.9952	1.0075	89.85°	90.00°	90.00°

Al_2O_3 superlattice, which is a prototype model for studying the properties of the $TiO_2(100)$-$Al_2O_3(001)$ interface.

Before starting with the evaluation of the work of separation, the electronic, and the mechanical properties, the atoms of the constructed superlattice should be relaxed, and the optimal interslab spacing should be defined. The results of relaxation are presented in the next chapter.

Chapter 6

Optimization of the interface structure

6.1 Introduction

Before computing and evaluating interface properties, the equilibrium structure has to be obtained by minimizing the forces that act on the atoms within the considered supercell. The results of such relaxation are presented and discsussed in this chapter. The optimal structures are characterized in terms of radial and angular distributions of atoms. The chapter ends with concluding remarks.

6.2 Results

After obtaining the equilibrium supercell geometry from *stress balancing*, the inter-slab separation, i.e., the distance between two slabs, is optimized for each considered stacking using two approaches – *static* and *relaxed* – which give us the *static separation* and the *relaxed separation*, respectively. The *static separation* is found, when all atoms of each slab are kept fixed to maintain the structural arrangement of the bulk materials, i.e., only the distance itself is varied. The *relaxed separation* is obtained allowing four atomic layers from each side of both slabs to relax. To optimize the atomic positions, we use the BFGS method [104].

Table 6.1: Optimal inter-slab separations (Δ) for different stacking.

Stacking	A_2-T_2	A_2-T_3	A_3-T_2	A_3-T_3
Δ (*static*) [bohr]	2.47	2.86	4.49	1.49
Δ (*relaxed*) [bohr]	2.49	2.65	3.96	1.39

The value of the inter-slab separation that minimizes the total energy is called optimal. The optimal values of inter-slab separation are shown in Table 6.1. The results of atomic relaxation are presented and discussed in the next sections.

6.2.1 A first view

The relaxed interface structures are presented in Fig. 6.1. As predicted in Section 4.4, two ways of stacking (A_2-T_3 and A_3-T_2) that lead to an under-coordination of interface atoms reveal strong relaxation. It is interesting to note a few features of A_2-T_3 and A_3-T_2: 1) In the course of relaxation, the double-O-terminated titanium dioxide slab of A_2-T_3 becomes almost a single-O-terminated one, as shown in Fig. 6.1b. 2) According to Fig. 6.1d, the metal-to-metal stacked A_3-T_2 demonstrates a repulsion of Ti atoms from the double-Al-terminated Al_2O_3 slab, so to maintain an average bond-length of approximately 5.0 Bohr. 3) Even after relaxation both structures possess poor coordination, and therefore weak binding. A_2-T_2 and A_3-T_3 relax in a similar manner, that differs from the manner of A_2-

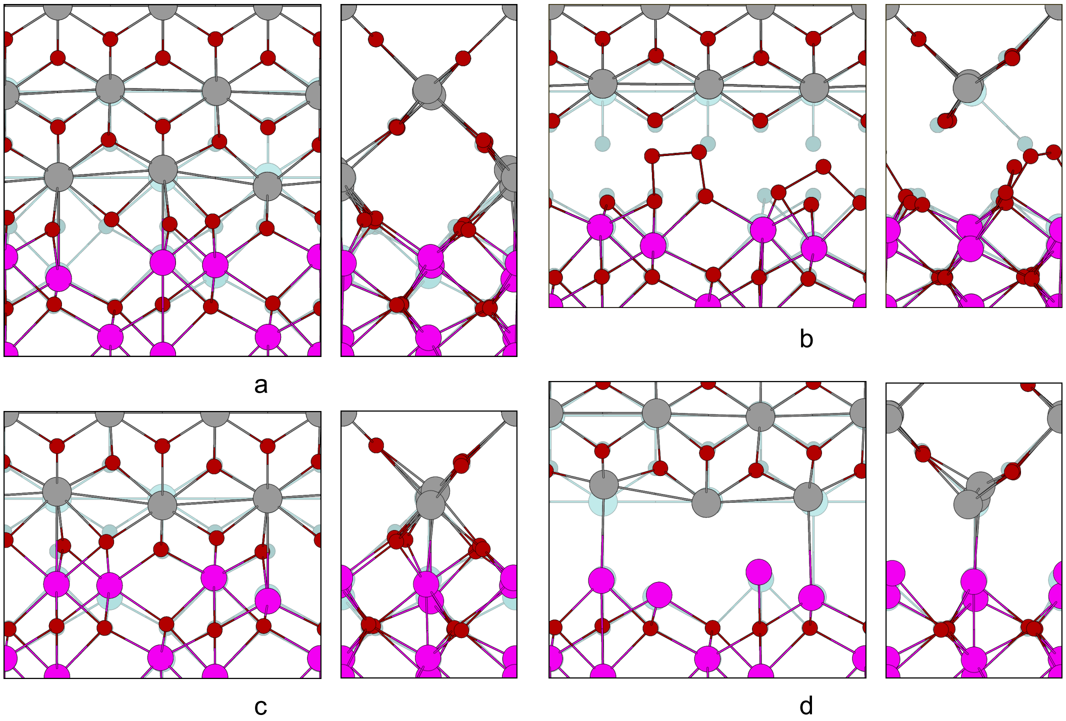

Figure 6.1: Relaxation of the A_2-T_2 (a), A_2-T_3 (b), A_3-T_3 (c), and A_3-T_2 (d) structures from 2 different projections. The structure in the background (foreground) corresponds to the initial (optimized) geometry. Atomic species are shown in different color: Al(magenta), Ti(grey), and O(red). Reproduced from [73].

T_3 and A_3-T_2. Here, the Ti-layer closest to the interface experiences a wave-like relaxation, at the same time the Al double-layer is affected at most locally.

6.2.2 Relaxation profiles

Visual inspection of the results of relaxation gives us an idea about the most prominent stacking at the interface, i.e., the one, which leads to the best coordination and, thus, compact arrangement of atoms. There are 2 favorites identified, namely, A_2-T_2 and A_3-T_3. The next step is to quantify the relaxation. The simplest property to look at is the atomic displacement. For an atom α the displacement is defined as

$$\boldsymbol{\delta}^{\alpha} = [\delta_x^{\alpha}\ ,\ \delta_y^{\alpha}\ ,\ \delta_z^{\alpha}] = [x_{opt}^{\alpha} - x_0^{\alpha}\ ,\ y_{opt}^{\alpha} - y_0^{\alpha}\ ,\ z_{opt}^{\alpha} - z_0^{\alpha}] = \boldsymbol{r}_{opt}^{\alpha} - \boldsymbol{r}_0^{\alpha},$$

where $\boldsymbol{r}_0^{\alpha}$ and $\boldsymbol{r}_{opt}^{\alpha}$ are the initial and the optimized positions of the considered atom. We can investigate the displacements of any single atom within the cell using $\boldsymbol{\delta}$'s; however, they are not convenient to quantize the relaxation of all atoms at once, i.e., to see the whole picture of relaxation. Instead, we can use these values to calculate the net relaxation profile (a vectorial function)

$$\boldsymbol{\Delta}(z) = [\Delta_x(z)\ ,\ \Delta_y(z)\ ,\ \Delta_z(z)] = \frac{1}{N_z}\sum_i^{N_z} \boldsymbol{\delta}^{\alpha_i}, \quad z_0^{\alpha_i} = z,$$

where N_z is the number of atoms in the cell, whose z-component of the initial position, i.e., z_0 is equal to z (argument of the function). The norm, or the length of $\boldsymbol{\Delta}(z)$, i.e., $||\boldsymbol{\Delta}(z)||$ describes the average net relaxation as a function of z (the direction perpendicular to the interface). The components of $\boldsymbol{\Delta}(z)$, i.e., $\Delta_x(z)$, $\Delta_y(z)$, and $\Delta_z(z)$ show the average net displacements of atoms along the corresponding axis (x, y, or z). Another useful function is the net absolute relaxation profile (a scalar function)

$$|\Delta|(z) = \frac{1}{N_z}\sum_i^{N_z} ||\boldsymbol{\delta}^{\alpha_i}||, \quad z_0^{\alpha_i} = z,$$

which is defined in almost the same way as $\boldsymbol{\Delta}(z)$, except that the $\boldsymbol{\delta}$'s are substituted by their norm, i.e., by $||\boldsymbol{\delta}||$. The net absolute relaxation profile show us how much relaxation happens at every atomic layer, i.e., how far the atoms move from their initial positions in average.

The relaxation profile of A_2-T_2 is given in Fig. 6.2. $|\Delta|(z)$ is confined by the fixed atomic layers from both sides of the interface, it rises when approaching the IF and is slightly above 0.2 Å for oxygen atoms situated right at the IF. The components of $\boldsymbol{\Delta}(z)$ evolve differently. There are just slight changes in the x-component of atoms across the interfacial region. In contrast, the y- and z-components change significantly, though the shape of the y-component is similar to the shape of $\mathrm{sinc}(z) = \sin(z)/z$, while the the shape of the z-component is sawtooth-like.

There are similarities to A_2-T_2 in the character of relaxations exhibited by A_3-T_3 as shown in Fig. 6.2. Here, the biggest peaks of $|\Delta|(z)$ appear in the layers a bit away from the interface itself. In TiO_2, the largest peak is on the oxygen layer next to the interface. In Al_2O_3, the biggest relaxations are observed in the second aluminum layer away from the interface. Despite the fact that the x-component of $\boldsymbol{\Delta}(z)$ hardly differs from zero as for A_2-T_2, it should be noted that the shapes of the y- and z-components are different. As compared to A_2-T_2, the relaxation of A_3-T_3 in the y- and z-direction is more pronounced in the titanium dioxide part.

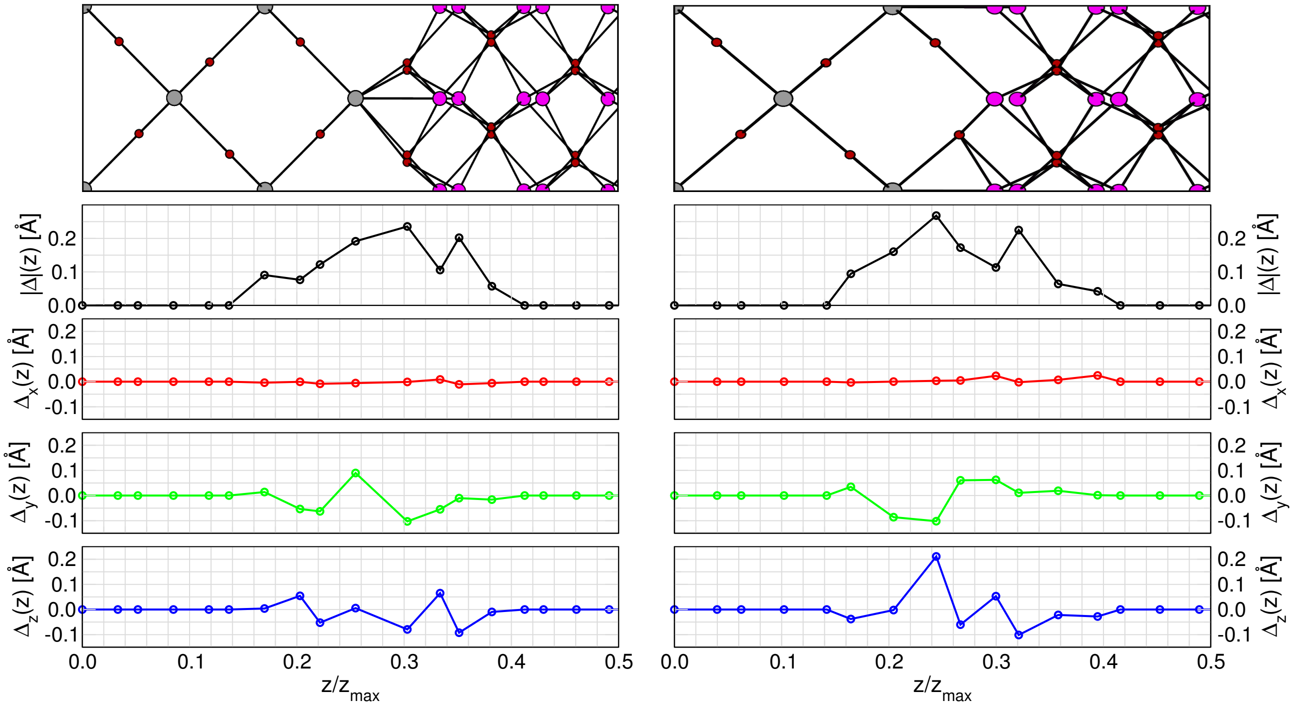

Figure 6.2: Relaxation profiles of the A_2-T_2 (left) and the A_3-T_3 (right) structures. The sketch of A_3-T_3 (top right) is intentionally compressed along the vertical axis to make the whole figure compact.

6.2.3 Radial distribution functions

The analysis of relaxation profiles demonstrated a complex relaxation behavior, which occurs in the vicinity of the interface. It is quite natural, then, to ask the following question: How does the relaxation affect the local geometry? To to answer this question, we investigate *the first coordination polyhedra*. Here, we define *the first coordination polyhedron* as the group of atoms surrounding the selected one, provided all these atoms are enclosed in a sphere of a certain radius. This radius is characteristic for every substance. A few notes have to be given here. First of all, according to the definition, a coordination polyhedron can be formed by a few smallest coordination spheres, as depicted in Fig 6.3. To remind, a coordination sphere is a group of atoms situated sharply at a certain distance from the central atom. The second note follows from the first one – the definition of the coordination number of a coordination polyhedron used in this work is different from the definition of the coordination number of a coordination sphere. Indeed, the coordination number of the first coordination polyhedron is the sum of the coordination numbers of the coordination spheres enclosed in this polyhedron.

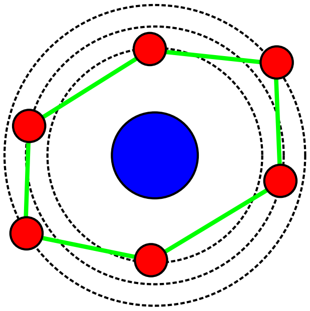

Figure 6.3: Two-dimensional sketch of a coordination polyhedron; its border is marked by the closed green line. First three coordination spheres are shown as concentric dashed circles. Each of the spheres hosts two red atoms, while the whole polyhedron is built of the central blue atom surrounded by six red atoms.

The building blocks of both oxides forming the interface are distorted O-M-O octahedra, where M=Al,Ti, as depicted in Fig. 6.4. The distances between the metal atom in the center and the surrounding oxygen atoms can be analyzed using the radial distribution function (RDF)

$$g(r) = \frac{1}{\rho_n}\frac{dn(r)}{dV(r)}, \tag{6.1}$$

where ρ_n is the average particle density, i.e., the number of particles per unit-volume, $dn(r)$ is the differential of the number of particles in a spherical shell

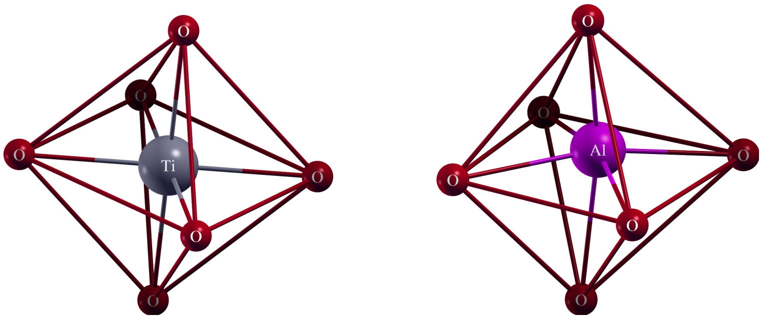

Figure 6.4: Three-dimensional view of oxygen-metal-oxygen octahedra, forming TiO_2 (left) and Al_2O_3 (right).

of radius r, and $dV(r) = 4\pi r^2 dr$ is the differential of the corresponding volume. In order to clarify the physical meaning of $g(r)$, it is convenient to rewrite equation 6.1 in the following form:

$$dn(r) = \rho_n g(r) dV(r). \tag{6.2}$$

If we integrate this equation from $r = r_0$ to $r = r_0 + \Delta r$, where Δr is an infinitesimal increment of r, we get:

$$\int_{r_0}^{r0+\Delta r} dn(r) = \rho_n \int_{r_0}^{r0+\Delta r} g(r) dV(r). \tag{6.3}$$

The left part of the equation turns simply to:

$$n(r_0 + \Delta r) - n(r_0) = \Delta n(r_0). \tag{6.4}$$

For the right part, we get:

$$\rho_n \int_{r_0}^{r0+\Delta r} g(r) dV(r) = \rho_n g(\zeta) \int_{r_0}^{r0+\Delta r} dV(r) = \tag{6.5}$$

$$= \rho_n g(\zeta) \left[V(r_0 + \Delta r_0) - V(r_0) \right] = \rho_n g(\zeta) V_{shell} = \tag{6.6}$$

$$= g(\zeta) \left(\rho_n \cdot V_{shell} \right) = g(\zeta) N_{shell}, \tag{6.7}$$

where $r_0 \leq \zeta \leq r_0 + \Delta r$, V_{shell} is the volume of the spherical shell ranging from r_0 to $r_0 + \Delta r$, and N_{shell} is the number of particles, which would be enclosed in the volume V_{shell} of a media with the constant average particle density ρ_n. Now, we put both parts together:

$$\Delta n(r_0) = g(\zeta) N_{shell}, \tag{6.8}$$

$$g(\zeta) = \frac{\Delta n(r_0)}{N_{shell}}, \tag{6.9}$$

or, approximately:

$$g(r_0) \approx \frac{\Delta n(r_0)}{N_{shell}}. \tag{6.10}$$

Thus, the radial distribution function acts as an enhancement factor – it defines the ratio between the true number of particles in a spherical shell as shown in Fig. 6.5 and the number of particles within the same shell in uniform and continuous media with the average particle density ρ_n. The shape of $g(r)$ reflects the spatial ordering in the substances. For instance, the RDF of an ideal lattice would look like a sum of sharp peaks at the radii of coordination spheres. The RDF is widely used for structural analysis of amorphous materials, like glasses or liquids, in order to invesigate short-range order and clustering. If for a multi-component system only 2 kinds of particles are considered, e.g., the distribution of atoms of type A around atoms of type B, then the so calculated RDF is called *partial RDF*. We use the RDF in order to study the changes of the radial distribution of oxygen-atoms in the first coordination polyhedra in both oxides. It is convenient for our purposes to analyze $\Delta n(r)$ instead of $g(r)$ itself, as it makes the calculation of coordination numbers straightforward. $\Delta n(r_{M-O})$ is evaluated in the range of 1.6-2.6 Å (the metal-oxygen bond-length in the bulk oxides is 1.8-2.0 Å), with a resolution of $\Delta r = 0.1$ Å. In order to investigate the dependence of the parameters of the polyhedra on the distance from the IF, for each M-atom in a layer we calculate $\Delta n(r_{M_i-O})$, then average over all (4 for Al-layers, 3 for Ti-layers) polyhedra of the considered layer, yielding $\langle\Delta n(r_{M-O})\rangle_{L_j}$. These layers are denoted as follows: L_1 corresponds to the M-layer closest to the IF, L_2 refers to the second-closest one, and L_3 to the third-closest M-layer.

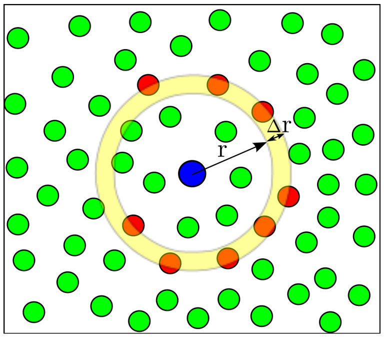

Figure 6.5: Illustration of calculation of radial distribution function in 2-dimensions. The central atom (blue) is considered as origin; it is surrounded by a circular shell (from r to $r + \Delta r$), highlighted in yellow. An atom is colored red, if its center falls into the yellow shell.

The layer-averaged radial distributions for the Al_2O_3 part of the IF are given in Fig. 6.6. $\langle\Delta n(r_{Al-O})\rangle_{L_3}$ of both the A_2-T_2 and the A_3-T_3 structures are exactly

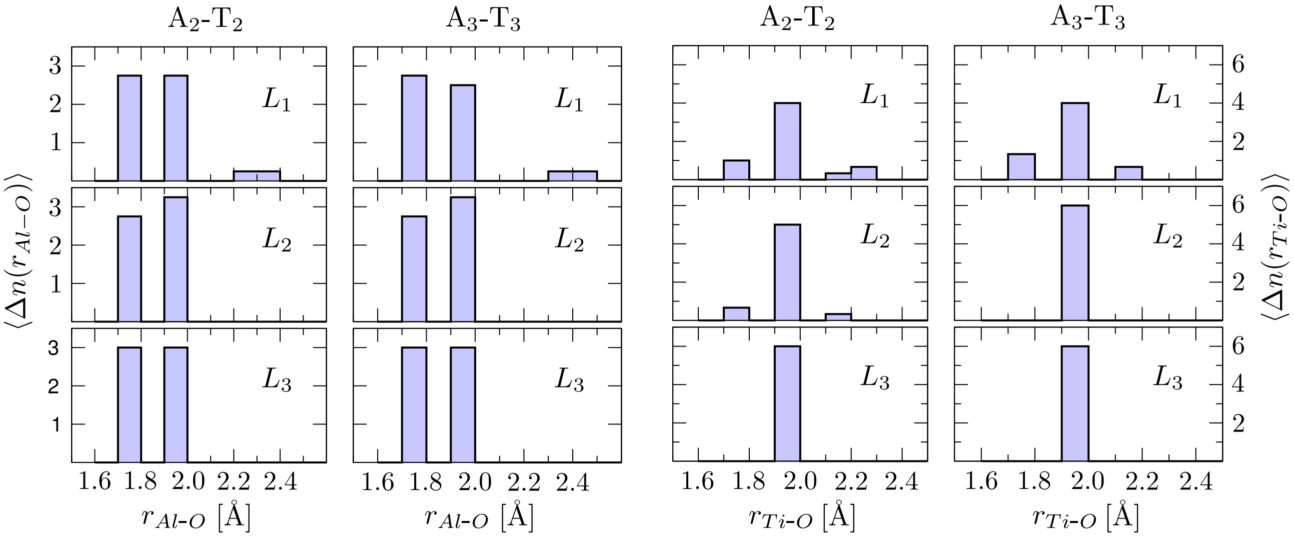

Figure 6.6: Layer-averaged radial distribution of O atoms around Al (left) and Ti (right) atoms. Reproduced from [73].

the same, they represent the strained-bulk state of Al_2O_3. The natural splitting between the first and the second coordination spheres, forming the deformed octahedra (6 O atoms around the Al), is enhanced by the strain imposed by the *stress balancing*. Coming closer to the IF results in a redistribution of O atoms between the first two coordination spheres in favor of the second one, i.e., the coordiantion polyhedra are getting stretched, which is reflected in the value of $\langle \Delta n(r_{Al-O}) \rangle_{L_2}$. The polyhedra situated next to the IF experience the strongest deformation as indicated by $\langle \Delta n(r_{Al-O}) \rangle_{L_1}$. Some of the M-O bonds have length of 2.2-2.4 Å (A_2-T_2) or even 2.3-2.5 Å (A_3-T_3). The coordination number for A_2-T_2 remains the same as for the bulk, i.e. 6. On the contrary, the coordination number for A_3-T_3 is 5.75, which is an indication of a less compact structure.

The layer-averaged radial distributions for the TiO_2 part of the IF are given in Fig. 6.6. As for aluminum oxide, L_3 represents the distribution of O atoms in the strained bulk of TiO_2. The splitting between the first two coordination spheres, also forming the deformed octahedra (6 O atoms around the Ti), in TiO_2 is smaller than in Al_2O_3. Even though altered by the strain, it is not resolved with the applied resolution, such that there is just one peak at 1.9-2.0 Å. As for A_3-T_3 the Ti atoms and their closest neighbors in L_2 were fixed during the relaxation, the distrubution function remains the same as for L_3. $\langle \Delta n(r_{Ti-O}) \rangle_{L_2}$ of the A_2-T_2 shows a splitting around the main peak, i.e., some of the M-O bonds became shorter (1.7-1.8 Å), some of them turned longer (2.1-2.2 Å). In the vicinity of the IF, i.e., in L_1, $\langle \Delta n(r_{Ti-O}) \rangle_{L_1}$ of both A_2-T_2 and A_3-T_3 demonstrate significant redistribution of M-O bondlengths, which is more pronounced in the case of A_2-T_2.

6.2.4 Angular distribution functions

The second property we analyze is the distribution of the oxygen-metal-xygen valence angles in the first coordination polyhedra. An example of such angles is shown in Fig. 6.7.

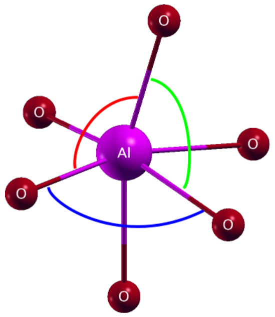

Figure 6.7: Illustration of oxygen-metal-oxygen valence angles in the first coordination polyhedra of Al_2O_3. The angles are indicated with colored arcs.

Like for radial distribution functions analysis, here we analyze only the most prominent structures, i.e A_2-T_2 and A_3-T_3, in the range of 70^o to 110^o. The emphasis of the analysis is, especially, put on the development of the O-M-O distributions as functions of the distance to the interface. Consider the O-Al-O distributions, which are presented in Fig. 6.8. First, comparing unstrained bulk Al_2O_3 and aluminum oxide in L_3, the changes brought by the *stress balancing* have to be noted. Due to introduced strain a splitting takes place about the position of unstrained-bulk peaks. Second, further splitting happens in L_2 of A_2-T_2 and A_3-T_3, which is caused here not only by the imposed strain, but it is also a consequence of structure relaxation. Third, in the interface region, i.e., in L_1, one can see the biggest variety of O-Al-O angles, which is more pronounced in the case of A_3-T_3. It supports the hypothesis of the less compact structure at the interface region of A_3-T_3 as compared to A_2-T_2. Further, we look at the O-Ti-O distributions depicted in Fig. 6.9. Again, the effect of strain imposed by the *stress balancing* can be seen, when comparing the distributions in unstrained-bulk TiO_2 and L_3. It is remarkable, that this strain drives polyhedra in titanium dioxide of L_3 closer to ideal octahedra, i.e, O-Ti-O angles are shifted towards 90^o. There is a quite big difference in the shapes of distributions in L_2 between A_2-T_2 and A_3-T_3, especially in the intensities of peaks. This difference arises, most likely, from the fact that in case of A_2-T_2 less atoms around and in L_2 were fixed in the course of relaxation as compared to A_3-T_3. As for Al_2O_3 the biggest spread of O-Ti-O angles is detected in L_1. The intensities of peaks in the case of A_3-T_3 are higher, than in A_2-T_2 due to the same reason as for L_2. The range of O-Ti-O angles is wider for A_3-T_3, which is yet another indication that this structure is less compact in the interface region than A_2-T_2.

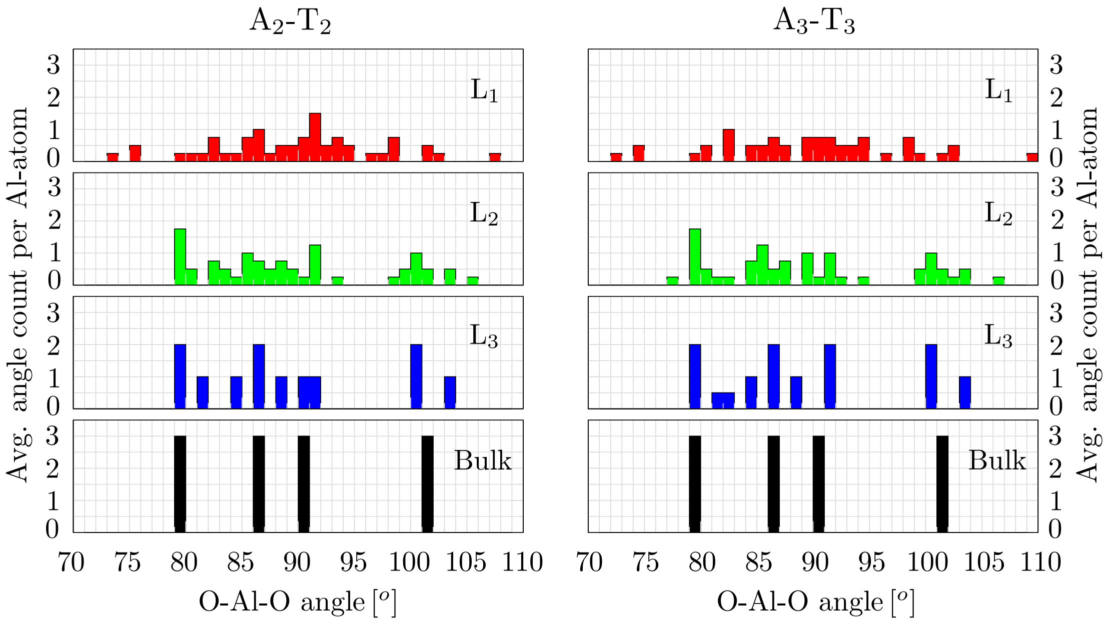

Figure 6.8: Distribution of O-Al-O valence angles in A_2-T_2 (left) and A_3-T_3 (right). The bottom panels depict the unstrained bulk (as optimized in this work).

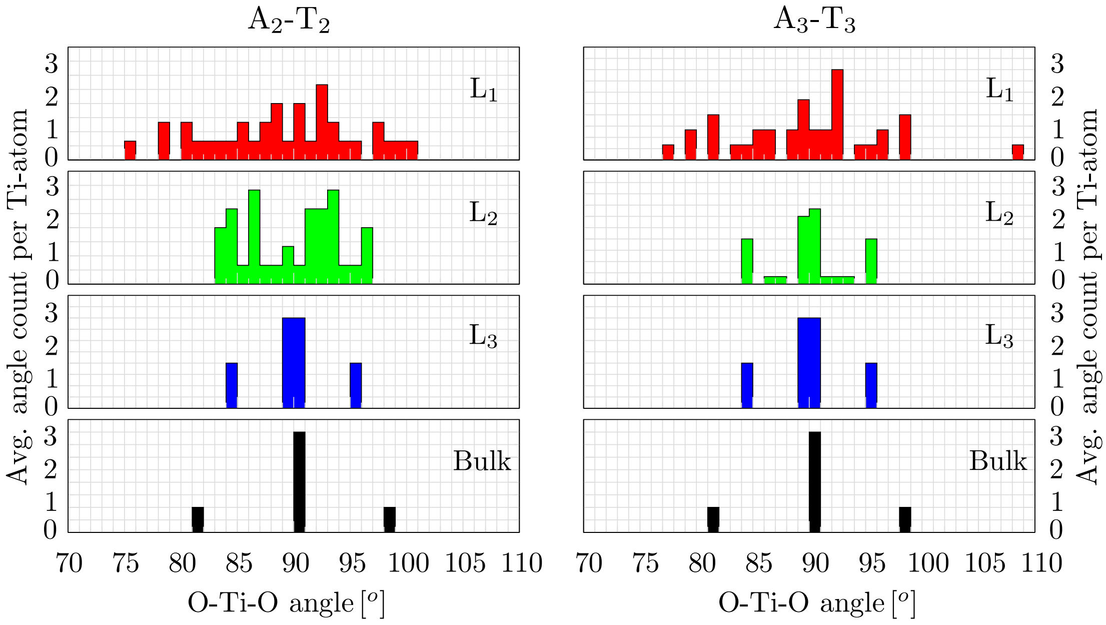

Figure 6.9: Distribution of O-Ti-O valence angles in A_2-T_2 (left) and A_3-T_3 (right). The bottom panels depict the unstrained bulk (as optimized in this work).

Now, we consider the individual polyhedra in each M-layer, and restrict the analysis to the smallest and the largest angles. These angular distributions are presented in Fig. 6.10. In L_3 of both oxides the splitting between the maximal and the minimal angles reflects the structural properties of the strained bulk oxides. In L_2 a spread of 3-5^o is found about the angles in L_3. In the vicinity of the IF, there is a broad variety of angles, which is more pronounced in the Al_2O_3 slab. In general, the difference between the distributions in the A_2-T_2 and the A_3-T_3 strucutres is minor, except the range of the maximal angles in the first M-layer of TiO_2, which is larger in the case of A_3-T_3. Comparing the layer-averaged trends in the IF counterparts, we note two features. First, approaching the IF, both lines are getting close to each other, so that the total line looks smooth across the IF. Second, the values of the lines in L_1 are quite close to those of the unstrained bulk oxides, which may be a sign of strain-relief at the IF.

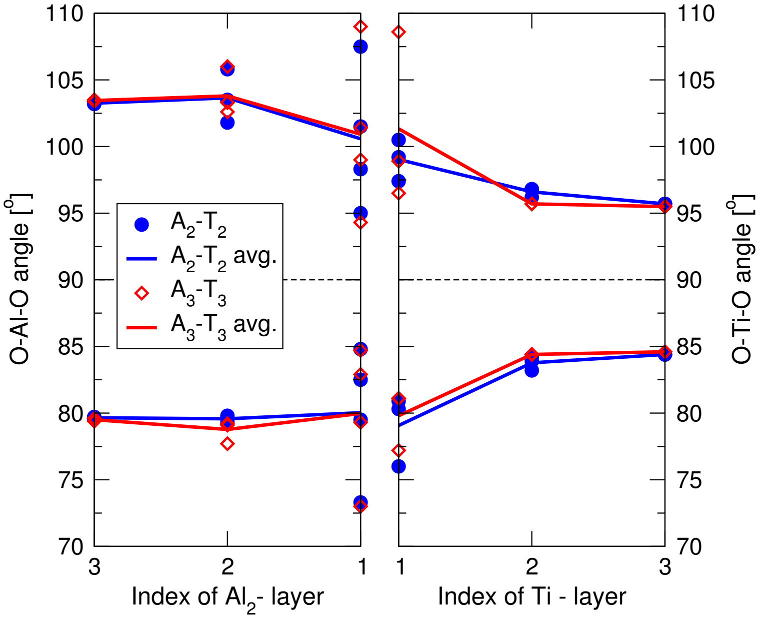

Figure 6.10: Distributions of minimal (below 90^o) and maximal (above 90^o) O-M-O (M=Al,Ti) angles in the first coordination polyhedra. The solid lines provide the layer-averaged values. The filled blue circles and lines represent A_2-T_2, the empty red diamonds and lines A_3-T_3. Reproduced from [73].

6.3 Conclusions

The optimal static and relaxed interslab separations are found for all considered atomic stacking (shown in Table 6.1). Also, the relaxed atomic structures are obtained and the most compact ones are identified (A_2-T_2 and A_3-T_3). These structures are analyzed in terms of relaxation profiles, partial radial- and angular-distribution functions of O atoms in the first coordination polyhedra around the Al and Ti atoms.

According to the relaxation profile analysis most of the atomic rearrangement happens in the atomic layers situated right at the interface. The atoms here move from their bulk position in average by about 0.20-0.27 Å.

The analysis of partial radial distribution functions reveals a variety of bondlengths at the interface. Bonds that are both shorter and longer than in the bulk oxides are found. It is identified, also, that the average coordination numbers of the Al and Ti atoms at the interface are 6 for A_2-T_2 (the same as for bulk), 5.75 (for Al) and 6 (for Ti) for A_3-T_3. Thus, the stacking of A_2-T_2 leads to the most compact structure among all considered stacking sequences, which is supported by the analysis of the angular distribution functions.

Relaxation of superlattices with A_2-T_2, A_2-T_3, A_3-T_2, and A_3-T_3 stacking and the consequent structural analysis allows for identifying the A_2-T_2 stacking as the structurally most stable one. It leads to the most compact structure, that maintains the metal-oxygen-metal stacking natural for both oxides, as well as the coordination number (6) of the O atoms around the Al an Ti atoms. The relaxed superlattice structures are used in the next chapters to evaluate a range of interface-related properties.

Chapter 7

The work of separation

7.1 Introduction

The work of separation is a measure of bonding strength at the interface. Even though it is a zero-Kelvin property, it can be used as an ingredient for evaluating the interface energy at finite temperature and in different of chemical environments, following the approach proposed by Finnis and co-workers [105]. In first-principles calculations, the work of separation can be obtained by the formula

$$W_{\mathrm{sep}} = \frac{1}{2A}[E_{\mathrm{tot}}^{\mathrm{ss}} + E_{\mathrm{tot}}^{\mathrm{ol}} - E_{\mathrm{tot}}^{\mathrm{sc}}], \tag{7.1}$$

where A is the interface area, and $E_{\mathrm{tot}}^{\mathrm{ss}}$, $E_{\mathrm{tot}}^{\mathrm{ol}}$, and $E_{\mathrm{tot}}^{\mathrm{sc}}$ are the total energies of the substrate, the overlayer, and the entire super-cell comprising the interface, respectively. In our case, the substrate is the aluminum oxide slab, and the overlayer is the titanium oxide slab.

7.2 Computation method

The work of separation was calculated here in two ways. The first one, which we call *static*, was performed using the optimal slab separation for frozen atomic positions of the superlattice. Accordingly, no relaxation was allowed for individual slabs. The second method, which we call *relaxed*, uses the optimal interface separation, while a constrained atomic relaxation of the superlattice was allowed. Each of the slabs was relaxed with the analogous constraints (4 outermost atomic layers from each side of a slab).

In order to avoid computational artefacts when calculating the energies of the isolated slabs, we always keep the unit cell parameters of the full superlattice, removing all the atoms that do not belong to the considered slab.

7.3 Results

The values of the work of separation calculated in this work are presented in Table 7.1. All of them are obtained using a cut-off energy of 30 Ry and a shifted 2x4x1 mesh of points in the Brillouin zone (4 points in the IBZ). The results of a convergence study are presented in Section 7.4.

Table 7.1: The ideal work of separation. The superscripts "static" and "relax" correspond to the work of separation of unrelaxed and relaxed structure, respectively. The error bar is ~60 mJ/m^2.

Interface	Stacking	$W_{\rm sep}^{\rm static}$ [J/m^2]	$W_{\rm sep}^{\rm relax}$ [J/m^2]
A_2-T_2	-Al-Al-O-|-Ti-O-O-	10.15	9.31
A_2-T_3	-Al-Al-O-|-O-O-Ti-	0.35	0.45
A_3-T_2	-O-Al-Al-|-Ti-O-O-	2.26	1.58
A_3-T_3	-O-Al-Al-|-O-O-Ti-	10.33	8.84

As expected from their structural similarity, the works of separation of A_2-T_2 and A_3-T_3 are close to each other, slightly favoring A_2-T_2. The work of separation of oxygen-rich A_2-T_3 is one order of magnitude smaller, compared to the previous structures, but still positive. The metal-to-metal interface, A_3-T_2, reveals a relatively weak bonding, though much stronger than the oxygen-rich one.

7.4 Convergence studies

One of the most important questions, when dealing with numerical methods, is the question of reliability of the obtained results. To see what can affect the precision of our results, let us recall Eq. 7.1. It is clear, that the precision of $W_{\rm sep}$ is limited by the precision of the total energies of substrate, overlayer, and superlattice, or, to be more precise, it depends on the precision of their linear combination. Such a linear combination usually converges faster than any of its components. Numerical evaluation of total energies relies upon many technical aspects, and there are two most critical among them. The first one is the use of a truncated series for the wavefunction expansion, which is controlled by cut-off energy. The second one, is the substitution of integrals over the Brillouin zone by weighted sums over special points within the Brillouin zone.

The work of separation as defined by equation 7.1 can be calculated using slabs of different thickness. Therefore, for each combination of substrate and overlayer slab thickness, we will get a different work of separation, unless both of the slabs are thick enough. This value of the work of separation is our target. Equation 7.1

can be formally rewritten into a system of equations

$$W_{\mathrm{sep}}(n,m) = \frac{1}{2A}[E^{\mathrm{ss}}_{\mathrm{tot}}(m) + E^{\mathrm{ol}}_{\mathrm{tot}}(n) - E^{\mathrm{sc}}_{\mathrm{tot}}(m+n)], \tag{7.2}$$

$$W_{\mathrm{sep}} = \lim_{\substack{n\to\infty \\ m\to\infty}} W_{\mathrm{sep}}(m,n), \tag{7.3}$$

where the numbers m and n quantify the thickness of the slabs, i.e., they are connected to the number of atomic layers within each slab. It turns out that reasonable convergence is achieved at rather small finite thickness.

Overall, we have to investigate the convergence of W_{sep} with respect to:

- BZ-sampling
- Cut-off energy
- Slab thickness

To this end, we make convergence tests of the unrelaxed W_{sep} of A_3-T_3 using Δ, i.e., an inter-slab spacing, of 1.39 bohr. As the considered interfaces differ mainly in atomic stacking at the interfacial region, it seems reasonable to presume, that once the parameters leading to the desired accuracy are found for one particular stacking, e.g., A_3-T_3, they can be used for the rest of stacking variants, too.

7.4.1 Brillouin zone sampling

To test the convergence of W_{sep} of A_3-T_3 with respect to the BZ-sampling, a superlattice built of an A_3 slab with 14 atomic-layers and a T_3 slab of 17 atomic-layers was employed. The uniform sampling of the Brillouin Zone was performed using the standard approach of Monkhorst and Pack [106]. All used meshes were shifted. One can see in Fig. 7.1 that W_{sep} calculated using a 2x4x1 mesh differs from the one obtained using a 3x6x2 mesh by ~60 mJ/m^2, i.e., by approximately 0.6%. The 2x4x1 mesh is a computationally reasonable choice, since it requires almost 5 times less resources, than the 3x6x2 mesh. The accuracy using the 2x4x1 mesh is sufficient for a reliable distinction among the values of the work of separation, except the case of weakly-bound A_2-T_3. The latter, however, is not a problem as we are interested in the structures with the highest adhesion.

7.4.2 Wavefunction expansion

According to Bloch's theorem [76], solutions of the Schrödinger equation for a periodic system can be written in a form of an infinite series (plane-wave expansion)

$$\psi_{\boldsymbol{k}}(\boldsymbol{r}) = \sum_{\boldsymbol{G}} C_{\boldsymbol{k}+\boldsymbol{G}} e^{-i(\boldsymbol{k}+\boldsymbol{G})\cdot\boldsymbol{r}}, \tag{7.4}$$

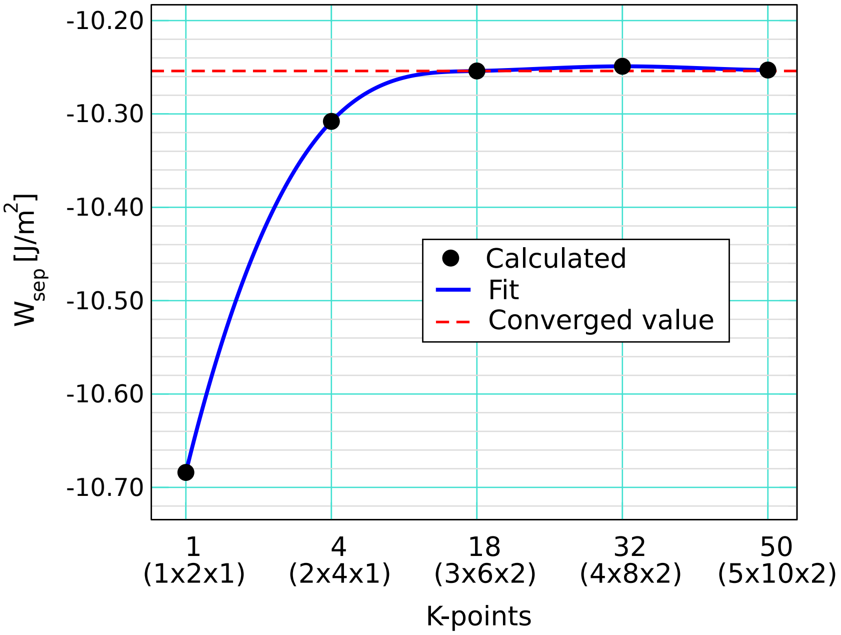

Figure 7.1: Convergence of the work of separation with respect to the number of k-points.

where $\boldsymbol{k}$ is a vector in the first Brillouin zone, and the vectors $\boldsymbol{G}$ belong to the reciprocal lattice. Each of the plane-waves in equation 7.4 corresponds to the kinetic energy

$$E = \frac{h^2}{2m_e}|\boldsymbol{k}+\boldsymbol{G}|^2.$$

It is reasonable to assume that the contributions with low-energy are physically the most important [107]. Thus, in practical calculations a cut-off energy is used to truncate this expansion from above

$$E_{\text{cut-off}} = \frac{h^2}{2m_e}G^2_{\max}, \tag{7.5}$$

$$\Rightarrow \quad G_{\max} = \sqrt{\frac{2m_e E_{\text{cut-off}}}{h^2}}. \tag{7.6}$$

After truncation equation 7.4 turns into

$$\psi_{\boldsymbol{k}}(\boldsymbol{r}) = \sum_{|\boldsymbol{k}+\boldsymbol{G}|\leq G_{\max}} C_{\boldsymbol{k}+\boldsymbol{G}} e^{-i(\boldsymbol{k}+\boldsymbol{G})\cdot\boldsymbol{r}}.$$

In order to study the convergence of the work of separation with respect to the cut-off energy, the superlattice used in Subsection 7.4.1 was employed. The convergence of W_{sep} with respect to the cut-off energy is shown in Fig. 7.2. It

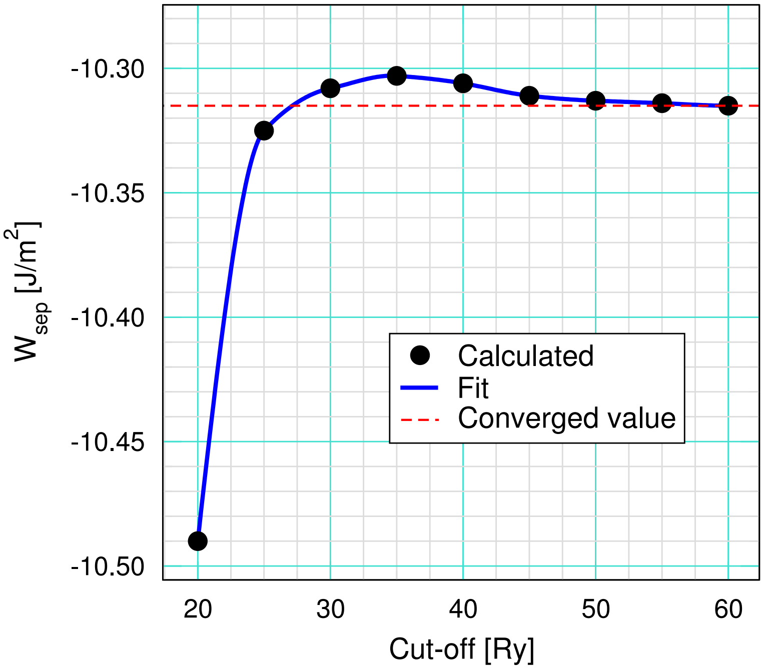

Figure 7.2: Convergence of the work of separation with respect to the cut-off energy.

is evident, that at a cut-off value of 25-30 Ry the work of separation is already converged, and its absolute error is about 10-20 mJ/m^2, i.e., approximately 0.1-0.2%. Such precision is beyond the one we need to compare reliably, however, taking into account the necessity to relax the structures, low cut-offs should be avoided to decrease the error of atomic forces. So, a cut-off energy of 30 Ry is a reasonable and computationally efficient choice.

7.4.3 Thickness of slabs

Since the interface structures are modeled using sapphire and rutile slabs stacked into multi-layers the question of sufficient slab thickness has to be investigated. On the one hand, the slabs have to be thick enough to exclude interactions between atoms from its opposite surfaces and other finite size effects. On the other hand, since computational demand increases rapidly with the number of atoms considered, it is practical to use the lowest possible slab thickness. An additional source of numerical errors of the work of separation are slight oscillations due to the inevitable inconsistency in basis sets, which originates from the difference of super-cell size in the direction normal to the interface. In this work the slab thickness is quantitatively described by the number of layers. The definition of the term *layer* for A_3-T_3 is the following. An N-layer slab of Al_2O_3 consists of N [-Al-O-Al-] triplets of atomic planes stacked into one sequence, and capped by Al atomic planes from each side. An N-layer slab of TiO_2 consists of N [-O-Ti-O-] tiplets of atomic planes stacked into one sequence, and capped by oxygen planes from each side. Formally, both of these slabs can be described by following formuli Al-[Al-O-Al]$_N$-Al and O-[O-Ti-O]$_N$-O, leading to $3N + 2$ atomic layers in each slab, where N is a natural number.

First, we investigate the static case, where the slabs are fixed before and after cleavage. The results are summarized in Table 7.2. The deviation from the converged value of 10.33 ± 0.01[J/m^2] is negligible ($< 0.4\%$) already at the minimal thickness.

Table 7.2: The *static* work of separation as a function of slab thickness. The number of *layers* in each slab is indicated by N^s(substrate) and N^o(over-layer). E stands for the total energy of the supercell (SL), the Al_2O_3 slab (AS), and the TiO_2 slab (TS).

N^s	N^o	E(SL)[Ry]	E(AS)[Ry]	E(TS)[Ry]	W_{sep}^{static} [J/m^2]
2	3	-2354.4279	-534.2583	-1816.3523	10.29
4	3	-2839.7196	-1019.5481	-1816.3522	10.29
4	5	-3924.6995	-1019.5478	-2901.3210	10.33
4	7	-5009.6632	-1019.5478	-3986.2915	10.31
6	3	-3325.0115	-1504.8403	-1816.3521	10.29
6	5	-4409.9914	-1504.8398	-2901.3209	10.32
6	7	-5494.9550	-1504.8395	-3986.2916	10.31
6	9	-6579.9346	-1504.8393	-5071.2645	10.33
8	9	-7065.2263	-1990.1308	-5071.2646	10.33

The next step is to consider atomic relaxation in the vicinity of the interface and, after cleavage, at the free surfaces. In the course of relaxation we allow the 4 outermost atomic layers from each side of a slab to be fully relaxed, whereas the central parts were kept fixed to emulate the bulk-like environment. The inter-slab separation was varied, allowing atoms to relax according to the methodology described above. The optimal separation, i.e., the one giving the lowest total energy, was selected for the evaluation of the work of separation. Table 7.3 presents the so obtained values. The most striking difference to the *static* case is the appearance of very pronounced oscillations, such that no apparent convergence trend could be identified for the considered thicknesses. To shed light on this phenomenon, we partition the change in work of separation due to relaxations into its components, and analyze them. For that, we, first, write the equation for the "quasi-static" work of separation, i.e., the work of separation for fixed atomic positions, but using the relaxed inter-slab distance:

$$2A \times \tilde{W}_{sep}^{stat} = \tilde{E}(AS)^{stat} + \tilde{E}(TS)^{stat} - \tilde{E}(SL)^{stat} \tag{7.7}$$

Then, the equation for the work of separation is:

$$2A \times W_{sep}^{rlx} = E(AS)^{rlx} + E(TS)^{rlx} - E(SL)^{rlx} \tag{7.8}$$

Table 7.3: The work of separation as a function of slab thickness. The number of *layers* in each slab is indicated by N^{s}(substrate) and N^{o}(over-layer). E stands for the total energy of the supercell (SL), the $\mathrm{Al_2O_3}$ slab (AS), and the $\mathrm{TiO_2}$ slab (TS).

N^{s}	N^{o}	E(SL)[Ry]	E(AS)[Ry]	E(TS)[Ry]	$W_{\mathrm{sep}}^{\mathrm{relax}}$ [J/m^2]
2	3	-2355.0468	-534.2858	-1817.3400	9.22
4	3	-2840.3234	-1019.5757	-1817.3946	9.04
4	5	-3925.2988	-1019.5753	-2902.4423	8.84
4	7	-5010.2691	-1019.5755	-3987.4151	8.84
6	3	-3325.6154	-1504.8676	-1817.3947	9.04
6	5	-4410.5909	-1504.8673	-2902.3731	9.03
6	7	-5495.5599	-1504.8668	-3987.2567	9.26
6	9	-6580.5346	-1504.8669	-5072.3209	9.02
8	9	-7065.8262	-1990.1587	-5072.2287	9.27

Subtraction of equation 7.7 from equation 7.8 gives the required decomposition:

$$\begin{aligned} E_{\mathrm{rlx}} = 2A \times (W_{\mathrm{sep}}^{\mathrm{rlx}} - \tilde{W}_{\mathrm{sep}}^{\mathrm{stat}}) = &\\ & \left[E(\mathrm{AS})^{\mathrm{rlx}} - \tilde{E}(\mathrm{AS})^{\mathrm{stat}}\right] + \\ & \left[E(\mathrm{TS})^{\mathrm{rlx}} - \tilde{E}(\mathrm{TS})^{\mathrm{stat}}\right] - \\ & \left[E(\mathrm{SL})^{\mathrm{rlx}} - \tilde{E}(\mathrm{SL})^{\mathrm{stat}}\right] = \\ & \Delta E(\mathrm{AS}) + \Delta E(\mathrm{TS}) - \Delta E(\mathrm{SL}) \end{aligned}$$

Here, ΔE(AS), ΔE(TS), and ΔE(SL) are the relaxation energies of the sapphire slab, rutile slab, and superlattice, respectively. Their numerical values are compiled in Table 7.4. The contributions from the α-$\mathrm{Al_2O_3}$ slabs are very similar to each other starting from 2 layers. The relaxation energies reveal a minor extent of reconstructions. In turn, there are discrepancies in the relaxation energies of $\mathrm{TiO_2}$ ($\sim$ 0.1 Ry), and they reproduce an oscillation pattern of the work of separation (see Fig. 7.3). Therefore, we conclude that the relaxation of rutile slabs is the main source of the deviations. The energy of relaxation is much higher compared to the sapphire surface, which is a sign of massive reconstructions. It is also interesting to notice that the relaxation energies can be divided into 3 groups: approximately, -1.12, -1.05, and -0.97 Ry per unit cell. This gives rise to the following hypothesis: the oscillations in the relaxation energy are, probably, due to the existence of local minima on the potential energy surface (PES), so that sometimes the system is being trapped, leading to higher total energies and, consequently, to higher works of separation.

To verify the hypothesis, we address the geometries with the relaxed surface atoms presented in Fig. 7.4. An analysis allows for dividing them into three

Table 7.4: The relaxation energies as a function of slab thickness. The number of layers in each slab is indicated by N^{s}(substrate) and N^{o}(over-layer). The symbol A stands for the interface area. The energies are given in Rydberg units.

N^{s}	N^{o}	$-\Delta E(\mathrm{SL})$	$\Delta E(\mathrm{AS})$	$\Delta E(\mathrm{TS})$	E_{rlx}
2	3	0.636	-0.028	-0.988	-0.380
4	3	0.611	-0.028	-1.043	-0.460
4	5	0.606	-0.027	-1.122	-0.543
4	7	0.613	-0.028	-1.124	-0.539
6	3	0.611	-0.028	-1.043	-0.459
6	5	0.606	-0.027	-1.052	-0.474
6	7	0.612	-0.027	-0.967	-0.382
6	9	0.606	-0.027	-1.057	-0.479
8	9	0.606	-0.027	-0.966	-0.387

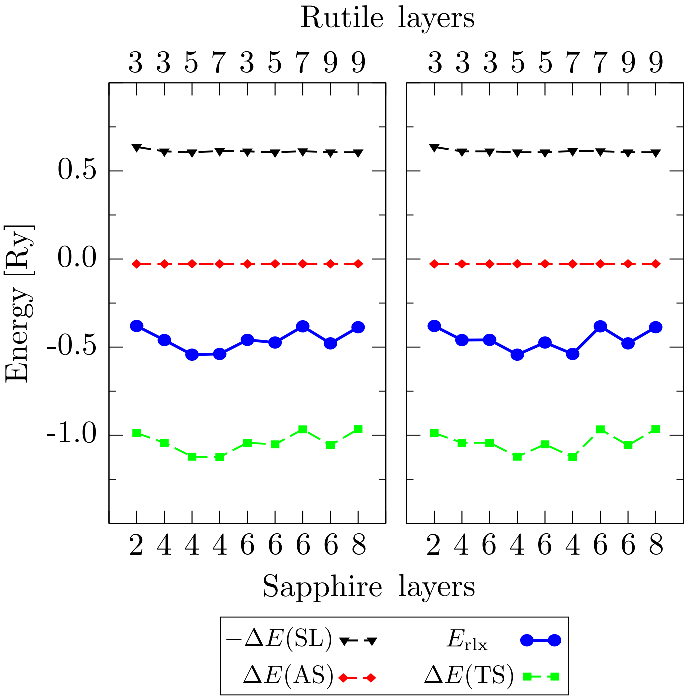

Figure 7.3: The relaxation energy (blue, circles) and its components: surface relaxation of sapphire slab (red, diamonds), rutile slab surface relaxation (green, squares), and interface relaxation (black, triangles) as a function of sapphire and rutile slab thicknesses. The data is ordered by ascending thickness of the sapphire (left) or rutile (right) slab, respectively. Reproduced from [73].

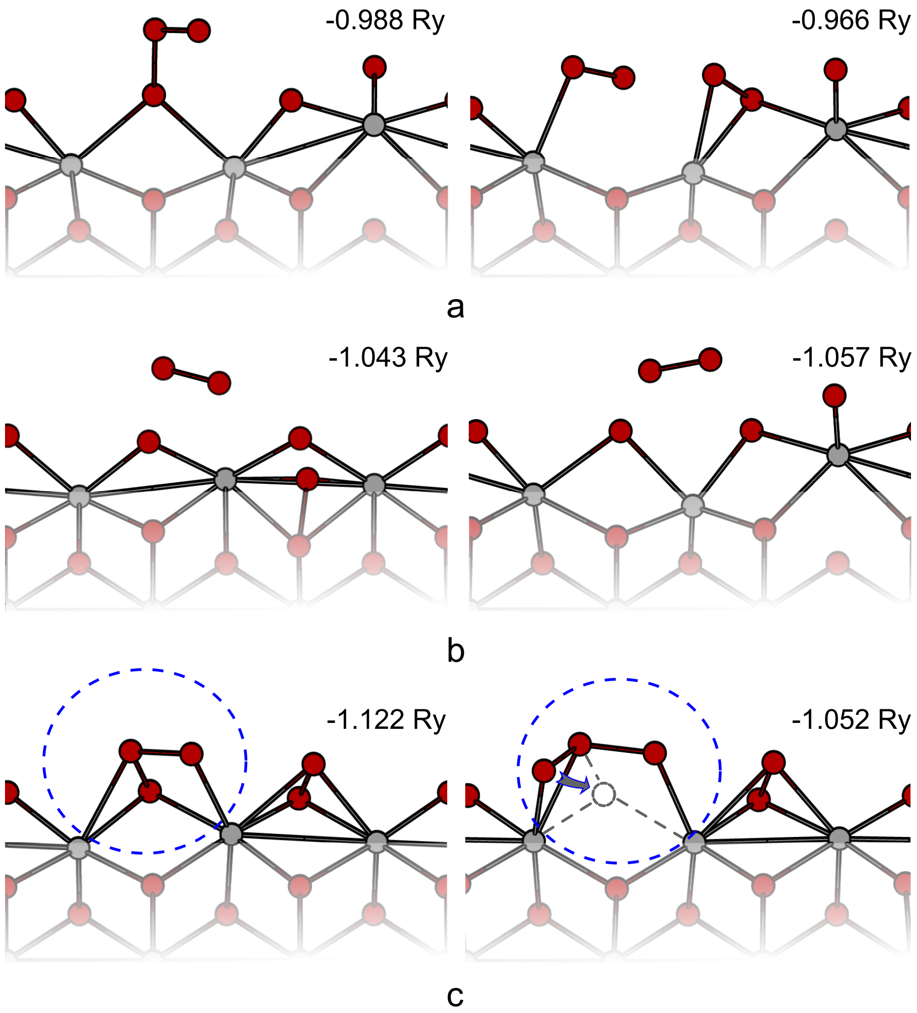

Figure 7.4: Surface geometries of relaxed double-oxygen terminated (T3) rutile: a) "Dangling oxygen" type, represented by the final pattern for 2L-3L (left), 6L-7L, and 8L-9L (right); b) "desorbed oxygen" type, consisting of 4L-3L (left), 6L-3L, and 6L-9L (right); c) "O_3-bridge" type, exhibited by the systems 4L-5L and 4L-7L (left), and 6L-5L (right). 6L-5L has a somewhat smaller relaxation energy, which is actually close to the one of the "desorbed oxygen" type. Structurally, this energetic difference originates from the different position of one of the oxygen atoms at the surface (see encircled areas). It can be matched to the position in the left structure by moving the atom along the arrow indicated in the figure. Reproduced from [73].

distinct groups. The first one, a "dangling oxygen" pattern, leads to the smallest relaxation effects, and is discovered for 2L-3L (2 *layers* of sapphire, 3 *layers* of rutile), 6L-7L, and 8L-9L. The second pattern, which we name "desorbed oxygen" type, gives rise to intermediate relaxation energies, and is found for 4L-3L, 6L-3L, and 6L-9L. An "O_3-bridge" pattern is encountered for 4L-5L, 4L-7L, and 6L-5L. While 4L-5L and 4L-7L exhibit the lowest relaxation energy and exactly the same geometry, the 6L-5L system has a relaxation energy closer to the one of the "desorbed oxygen" group. Yet, its geometry is much closer to "O_3-bridge" type, except one oxygen atom (see the encircled area). Being moved as it is depicted in Fig. 7.4a, this oxygen atom would allow to match the optimal surface geometry. Manual correction of the 6L-5L structure with subsequent relaxation leads to exactly the same geometry and energy as for the 4L-5L and 4L-7L. Motivated by this finding, we tried to apply the same correction to the other thicknesses by manually imposing the "O_3-bridge" surface geometry as a starting point. And, indeed, this led to significantly larger relaxation energies and, thus, to a great improvement of the convergence, as shown in Fig. 7.5. This way, it was confirmed that the 5-layer T_3 slab is thick enough to obtain the relaxed work of separation, converged to about 10-20 mJ/m^2. At the same time, the presence of local minima becomes evident, and therefore more robust methods capable of avoiding local minima would be preferable.

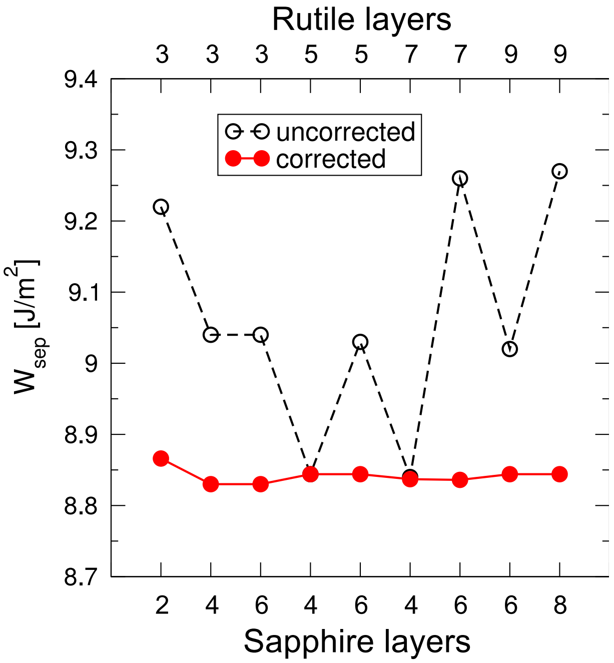

Figure 7.5: The improvement of the work of separation convergence with respect to slab thickness, when the manual correction is applied (see the text). Reproduced from [73].

7.5 Conclusions

In this chapter, the work of separation for all considered atomic stacking variants were presented (see Table 7.1). It turned out, that the stacking sequence A_2-T_2, that was found to be the most compact structure in the previous chapter, has, at the same time, the highest work of separation (9.31 J/m^2). Next to it there is the A_3-T_3 structure (8.84 J/m^2), that also has an oxygen-metal-oxygen stacking, but a somewhat lower coordinaton at the interface. The metal-to-metal stacked A_3-T_2 superlattice has a significantly smaller work of separation (1.58 J/m^2) as compared to the former two. And the least bound superlattice (0.45 J/m^2) is the one with the A_2-T_3 stacking (oxygen-to-oxygen).

A thorough convergence testing was performed for one of the stacking sequences (A_3-T_3) with respect to the Brillouin zone sampling, wavefunction expansion cut-off, and slab thickness. These tests allowed to define the computational parameters, that, on the one hand, give reasonable precision, and, on the other hand, do not make the calculations excessively or even prohibitively demanding.

Chapter 8

Electronic structure

8.1 Introduction

Properties of materials are tightly connected to their electronic structure. Thus, in this chapter the electronic structure of the considered interfaces is presented. The chapter is organized in the following way. First, an analysis of the plane-averaged charge (PAC) distributions is presented for all considered interface structures. The connection between integral charge transfer (ICT) and work of separation (W_{sep}) is revealed and discussed. Second, densities of states (DOS) of the valence electrons are analyzed with emphasis on the comparison among the considered interface structures. Further, each total DOS is decomposed into the corresponding partial densities of states (PDOS), and the the role of the major contributions is studied. After this brief comparison of all considered interface structures, the the most prominent structure, i.e., A_2-T_2, is analyzed in detail. First, the local densities of electronic states (LDOS) are shown. Among many interface-induced features, the presence of an interface-induced electronic state is discovered and visualized. In the next section, the findings ot the Löwdin-charge analysis are presented. Further, we shortly discuss the issues of modeling TiO_2 using LDA and GGA, and how they can affect the results presented in this work. At the end, conclusions for the whole chapter are drawn.

8.2 Plane-averaged charge

In Fig. 8.1 we provide the plane-averaged charge (PAC) of A_2-T_2, A_2-T_3, A_3-T_2, and A_3-T_3. The PAC characterizes the spatial distribution of electronic charge and its rearrangement upon interface formation along some direction. As we are primarily interested in the charge distribution across the interface and in its vicinity, we choose the direction along the normal to the interface plane (c, in

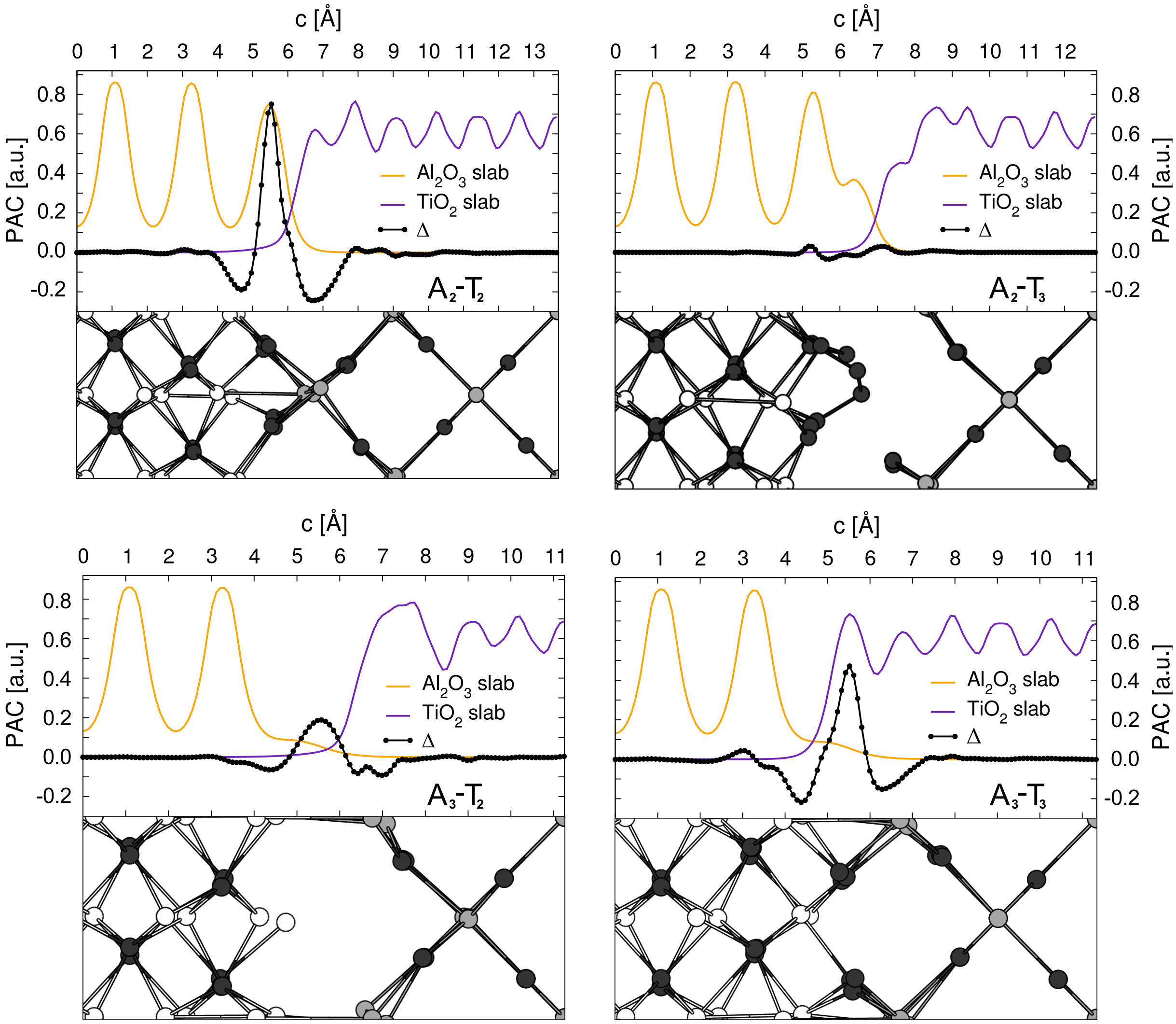

Figure 8.1: Plane-averaged charge (PAC) of the relaxed structures. Δ stands for the difference between the PAC of the super-lattice and the sum of PACS of the individual aluminum oxide and titanium oxide slabs. The values of Δ are scaled by the same factor across all panels. Each graph is supplemented with the structure of one half of the super-lattice supercell (the second half is identical due to inversion symmetry), where Al, Ti, and O atoms are represented by the white, gray, and dark gray solid circles, respectively. Reproduced from [73].

the geometric setup used here). We calculate PACs of the whole sandwich-like supercell, and of its constituents (individual slabs), obtained after the removal of one or the other part. Each slab has free surfaces, and their presence results in a perturbation of the electronic density close to the surface. This effect with no doubt affects the PAC, and, especially, the difference (Δ) between the PAC of the whole structure and the sum of PACs of the constituents, leading to artificial features. Therefore, Δ's have to be considered with care. Looking at the PAC of the relaxed A_2-T_2 structure, we note the first glaring feature of the charge distribution across the interface – its strong inhomogeneity in the aluminum oxide slab as compared to the titanium oxide slab. Another prominent feature is a quite significant charge rearrangement (Δ–curve) in the ~6 Å thick region around the interface. The charge distribution of the whole structure of the relaxed A_2-T_3 structure is almost a superposition of charge distributions of the individual slabs. Due to weak interface bonding, the PAC difference is much smaller as compared to A_2-T_2, overall, the region affected by the interface is also approximately 6 Å in thickness. Far from the interface, the metal-to-metal stacked A_3-T_2 structure demonstrates a charge distribution close to previously considered structures. The charge rearrangement at the interface is moderate, and happens mostly in a ~7 Å thick region around the interface. The spatial charge distribution in the A_3-T_3 structure is quite similar to the one of A_2-T_2. While the PAC difference also resembles the pattern of the A_2-T_2 structure, its amplitude is smaller. The main feature is a charge accumulation in the oxygen layer sandwiched between an aluminum layer from one side and a titanium layer from the other.

To summarize, the PACs of the considered structures reveal a different extent of charge rearrangement, depending on the stacking. The modification of the electronic density mostly happens in a 6-7 Å thick region in the vicinity of the interface. The bonding strength at the interface measured by the work of separation is clearly correlated with the amplitude of the difference in PACs. This correlation becomes even more obvious, when the work of separation is plotted as a function of integral charge transfer (ICT) (Fig. 8.2). The latter is obtained

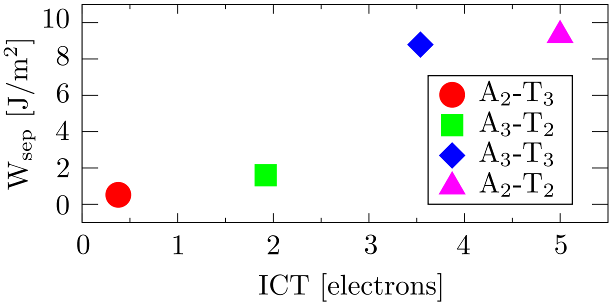

Figure 8.2: Work of separation as a function of integral charge transfer.

by integrating the absolute value of the PACs difference along the c-axis over the unit-cell. ICT is an indirect measure of the local charge transfer due to bonding. The clearly non-stoichiometric interfaces A_2-T_3 and A_3-T_2 show rather small charge transfer, and their work of separation is below 2 J/m^2. In contrast, the more stoichiometric systems A_2-T_2 and A_3-T_3 exhibit a significantly larger charge transfer, and works of separation of about 9 J/m^2.

8.3 Density of states

Here, we calculate the total density of states (DOS), and analyze the contributions of particular kinds of atoms. The result is shown in Fig. 8.3. Only the major PDOS contributions are depicted. The Fermi level of the metallic interface (A_3-T_2) is set to zero. In case of the insulating interfaces the Fermi level is set to the bottom of the conduction bands. The valence band is mainly composed of O 2*p* states with an admixture of Ti 3*d* states for all considered interfaces. The

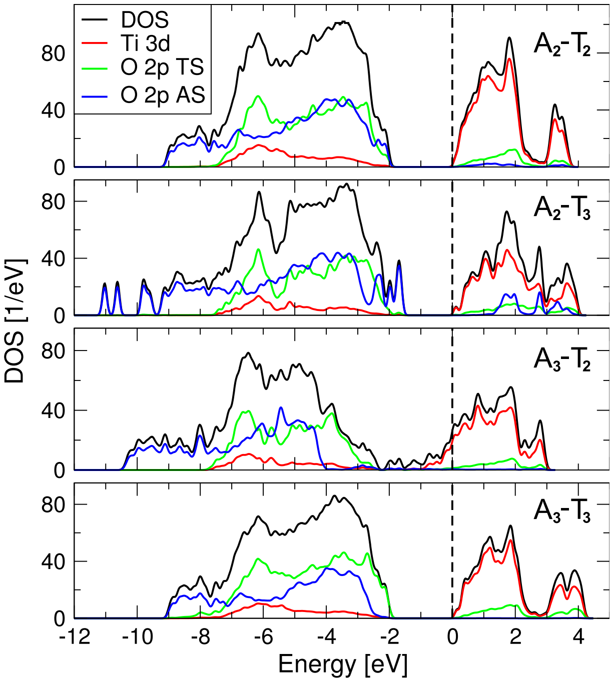

Figure 8.3: Total electronic density of states (DOS) plots, supplemented with the major contributions of the projected densities of states (PDOS). The oxygen contributions originating from the aluminum oxide slab (AS, blue lines) and the titanium oxide slabs (TS, green lines) are provided separately. The contributions from the Ti 3*d* states are shown as red lines. The dashed line indicates the Fermi level. Reproduced from [73].

conduction bands are dominated by Ti 3*d* states. The DOS of the structurally similar interfaces A_2-T_2 and A_3-T_3 are, naturally, very close to each other, both exhibiting a 1.9-2.0 eV Kohn-Sham band gap. Poor coordination of oxygen atoms at the interface region in A_2-T_3 leads to the appearance of defect-like states above the top of the valence band (around -1.9 eV), which decreases the Kohn-Sham band gap to 1.6-1.7 eV. An even more drastic change of the electronic structure happens when there is a metal-to-metal stacking at the interface, i.e., for A_3-T_2, leading to a complete closure of the gap.

The local densities of states (LDOSs) of the A_2-T_2 are presented in Fig. 8.4. Several features become evident, when going across the interface, indicative of the changes in the bonding character. First of all, the LDOS of oxygen-layers changes from the characteristic of Al_2O_3 to TiO_2 type, when going from bottom to top in Fig. 8.4. The O 2*p* peaks in TiO_2 at 0-2 eV and 3-4 eV decay in Al_2O_3. The shape of the Ti 3*d* peak at -8 to -2 eV smoothens, when approaching the IF. The sharp peak at -5.6 eV is not so pronounced in the Ti-layer next to the IF. The same smoothing happens to the Al 3*p* states. In contrast, a distinquished peak of Al 3*s* appears in the LDOS of the Al-layer next to the IF. Another feature is the appearance of rather sharp peaks at -2.5 to -2.0 eV (the top of the valence zone) in the LDOS of the oxygen-layer situated right at the IF and the Ti-layer nearby. These peaks are consistent with the presence of a localized interface electronic state. Visualizing the contribution of the Kohn-Sham states located in the energy window from -2.5 to -1.5 eV (Fig. 8.5), the presence of an interface state becomes evident. One can see that the interface state has the dumbbell shape typical for *p* states, and that it is more strongly pronounced for the interfacial oxygen atoms closer to Al.

8.4 Löwdin charges

Although there is no unique method to assign charges to atoms incorporated in molecules or solids, partitioning schemes provide useful information. Löwdin charge analysis [108] is one of the methods, along with the Mulliken scheme [109], the Bader approach [110], and many others, to assign charges to atoms in molecules or solids. It gives a semi-quantitative description of charge-distribution-sensitive properties in many systems, and performs, generally, better than Mulliken analysis [111]. Our purpose is to see how the occupancy of atomic-like orbitals change as a function of distance from the interface. It has to be stressed, that we are mainly interested in the development of the Löwdin charges across the interface, rather than in their absolute values.

The layer-averaged values of Löwdin charges on atoms and their orbital decomposition are shown in Fig. 8.6. The total Löwdin charges of Ti (Q_t(Ti)) show that titanium atoms lose in average about 1.6 electrons/atom as compared to

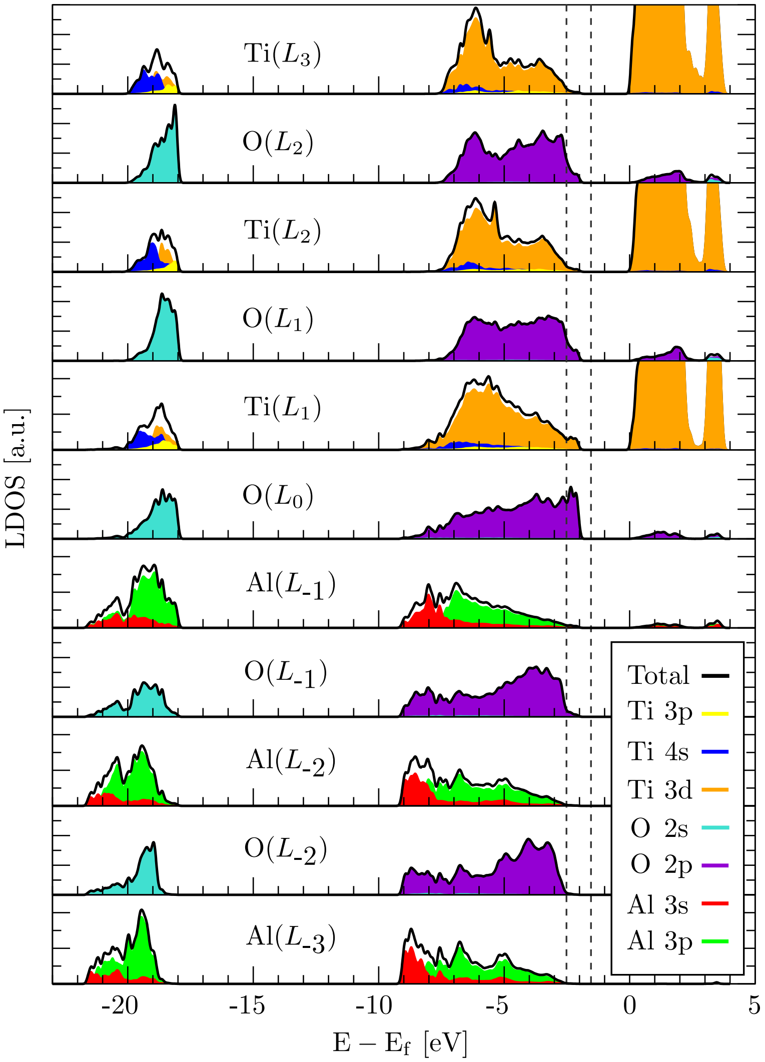

Figure 8.4: Local densities of states for the A_2-T_2 interface. Each panel corresponds to one kind of atoms in a specific layer specified as L_i, where the index i counts the layers from the interface. Dashed lines indicate the top of the valence band. Reproduced from [73].

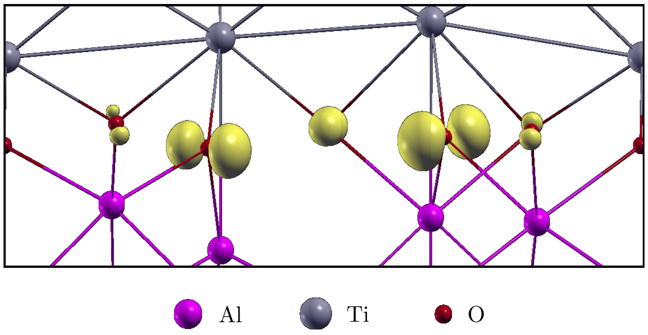

Figure 8.5: A detail of the A_2-T_2 structure containing the interface. The interface electronic state is shown as yellow isosurface. Reproduced from [73].

the isolated atom ($3s^23p^64s^23d^2$ with 12 valence electrons in total). Ti atoms residing next to the interface lose a bit more electrons than the bulk-like atoms. In contrast, the Ti atoms in the second layer from the IF attain less charge as compared to bulk-like layers. The orbital decomposition of Q_t(Ti) shows that the $3p$-states remain almost untouched, and thus are not shown in Fig. 8.6. The main changes upon interface formation happen in the s- and d-states with the trends opposite to each other. The net-population of the s-orbitals ($3s+4s$) decreases by 0.04 electrons/atom, whereas that of the d-orbitals rises by 0.03 electrons/atom, approaching the IF. The major charge loss happens in the s-states, most likely in the $4s$.

The total charge on Al atoms is 1.20-1.24 electrons/atom lower than in the isolated configuration ($3s^23p^1$, 3 valence electrons). When approaching the interface, Al atoms gain about 0.04 electrons/atom, and most of it goes to the $3p$-orbitals.

The charge on the oxygen atoms, as represented by Q_t(O), is 0.74-0.76 electrons/atom higher than in the atomic configuration ($2s^22p^4$ with 6 valence electrons), with slightly higher values in the Al_2O_3 part. A slight decrease of 0.02 electrons/atom occurs in the interfacial layer and in the first oxygen layer of TiO_2. It is, probably, connected to the increase of charges of Ti d-states and Al p-states in the vicinity of the IF. There are similarities and differences in occupancies of the s- and p-states of oxygen in the TiO_2 and Al_2O_3 parts. In both oxides the s-states are depopulated, and the p-states are overpopulated as compared to the reference of an isolated O atom. Hovewer, the charge deficiency of the $2s$-orbitals of O deep in TiO_2 is 0.20 electrons/atoms, whereas in bulk-like Al_2O_3 it is 0.20 electrons/atom higher, i.e., 0.40 electrons/atom. A completely opposite trend is seen in the case of the p-orbitals, so in TiO_2 the charge gain is 0.95 electrons/atom, while in Al_2O_3 it is 1.15 electrons/atom, i.e. 0.20 electrons/atom higher than in titanium dioxide. As for the O atoms situated right at the interface, the occupancies of their s- and the p-states show a mixed character, which appears to be a superposition of the respective states of pure oxides.

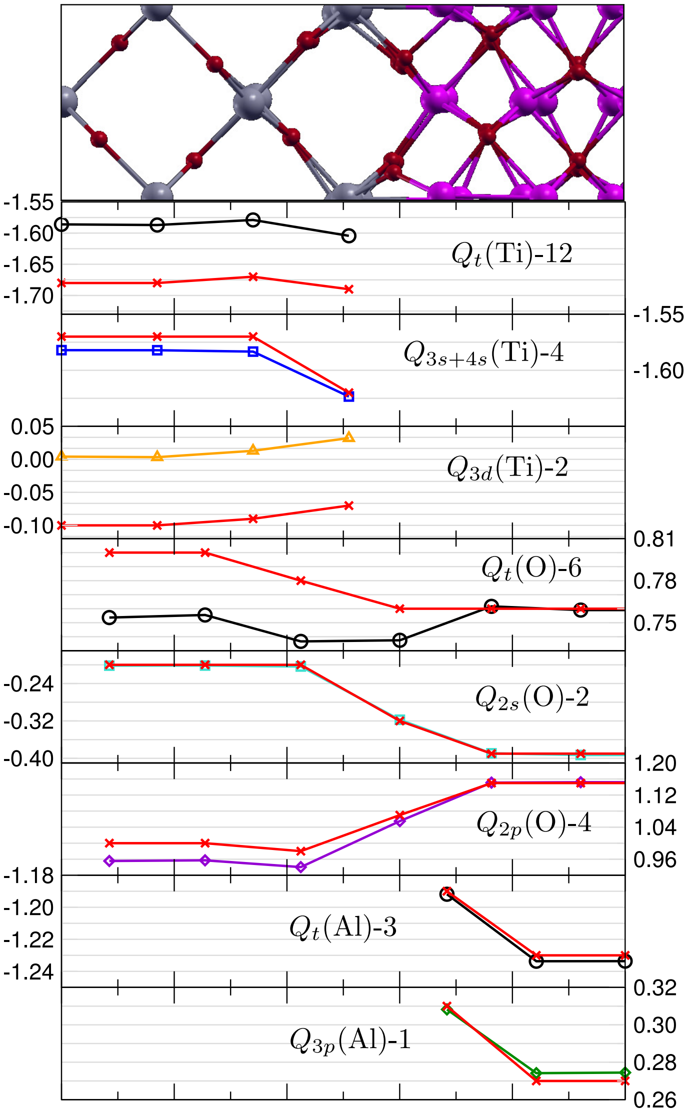

Figure 8.6: Layer-averaged Löwdin charges (Q) of A_2-T_2. Subscript "t" corresponds to the total charge. Red lines represent the charges obtained within the DFT+U framework (U(Ti)=3.25eV). Only the orbital contributions whose change across the interface is >0.01 electrons/atom, are shown.

8.5 The effect of Hubbard U

It is known that conventional exchange-correlation functionals like LDA or GGA cannot correctly reproduce the electronic structure of titanium dioxide due to self-interaction errors, especially when defects or surfaces are studied. One of the ways to cope with this problem is to mimic stronger correlations through the DFT+U [112–117] method. The purpose of this section is to examine briefly how DFT+U affects the electronic structure of A_2-T_2. Here, we use the simplified rotationally invariand flavor of DFT+U implemented in the Quantum ESPRESSO code, and described elsewhere [118].

The choice of an appropriate value for U is a delicate matter. Usually, a set of calculations with different values of U is performed, and the U which leads to the best agreement to experiment is selected. Arroyo-de Dompablo et al. [119] using $U \approx 5$ eV find good agreement between their theoretical studies and experimental data on geometry, electronic structure, and relative phase stability of titanium dioxide polymorphs at equilibrium and under high pressure. A more consistent approach is proposed by Cococcioni and de Gironcoli [118], where the authors introduce a method, which relies upon evaluation of the Hubbard U via a linear response approach. When it comes to the study of defects and surfaces of TiO_2, a variety of values of U can be found in literature, ranging from 2.5 eV to 4.2 eV [120–122].

For systems like A_2-T_2, in principle, different values of U should be used for Ti atoms, as the value of U may change across the interface. Here, however, we adopt the same value of $U=3.25$ eV from [121] for all Ti atoms in the cell, for the purpose of an estimation of the effect.

The effect of Hubbard U on the density of electronic states is presented in Fig. 8.7. The shapes of both, valence and conduction zones, are slightly changed; in particular, the the conduction band width decreases. The Kohn-Sham band-gap increases from 2.24 eV to 2.50 eV, i.e., by 0.26 eV. The peak in Ti 3*d* around -5 eV gets slightly more pronounced.

The influence of Hubbard U on the Löwdin charges is shown in Fig. 8.6. The total charge on Ti atoms decreases by 0.09 electrons/atom, which is almost completely due to depopulation of *d*-states, while there are just minor changes on Al atoms.

The total charge of oxygen in TiO_2 increases by 0.04-0.05 electrons/atom and, thus, the oxygen charge in TiO_2 becomes larger than in Al_2O_3, which is opposite to the uncorrected results. Most of this gain in charge leads to an increase in population of the *p*-states, while the *s*-states stay almost unchanged.

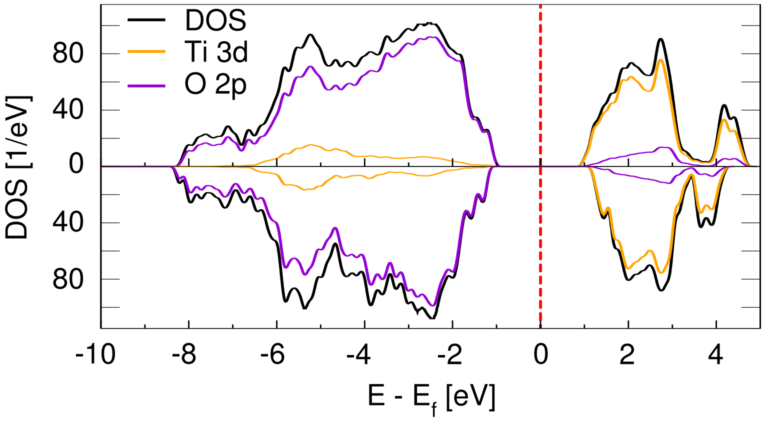

Figure 8.7: Total densities of electronic states (DOS) with U=0 eV (top panel), and with U=3.25 eV (bottom panel). The main contributions from partial densities of states (PDOS) are also provided. The Fermi level is set in the middle of Kohn-Sham gap, and marked with a red dashed line.

8.6 Conclusions

The spatial charge distribution and its rearrangement due to the presence of the interface were analyzed evaluating the plane-averaged charge distribution (PAC). It was found that most of the charge relocation happens in a 6-7 Å thick region around the interface. The most profound charge rearrangement was observed in the superlattices with the strongest adhesion, i.e., in A_2-T_2 and A_3-T_3, whereas the weakly bound interfaces A_2-T_3 and A_3-T_2 exhibited significantly smaller rearrangements. That way, a correlation was found between the integrated charge transfer and the values of the work of separation.

The electronic structure of the superlattices was studied using total and partial DOS. It was found that the valence bands of all superlattices are formed mostly by O 2*p* and Ti 3*d* states, whereas the main contribution to the conduction band has Ti 3*d* character. The obtained values of the Kohn-Sham band gaps are 1.9-2.0 eV for A_2-T_2 and A_3-T_3, and 1.6-1.7 eV for A_2-T_3. The A_3-T_2 structure turned out to be metallic.

The LDOS of A_2-T_2 revealed the evolution of the electronic structure across the interface. The most notable feature of A_2-T_2 is the presence of a localized interface state.

In order to see how the interface affects the orbital populations, the electronic density was decomposed by means of a Löwdin charge analysis. It was found for the Ti atoms, that the population of the *s*-orbitals slightly decreases, when approaching the interface, whereas the population of the *d*-states becomes a little bit higher. The *p*-states of Ti remain almost untouched. The Al *p*-orbitals become a bit more populated close to interface. The oxygen charges are different in each slab. The population of the 2*s*-orbitals in the TiO_2 part of the superlattice is higher, than in the the Al_2O_3 one; whereas, the trend is opposite for the 2*p*-states. In the vicinity of interface, the charges are of mixed character, corresponding to an average of the populations found for each oxide.

A short test was performed in order to see the effect the DFT+U method on the electronic structure of A_2-T_2, represented by the DOS and the orbital populations. The value of U (3.25 eV) used for the calculation is taken from literature [121]. Is was found that the inclusion of Hubbard U slightly changed the shape of the DOS. The value of the Kohn-Sham band gap increases by 0.26 eV, and became 2.50 eV. The orbital populations also altered a bit. The *d*-orbitals of the Ti atoms become depopulated by about 0.09 electrons/atom. A gain in population was detected for O *p*-orbitals in the TiO_2 part of the superlattice. The occupation of the Al-orbitals were hardly affected. Overall, the changes of the electronic structure are minor, applying the DFT+U to the A_2-T_2 structure. This assures us that the results, we have presented in the previous chapters, would not change significantly, if we recalculate them in the DFT+U framework.

Chapter 9

Mechanical moduli

9.1 Introduction

In this chapter, the mechanical moduli of the A_2-T_2 superlattice are examined. To this end, the structure which was used to study the work of separation and electronic properties, is further relaxed allowing the complete cell-shape, i.e., the lattice parameters a, b, and c, and angles α, β, and γ, to change too. To remind, so far the in-plane lattice parameters and angles were fixed to the values obtained from the stress balancing, whereas the supercell was allowed to relax along the direction normal to the interface. Here, however, the full cell-shape relaxation is allowed. This relaxation leads to minor changes of the supercell parameters (not more than 1%), which demostrates the usefulness of the stress balancing method. After that, the bulk modulus, the Young's modulus along the [001]-axis, and the shear modulus of a (001)-plane shear distortion along the [010]-axis are calculated and compared to the effective elastic moduli, obtained from the elastic constants of the individual bulk oxides. Particular attention is devoted to the technical details of the calculations, such as data fitting and convergence analysis. The chapter ends with concluding remarks.

9.2 Effective elastic constants of the superlattice

The idea of getting *effective* elastic properties [40, 41] of complex materials, like superlattices, from the elastic properties of the bulk constituents looks very fascinating. One of the methods proposed for calculating effective elastic constants of superlattices is the method of Grimsditch and Nizzoli (GN) [40, 41]. This method was mostly applied to metallic superlattices [123–127], hovewer, there is also some work on semiconducting materials [128, 129]. In some cases [124, 128, 129] the

GN-approach gives results close to experimental findings, obtained by measuring sound velocities in superlattices. In other cases, the method fails to reproduce the experimental data – most notable examples are systems, where the so-called *supermodulus* effect [123, 125, 130] or *shear softening* [127] are observed. Naturally, the failures of the method of Grimsditch and Nizzoli happen, when the assumptions made in the formulation of the method are not fulfilled by a system. For instance, the method does not take into account any effects of coherency strain, nor possible phenomena connected to the presence of interfaces in superlattices. The intent of this chapter is to test the applicability of the GN-method to the A_2-T_2 interface system.

The ingredients we need to calculate the estimate of the elastic matrix of A_2-T_2 via the Grimsditch-Nizzoli approach are the elastic matrices of bulk Al_2O_3 and TiO_2 given in the same cartesian system as for the superlattice, and the ratio between the thicknesses of the constituent slabs. Taking into account that the elastic matrix of unstrained Al_2O_3 is

$$\mathrm{C(Al_2O_3)} = \begin{bmatrix} 462 & 144 & 104 & -20 & 0 & 0 \\ 144 & 462 & 104 & 20 & 0 & 0 \\ 104 & 104 & 466 & 0 & 0 & 0 \\ -20 & 20 & 0 & 137 & 0 & 0 \\ 0 & 0 & 0 & 0 & 137 & -20 \\ 0 & 0 & 0 & 0 & -20 & 159 \end{bmatrix}, \tag{9.1}$$

the elastic matrix of unstrained TiO_2 is

$$\mathrm{C(TiO_2)} = \begin{bmatrix} 474 & 148 & 148 & 0 & 0 & 0 \\ 148 & 259 & 170 & 0 & 0 & 0 \\ 148 & 170 & 259 & 0 & 0 & 0 \\ 0 & 0 & 0 & 213 & 0 & 0 \\ 0 & 0 & 0 & 0 & 115 & 0 \\ 0 & 0 & 0 & 0 & 0 & 115 \end{bmatrix}, \tag{9.2}$$

and the thickness ratio is

$$\frac{\mathrm{d(Al_2O_3)}}{\mathrm{dTiO_2}} \approx \frac{2}{3},$$

the estimate for the effective elastic matrix of the superlattice is

$$\mathrm{C_{GN}(SL)} = \begin{bmatrix} 467 & 145 & 136 & -10 & 0 & 0 \\ 145 & 336 & 152 & 10 & 0 & 0 \\ 136 & 152 & 314 & 0 & 0 & 0 \\ -10 & 10 & 0 & 174 & 0 & 0 \\ 0 & 0 & 0 & 0 & 122 & -7 \\ 0 & 0 & 0 & 0 & -7 & 131 \end{bmatrix}. \tag{9.3}$$

This matrix will be used in order to estimate the effective elastic moduli in the following sections.

9.3 Polynomial fitting procedure

The common way of obtaining elastic constansts or moduli consists of imposing a certain strain on a crystal, and looking, then, at the crystal's response, i.e., the change of energy, pressure, or stress. As an outcome of such a procedure we get a set of "strain-response" couples. It is important to note, that both the strain and the response are prone to computational errors. The strain is defined with respect to the best guess of the equilibrium parameters, whereas the true equilibrium is almost never reached. The response of a crystal is also calculated with finite precision. The property of interest for us is the value of the first derivative of the strain-response curve at equilibrium. One of the ways to obtain this derivative is to use numerical differentiation; another approach is to fit the *ab initio* data with an analytical function, and find its derivative analytically. Here, we use the second method, which is, more specifically, the fitting of polynomials to data by means of the least-squares method.

For each of the considered moduli, i.e., the bulk modulus, Young's modulus along [001] (normal to the interface), and the shear modulus of (001) along [010], 20 datapoints are obtained on evenly spaced meshes. These points are partitioned into 10 ranges, so that each range consists of an even number of points centered around the equilibrium. For instance, $range_1$ contains two points around equilibrium, i.e., one point from each side, $range_2$ comprises four points, and so on, as illustrated in Fig 9.1. For the points in each range a series of fits using polynomi-

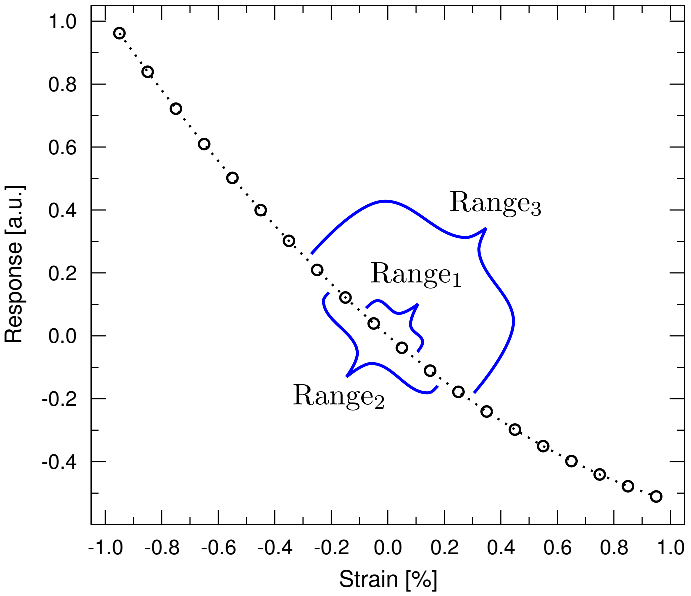

Figure 9.1: Dummy strain-response curve showing the hierarchy of ranges used for polynomial fitting.

als with degrees from 1 to N-1 is performed, where N is the number of points in the range. The so obtained polynomials allow to identify their exact equilibrium parameters, i.e., roots, and analytical first derivatives. This approach is close in spirit to the one described in [131]. It has to be noted here, that the procedure described above favors lower degrees of polynomials in a sense that they are used for fitting more times, than the higher degree polynomials. Ultimately, this fact can be illustrated by the following example: the polynomial of the first degree (a straight line) is used here for fitting in all 10 ranges, i.e., 10 times, whereas the polynomial of the nineteenth degree is used just once – in $range_{10}$, that includes all 20 datapoints.

Assume, we obtained the values of the first derivatives from fits. To get these numbers, we used different ranges (subsets) of the initial data and different degrees of fitting polynomials. It can happen that some values are quite far from the "true" value due to a number of reasons. For instance, if we try to fit a straight line to a dataset whose character is essentially non-linear, and then use its slope as an estimate for the slope of the curve correctly describing the dataset, we risk to introduce huge errors. Yet another source of inaccuracies is the problem of *overfitting*, which is neatly illustrated by a phrase attributed to John von Neumann:*"With four parameters I can fit an elephant, and with five I can make him wiggle his trunk"*. To treat both of these deficiencies, a regularization-like technique is applied. That is, some additional requirements concerning the range of the allowed values of the first derivative are introduced, so that all the values out of the range are, simply, disregarded.

After applying the regularization conditions, we still have a scatter of values of the first derivative. The questions arise: Which of the values is "the best", i.e., converged, and what is the error bar? To answer these questions, a visual inspection or cross-validation [132, 133] can be used as it is done in [134]. However, here we study the distribution of values by calculating histograms and analyzing them. When dealing with histograms, it is important to choose the optimal number of bins, which is connected to resolution and precision. On the one hand, we want to get the most precise results, and therefore would tend to use as many bins as possible. On the other hand, the use of too many bins will ultimately lead to isolating individual datapoints, and, thus, will not allow us to locate the regions of their congestion.

To summarize, the procedure of fitting used in the next sections consists of the following steps:

1. Perform a polynomial fit of the *ab initio* dataset using ranges.
2. Discard the values, that do not fulfill the regularization conditions.
3. Use histograms to analyze the values which passed the previous step.

9.4 Bulk modulus

The bulk modulus describes the elastic response of a material to hydrostatic stress as depicted in Fig. 9.2. It can be calculated from the volume-pressure relationship via the formula

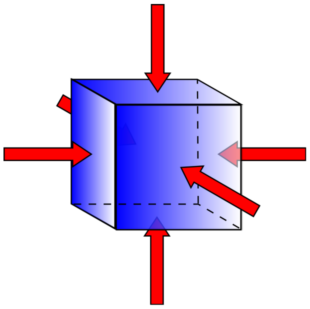

Figure 9.2: An illustration of hydrostatic stress acting on a cube.

$$B_0 = -V_0 \cdot \frac{dP}{dV}(V_0) = \frac{1}{k}, \tag{9.4}$$

where V_0 is the equilibrium volume, P is the pressure, and k is the compressibility. For single crystals, the latter can be written as

$$k = s_{11} + s_{22} + s_{33} + 2(s_{12} + s_{13} + s_{23}), \tag{9.5}$$

where s_{ij} are the components of the compliance matrix.

Once the equilibrium volume V_0 and bulk modulus B_0 are known, Eq. 9.4 can be rewritten in a convenient form:

$$P = B_0 \cdot (1 - V/V_0)\,. \tag{9.6}$$

9.4.1 Computational procedure

The volume-pressure curve is calculated using the variable cell-shape optimization by Wentzcovitch [135], which simulates hydrostatic stress. In fact, it is the target pressure which is pursued in the process of relaxation. Once this pre-defined pressure is achieved, the corresponding volume is known. This way, a dataset of V-P pairs is obtained. The V-P dataset obtained for A_2-T_2 is shown in Fig. 9.3.

9.4.2 Fitting the *ab initio* dataset

The fitting is performed according to the procedure described in 9.3. The workflow related, specifically, to the bulk modulus is as follows:

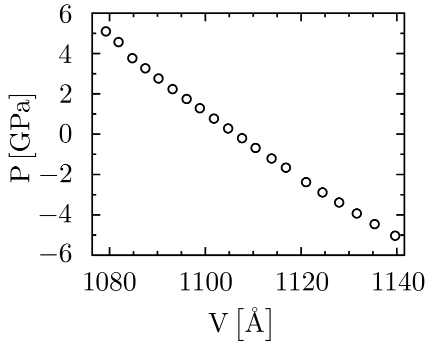

Figure 9.3: Volume-pressure dependency calculated for A_2-T_2.

- First, tha dataset $\{V_i, p_i\}$ is fitted by polynomials using the sequence of ranges as described in 9.3.

- We know the following about the superlattice used to obtain the *ab initio* dataset. On the one hand, the superlattice is unlikely in the true equilibrium, hovewer, it must be very close to the true equilibrium as the superlattice is relaxed. Therefore, for every fitting polynomial the roots (V_0's) are identified. Then, those roots, which are closest to the "equilibrium volume" are selected as the true equilibrium. More specifically, the roots must satisfy $V_0 \in [1103; 1109]$ Å^3. This region is estimated using the result of cell-shape relaxation, 1107.7 Å^3.

- Then, the analytical derivatives of the fitting polynomials are evaluated at the corresponding true equilibrium volumes, i.e., at V_0's, and the values of B_0 are calculated. After that, the B_0's are sifted, so that only those B_0's are left, that fulfill the condition $B_0 \in [150; 250]$ GPa. The range of allowed values of the bulk modulus of the superlattice is estimated from the value of the effective bulk modulus obtained by the GN-approach. The GN-estimate of the bulk modulus is 216 GPa, so the the selected range is 200±25% GPa, i.e., $[150; 250]$ GPa.

As an outcome of the fitting we get a set of $\{V_0, B_0\}$ as shown in Fig. 9.4. Convergence analysis using histograms gives a value of 1106.45 Å^3 for the (*true*) equilibrium volume (V_0), and a value of 183 GPa for B_0. Both of these values are indicated by red dashed lines in Fig. 9.4.

The dependence of B_0 on the degree of the fitting polynomial is given in Fig. 9.5. It is evident that for this particular case most of the polynomials of degree higher than 8 fail to give B_0 within the allowed range (in the framework describeGoled above). It can also be seen, that for smaller ranges of deformations the polynomials of lower degree give the best result, whereas for large deformations higher

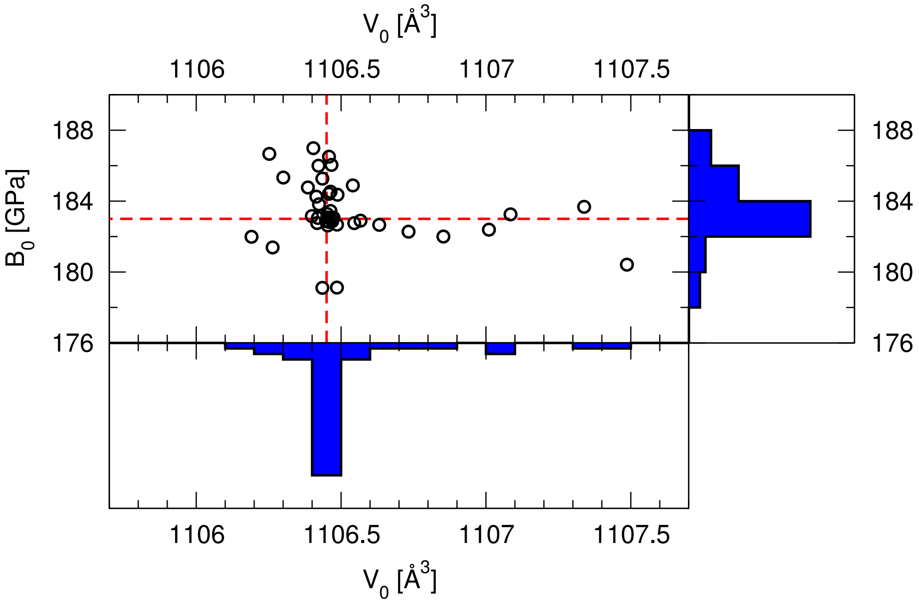

Figure 9.4: Scatter plot of $\{V_0, B_0\}$ points obtained after fitting. The resolutions of V_0- and B_0-histograms are 0.1 Å^3 and 2 GPa, respectively.

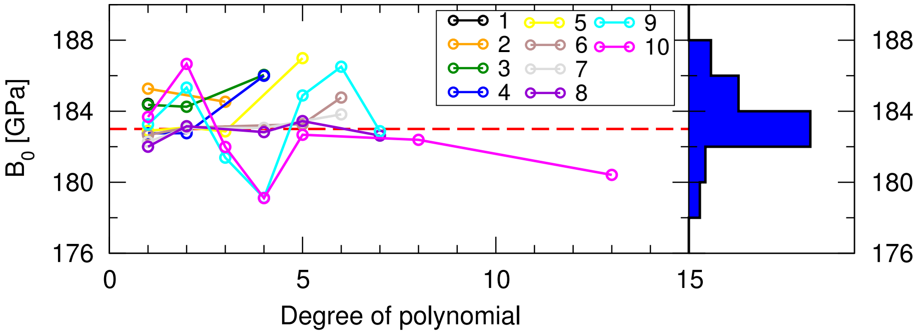

Figure 9.5: Dependence of B_0 on the degree of the fitting polynomial (left), and histogram showing the distribution of B_0 (right). Each curve corresponds to one fitting region; indices of regions are coded by color as shown in the legend.

degree polynomials are required to obtain the converged value of B_0, which is consistent with [134].

9.4.3 Results and analysis

The result of fitting and convergence analysis is shown in Fig. 9.6. The converged value of V_0 is very close (the deviation is less than 0.1%) to the initial equilibrium volume of the A_2-T_2 superlattice (the volume obtained after relaxation). According to the histogram at the right-hand side in Fig. 9.4, the value of B_0 has a spread of about ±5 GPa around the highest peak, thus giving an upper estimate of the error. Therefore, the final estimate of B_0 is 183±5 GPa. Comparing this number to the prediction of the Grimsdich-Nizzoli method (216 GPa), we can see that there is a discrepancy of about 15-20%, and that the GN-approach overestimates the bulk modulus of A_2-T_2.

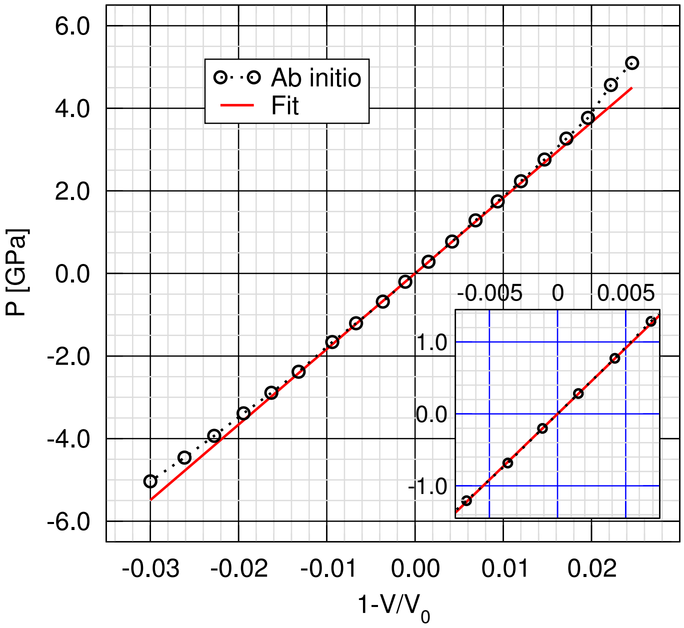

Figure 9.6: The result of fitting V-P *ab initio* data. The inset shows the region around zero with higher magnification.

9.5 Young's modulus

Young's modulus describes the mechanical response of a material to tensile load (stress) as shown in Fig. 9.7. It is defined as the strain-stress dependence by the

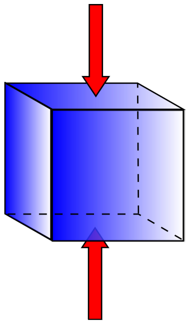

Figure 9.7: An illustration of tensile stress acting on a cube.

formula

$$E = \frac{\sigma_t}{\epsilon_t}, \tag{9.7}$$

where ϵ_t is the tensile strain, σ_t is the tensile stress. For single-crystals we have

$$E = \frac{1}{\tilde{s}}, \tag{9.8}$$

where $\tilde{s}$ is the compliance of the crystal along the direction of the applied stress.

9.5.1 Computational procedure

In order to get the value of E_0 along the direction perpendicular to the plane of the interface, i.e., along [001], the following method is used. A series of tensile deformations of the equilibrium structure of A_2-T_2 along the z-axis is made (the z-axis is almost indistiguishable from the [001] axis), then a constrained relaxation of the cell-shape and an ionic relaxation of the deformed superlattice is performed, allowing the cell to relax only in the xy-plane. The result of this procedure is shown in Fig. 9.8. It can be seen in the bottom panel, that the σ_{11} and the σ_{22} curves have a jaggy character, which is likely due to numerical noise. The clear depencence of the shear components on the amount of strain is the result of a slight misalignment of the supercell's Bravais vectors with respect to the cartesian frame due to finite precision of the cell-shape relaxation.

9.5.2 Fitting the *ab initio* dataset

The fitting is performed according to the procedure described in 9.3. The workflow related, specifically, to the Young's modulus is as follows:

- First, the *ab initio* dataset consisting of $\{\varepsilon_i,\ \sigma_{33}(\varepsilon_i)\}$ couples is used for polynomial fitting using ranges as prescribed in 9.3.

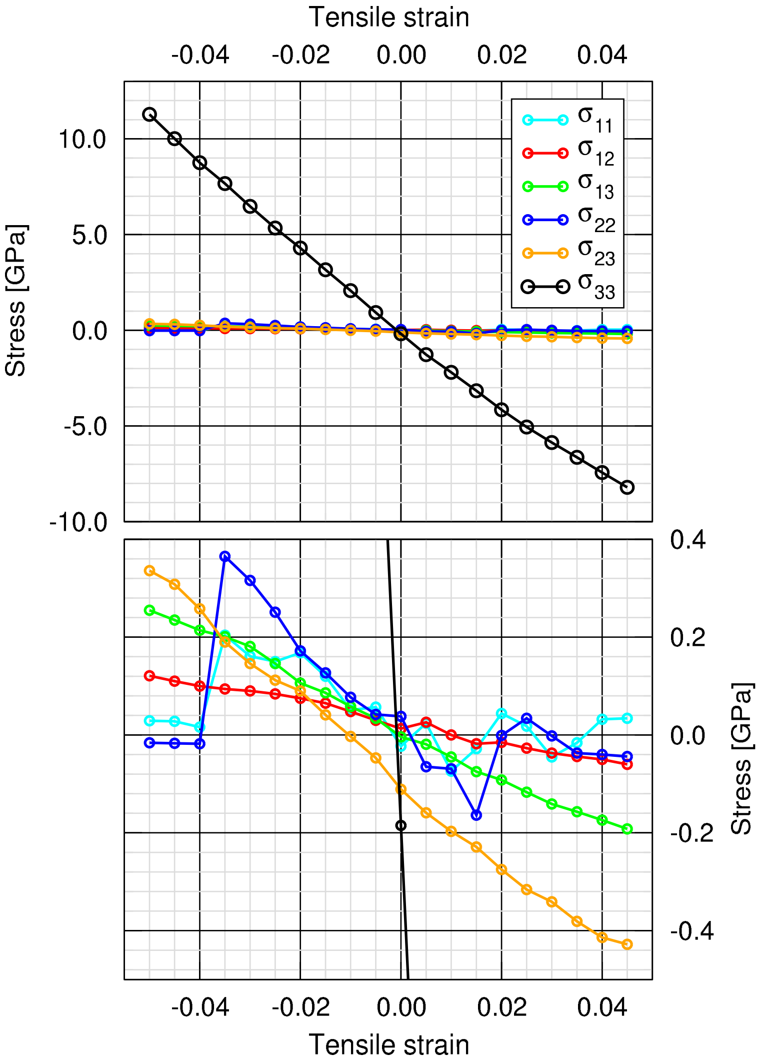

Figure 9.8: Stress-components as functions of tensile strain. The bottom panel is a magnification of the top one.

- Then for each fitting polynomial the roots are looked for in the region of [-0.0025;0.0025] (defined by visual inspection).
- Next, the E_0 is calculated for the found root, and checked if it complies with the allowance range of [160;300] GPa. The range is again defined with the help of the GN-estimate. According to the method, the Young's modulus of A_2-T_2 along the [001] axis is 234 GPa. Thus, a range of allowed values of 230±30% GPa is selected, that contains the GN-estimate inside.

The output of this procedure is shown in Fig. 9.9. The converged values of the strain-correction (ε_0) is -0.00075. Young's modulus along [001] (E_0) is found to be 217.5 GPa. The converged values of ε_0 and E_0 are shown in Fig. 9.9 as red dashed lines. The tail-like group of points at the right side of the central congestion of the points is formed by linear fits of the ranges with high index. The dependence of E_0 on the degree of the fitting polynomial is given in Fig. 9.10. Unlike the case of the bulk modulus, here all degrees of polynomials give reasonable results, however, higher degrees of polynomials and, thus (remember the procedure, described in 9.3), larger amplitudes of strain tend to give higher values of E_0.

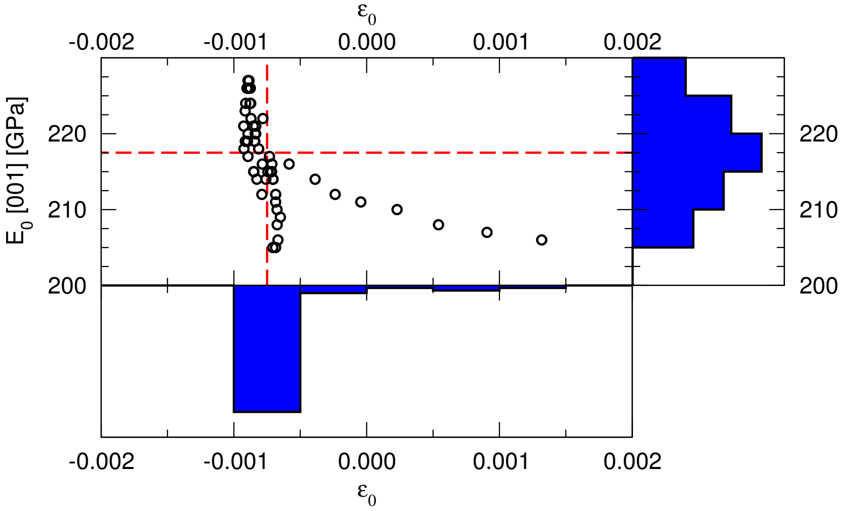

Figure 9.9: Scatter plot of $\{\varepsilon_0, E_0\}$ data obtained by fitting. The resolutions of ε_0- and E_0-histograms are 0.0005 and 5 GPa, respectively.

9.5.3 Results and analysis

The result of fitting and convergence analysis is shown in Fig. 9.11. The behavior of the superlattice in the range of the considered distortions is asymmetric. Upon

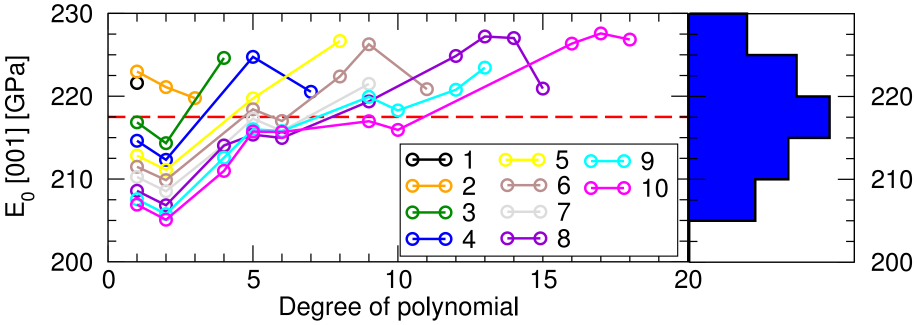

Figure 9.10: Dependence of the Young's modulus on the degree of a fitting polynomial (left), and the distribution histogram of $E_0[001]$ (right). Each curve corresponds to one fitting region; indices of regions are coded by color as shown in the legend.

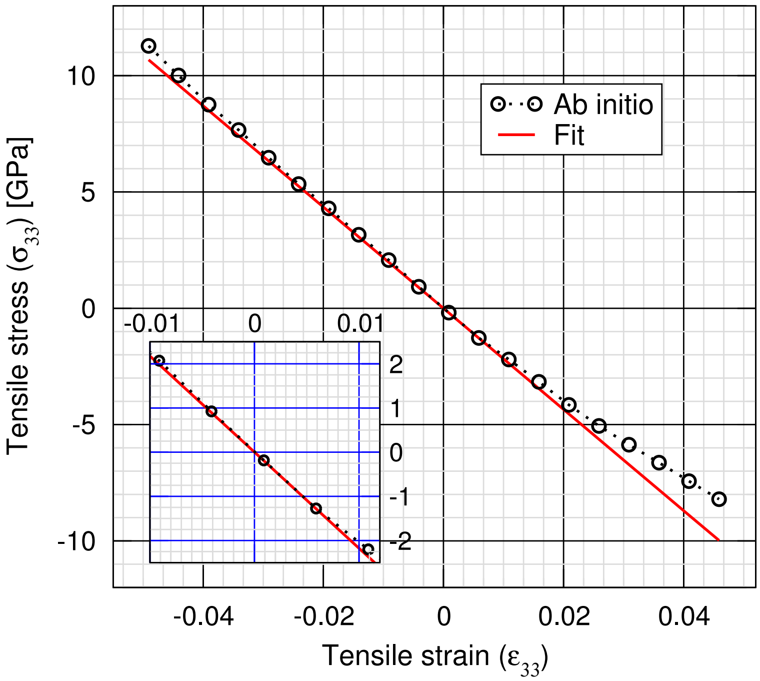

Figure 9.11: Results of fitting the *ab initio* data. The inset shows the region around zero with higher magnification.

compressive uniaxial strain the superlattice responds almost linearly up to the maximal distortion of ≈5%. In contrast, upon tensile strain the response of A_2-T_2 starts to deviate considerably from a linear law at ≈2-3%.

According to the histogram on the right panel in Fig. 9.10, there is a spread of ±12.5 GPa around the center of the main peak (E_0=217.5 GPa), thus the upper estimate of the error is ±12.5 GPa. This leads us to an estimate of the Young's modulus of A_2-T_2 along [001] of $E_0 = 217.5\pm12.5$ GPa. Compared to the GN-estimate of 234 GPa, it shows that again, the Grimsditch-Nizzoli method overestimates the value of the mechanical modulus. Though, the relative error in this case is marginally lower than the one for the bulk modulus, it is of the order of 2 to 14%.

9.6 Shear modulus

The shear modulus describes the mechanical response of a material to shear strain, as depicted in Fig. 9.12. It is defined as

$$G = \frac{\sigma_s}{\epsilon_s}, \tag{9.9}$$

where ϵ_s is the shear strain, and σ_s is the shear stress. For single-crystals G can be calculated as

$$G = \frac{1}{\tilde{s}}, \tag{9.10}$$

where $\tilde{s}$ is the corresponding shear compliance of the crystal.

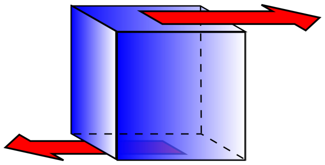

Figure 9.12: An illustration of shear stress acting on a cube.

9.6.1 Computational procedure

To obtain one specific shear modulus, namely, the one, which corresponds to the shear of the (001) plane along [010], a series of shear deformations of the A_2-T_2 supercell is performed. After deformation, atoms within the cell are relaxed, and at the same time the shape of the cell is allowed to relax along all the cartesian axes, i.e., x, y, and z. The result of this procedure is shown in Fig. 9.13. It can be seen in the bottom panel, that the σ_{11}, the σ_{22}, and the σ_{33} curves have a jaggy character, which is likely due to numerical noise. The reason why σ_{12} and σ_{13} are not equal to zero is the same as given in 9.5.1.

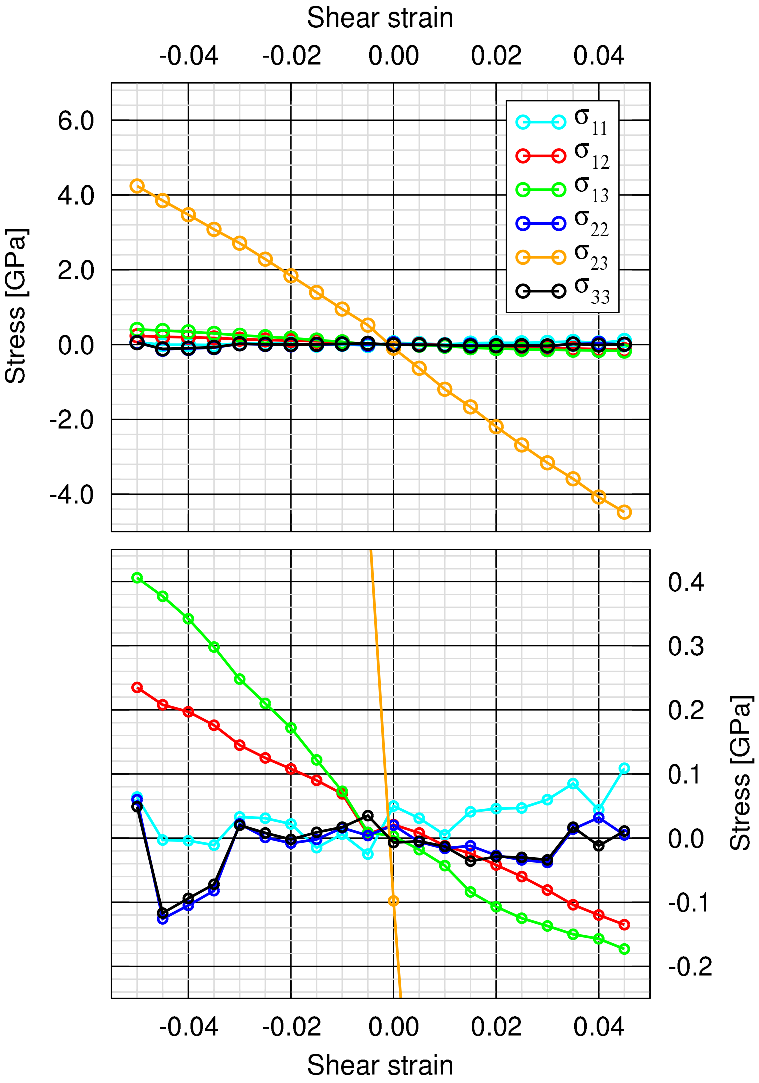

Figure 9.13: Stress-components as functions of shear strain. The bottom panel is a magnification of the top one.

9.6.2 Fitting the *ab initio* dataset

The fitting procedure is performed according to the procedure described in 9.3. The workflow related, specifically, to the shear modulus is done in the same way as for Young's modulus in 9.5.2, and described below:

- First, the *ab initio* dataset consisting of $\{\varepsilon_i,\ \sigma_{23}(\varepsilon_i)\}$ couples is used for polynomial fitting using ranges as prescribed in 9.3.
- Then for each fitting polynomial, the root in the region of [-0.0025;0.0025] (defined upon visual inspection) is looked for.
- Next, G_0 is calculated for the found root, and checked if it complies with the allowance range. The range is again defined with the help of the GN-estimate, however, in a trickier way. According to the method, the shear modulus of A_2-T_2 is 173 GPa. So, at first, a range of values of 170±30% GPa, i.e, [120;220] GPa was selected. It turned out, from the distribution of the obtained values of G_0, however, that they are only few and they are all concentrated at the lower boundary of the allowed range. Therefore, the range of allowed values of G_0 was adjusted, taking also into account the overestimation of the bulk and the Young's moduli by the GN-approach, described in 9.4 and 9.5, respectively. So, a new range of [70;170] GPa centered at about 120 GPa was selected, i.e., the allowed range was shifted down to account for the overestimation.

The outcome of the fitting is presented in Fig. 9.14. The converged value of the strain-correction (ε_0) is -0.00075. The distribution of the values of G_0 has a bimodal character with two centers of congestion at 107.5 GPa and 117.5 GPa,

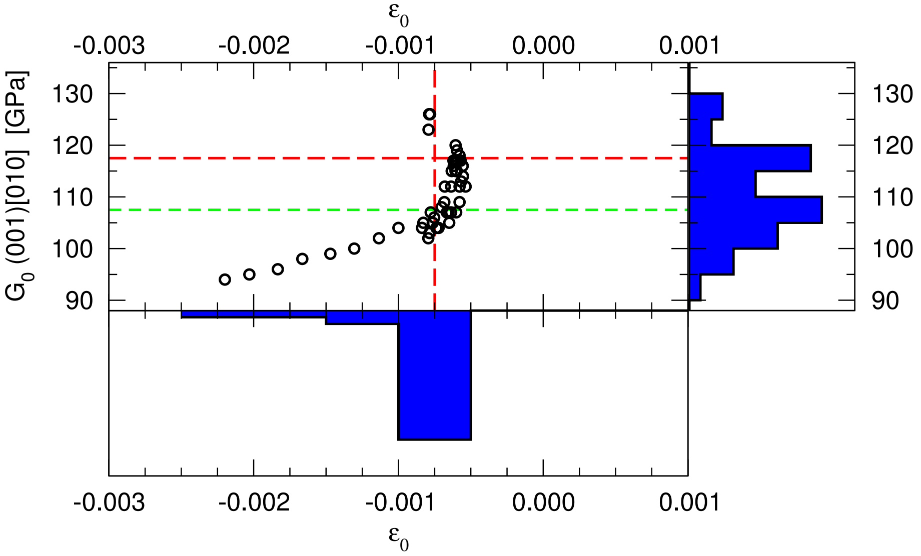

Figure 9.14: Scatter plot of $\{\varepsilon_0, G_0\}$ data obtained by fitting. The resolution of the ε_0- and G_0-histogram is 0.0005 and 5 GPa, respectively. Horizontal dashed lines indicate the two main peaks in the G_0-histogram, at 107.5 GPa (green) and at 117.5 GPa (red).

which are indicated by green and red horizontal dashed lines in Fig. 9.14, respectively. The tail-like structure on the left is formed by linear fits, as in the case of the Young's modulus.

The dependence of the shear modulus on the degree of the fitting polynomial is shown in Fig. 9.15. Similar to the case of the Young's modulus, higher degrees of polynomials, in average, result in higher values of the modulus.

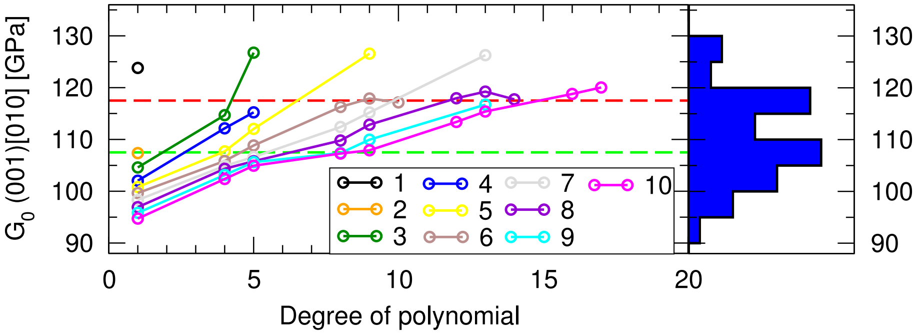

Figure 9.15: Dependence of G_0 on the degree of the fitting polynomial (left), and the distribution histogram of G_0(001)[010] (right). Each curve corresponds to one fitting region; indices of regions are coded by color as shown in the legend. Horizontal dashed lines indicate the two main peaks in the G_0-histogram, at 107.5 GPa (green) and at 117.5 GPa (red).

9.6.3 Results and analysis

The result of fitting is shown in Fig. 9.16. It is evident that the superlattice responds asymmetrically in the considered range of strains. The superlattice softens, i.e., declines from linearity quite early under shear strain. Therefore, in order to obtain a higher precision of the shear modulus a narrower range of strains should be used.

Due to the bimodality of the G_0-histogram, two possible values of G_0 are found, namely, 107.5 GPa and 117.5 GPa. One can see in Fig. 9.16 that G_0=107.5 GPa gives the best overall description of the *ab initio* data, whereas G_0=117.5 GPa seems to better reproduce the slope of the strain-stress curve at zero. Therefore, the value of 117.5 GPa is selected as the value of G_0. The uppermost estimate of the error is defined from the spread around the peak of 117.5 GPa. Disregarding the clearly pathologic tail-like group of points, we get a spread of ±17 GPa. So, the final estimate of the shear modulus of A_2-T_2 (G_0(001)[010]) is equal to 117.5±17 GPa. The discrepancy to the estimate from Grismditch-Nizzoli's method is of the order of 34 to 63%. Again, here the stiffness of A_2-T_2 calculated from *ab initio* data is lower than the one obtained using the GN-method.

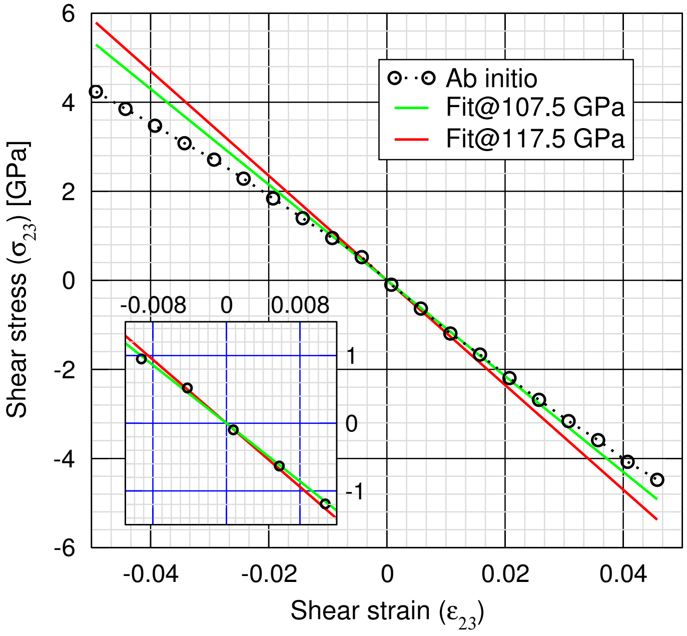

Figure 9.16: Results of fitting the *ab initio* data. The inset shows the region around zero with higher magnification.

9.7 Conclusions

The purpose of this chapter was to calculate selected mechanical moduli of the A_2-T_2 superlattice and to examine the applicability of the Grimsditch-Nizzoli approach.

A polynomial fitting procedure was used to fit the *ab initio* data. In order to study the reliability of the calculated numbers and to estimate computational errors, a convergence analysis based on histograms was introduced.

The converged value of the bulk modulus obtained in this work is 183±5 GPa. This value is 15-20% lower than the effective modulus. A rather small range of distortions allowed to achieve good precision.

The value of Young's modulus along the [001]-axis (normal to the interface plane) is 217.5±12.5 GPa, which is rather close to the GN-estimate (the relative error is 2-14%). The behavior of the superlattice in the range of considered distortions is asymmetric. Upon compressive uniaxial strain the superlattice responds almost linearly up to the maximal distortion of $\approx$5%, while, upon tensile strain the response of A_2-T_2 starts to deviate considerably from a linear law at $\approx$2-3%.

The estimate of the shear modulus corresponding to a shear deformation of the (001)-plane along the [010]-axis is 117±17 GPa. The deviation of the GN-estimate is the largest among the calculated moduli (the error is 34-63%). The superlattice

Table 9.1: Comparison of elastic moduli of the A_2-T_2 superlattice calculated *ab initio*, and through Grimsditch-Nizzoli estimate. Deviation is defined as $(M_{\mathrm{GN}} - M)/M$, where M_{GN} is a modulus by GN-approach, and M is *ab initio* one.

Quantity [GPa]	Al_2O_3 bulk	TiO_2 bulk	Superlattice		Deviation [%]
			GN-estimate	*Ab initio*	
B_0	232	203	216	183±5	15-20
E[001]	430	141	234	217.5±12.5	2-14
G(001)[010]	134	213	173	117.5±17	34-63

softens, i.e., declines from linearity quite early under shear strain. The softening occurs most noticeably for negative strain. In order to obtain a higher precision of the shear modulus, a narrower range of strains should be used.

The obtained data is compiled in Table 9.1. For convenience, the values of the corresponding moduli of bulk Al_2O_3 and TiO_2, as calculated from the elastic matrices 9.1 and 9.2, are given too. The GN-moduli are calculated from the elastic matrix 9.3.

In conclusion, it is evident that the approach of Grimsditch and Nizzoli overestimates the moduli of the considered superlattice and cannot substitute the direct evaluation using *ab initio* methods.

What to do in order to ensure reliable results? First of all, the range of distortions must be chosen with care in order to avoid the simultaneous presence of regions with significantly different behavior. Second, one has to calculate as many datapoints as possible to reduce the influence of numerical noise. And, finally, increasing the precision of the calculated stress or energy at each data point decreases the numerical noise itself.

Chapter 10

Summary and conclusions

In this thesis, the results of the first *ab initio* investigation of the $TiO_2(100) \,||\, (0001)$ Al_2O_3 interface were presented. The present study relies upon the experimental data for a real thin film of TiO_2 deposited on (0001) sapphire, that was produced and analyzed in the group of Prof. Mitterer [69, 70]. The above mentioned thin film has been used as a prototype system with well-defined parameters. In particular, the phase composition of the film (rutile), and the epitaxial relationships served as a starting point to create a model of the interface. Possible arrangements of atoms at the interface have been identified in this work by means of an atomic-stacking analysis.

In order to cope with lattice misfit between the substrate and the overlayer, we introduced the *stress balancing method.* The stress balancing method allows to minimize the total strain energy of a superlattice using linear elasticity theory in the most general, i.e., tensorial form.

The local arrangement of atoms in the vicinity of the interface was obtained by atomic relaxation. The structural features of the optimized geometries were analyzed by means of radial- and angular-distribution functions.

A range of properties was calculated for a series of superlattices, differing in their atomic stacking at the interface:

First, values for the work of separation were obtained, which allowed to identify a structure-adhesion relationship for the considered interfaces. It was established, that the maximal adhesion strength is achieved, when the metal-oxygen-metal stacking sequence, that is intrinsic for TiO_2 along [100] and for Al_2O_3 along [001], is preserved across the interface.

Second, diverse electronic properties were calculated, including the spatial charge distribution, and the total, partial, and local densities of electronic states. A variety of phenomena was discovered in the studied superlattices. For instance, it was found that the metal-to-metal stacked superlattice has no Kohn-Sham gap, whereas bulk TiO_2 and Al_2O_3 have wide KS band gaps. It was shown, that the superlattices with bulk-like atomic stacking preserve the KS band gap. Hovewer, for the structure with the highest adhesion a localized interface-induced electronic state was found. A connection between the interfacial adhesion strength and the integral spatial relocation of the charge density caused by the formation of the interface was found.

The last group of properties, evaluated for the superlattice with the highest adhesion, consists of various elastic moduli. The set of moduli comprises the bulk modulus (B), Young's modulus (E[001]), and the shear modulus (G(001)[010]). The numerical values of these moduli were esmimated using the effective elastic constans within the framework of the Grimsditch-Nizzoli method. The GN-esmitates were cross-checked by direct *ab initio* evaluation. It was revealed for the investigated superlattice, that the GN-approach based on the effective elastic moduli can lead to the errors as big as 70%. The latter accentuates the importance of *ab initio* methods.

The present work also established the foundation for further investigations of TiO_2-Al_2O_3 interfaces. One of the directions of such a work could be the experimental verification of the predicted atomic geometry by the high-resolution TEM analysis. The electronic structure of the superlattice can be further studied by, for instance, careful testing the effects of the Hubbard U correction, which was just touched in this work. And, of course, the stress balancing method introduced in the thesis requires more testing, and can potentially serve to provide a good starting point for modelling systems with moderate lattice misfit.

Appendix A

Elastic constants and crystal symmetry

A.1 General remark

Considering the mechanical stability and thermodynamics of a crystal, it is shown, for instance in [45], that a general elastic tensor has 21 independent components. The latter number, however, can be reduced if the symmetry of the crystal is taken into account. Such an analysis can be performed using several methods described in [45]. The most general one is the method of direct inspection. According to this method, one has to perform the following three steps for each symmetry operation (SymOp) from the spacegroup of the crystal:

1. Derive the mapping matrix (a_{ij}) from $(x_1', x_2', x_3') = \mathrm{SymOp}((x_1, x_2, x_3))$;
2. Calculate $\tilde{C}_{ijkl} = a_{im}a_{jn}a_{ko}a_{lp}C_{mnop}$;
3. Solve $\tilde{C}_{ijkl} = C_{ijkl}$.

The second step can be simplified by utilization of the fact, that the transformation law for the components of a tensor of rank n ($T_{i_1 i_2 \ldots i_n}$) are the same as for the products of of type $x_{i_1}x_{i_2}\ldots x_{i_n}$. Applying the method of direct inspection, one can identify the independent components for all crystal systems. These results are presented in the following section, that is completely adopted from [45].

A.2 Results for all crystal systems

KEY TO NOTATION

	·	zero component
	●	non-zero component
	●—●	equal components
	●—○	components numerically equal, but opposite in sign
For s	◉	twice the numerical equal of the heavy dot component to which it is joined
For c	◉	the numerical equal of the heavy dot component to which it is joined
For s	×	$2\,(s_{11} - s_{12})$
For c	×	$\frac{1}{2}\,(c_{11} - c_{12})$

All the matrices are symmetrical about the leading diagonal.

Crystal system	Class	Components	Diagram
Triclinic	Both classes	21	$\begin{pmatrix} \bullet & \bullet & \bullet & \bullet & \bullet & \bullet \\ & \bullet & \bullet & \bullet & \bullet & \bullet \\ & & \bullet & \bullet & \bullet & \bullet \\ & & & \bullet & \bullet & \bullet \\ & & & & \bullet & \bullet \\ & & & & & \bullet \end{pmatrix}$
Monoclinic	All classes	13	Diad $\parallel x_2$ (standard) $\begin{pmatrix} \bullet & \bullet & \bullet & \cdot & \bullet & \cdot \\ & \bullet & \bullet & \cdot & \bullet & \cdot \\ & & \bullet & \cdot & \bullet & \cdot \\ & & & \bullet & \cdot & \bullet \\ & & & & \bullet & \cdot \\ & & & & & \bullet \end{pmatrix}$ Diad $\parallel x_3$ $\begin{pmatrix} \bullet & \bullet & \bullet & \cdot & \cdot & \bullet \\ & \bullet & \bullet & \cdot & \cdot & \bullet \\ & & \bullet & \cdot & \cdot & \bullet \\ & & & \bullet & \bullet & \cdot \\ & & & & \bullet & \cdot \\ & & & & & \bullet \end{pmatrix}$

Crystal system	Class	Components	Diagram
Orthorombic	All classes	9	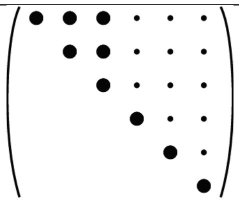
Tetragonal	Classes $4, \bar{4}, 4/m$	7	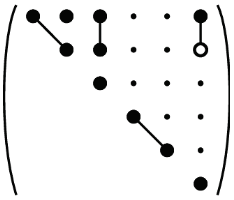
	Classes $4mm, \bar{4}2m,$ $422, 4/mmm$	6	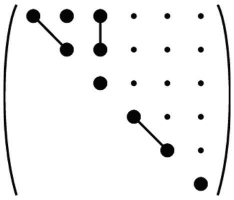
Trigonal	Classes $3, \bar{3}$	7	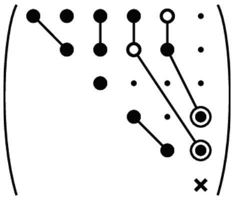
	Classes $32, \bar{3}m, 3m$	6	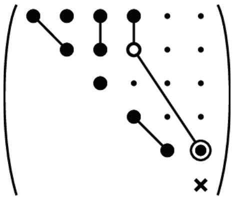
Hexagonal	All classes	5	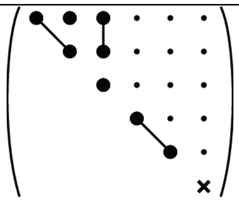
Cubic	All classes	3	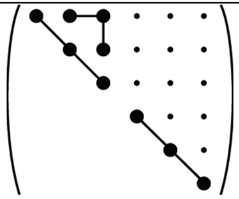

Crystal system	Class	Components	Diagram
Isotropic		2	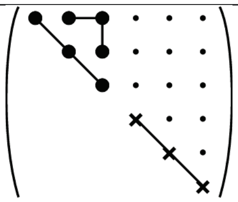

Acknowledgement

There are many people I'd like to express my gratitude to, who helped me to conduct the research and to write this thesis. First of all, I'd like to thank my supervisor Prof. Claudia Draxl for scientific guidance, steady support, and for creating a special environment in her group – scientifically demanding, but very friendly and inspiring. Second, I'd like to thank Jürgen Spitaler for fruitful scientific discussions, careful reading of my thesis and giving kindly the suggestions for its improvement. I'd like to thank all people, who were, at some time, members of the Chair for Atomistic Modeling and Design of Materials (AMDM) at the University of Leoben for the great friendly atmosphere, that made my PhD time a family-like experience. Especially, I'd like to thank Hojjat Gholizadeh for many hours of discussions – scientific and not so much, and for being a good friend.

I'd like also to express my gratitude to my experimental colleagues – Claudia Walter, Josef Keckes, and Prof. Christian Mitterer – for pleasant and productive collaboration.

This work was carried out in the framework of the Competence Center for Excellent Technologies (COMET) on Integrated Research in Materials, Processing and Product Engineering, financed by the Austrian Federal Government and the Styrian Provincial Government.

Finally, I'd like to thank my parents and my wife, whose love and support are simply invaluable.

List of Abbreviations

DFT	Density Functional Theory
EELS	Electron Energy Loss Spectroscopy
STEM	Scanning Transmission Electron Microscopy
STO	$SrTiO_3$
LAO	$LaAlO_3$
XAS	X-ray Absorption Spectroscopy
RPES	Resonant PhotoEmission Spectroscopy
HR-TEM	High-Resolution Transmission Electron Microscopy
LTE	Linear Thermal Expansion
LDA	Local-Density Approximation
GGA	Generalized Gradient Approximation
PW91	Perdew-Wang GGA
PBE	Perdew-Burke-Ernzerhof GGA
revPBE	Zhang-Yang revised PBE GGA
RPBE	Hammer-Hansen-Nørskov revised PBE GGA
PBEsol	Revised PBE GGA for solids and surfaces
XRD	X-ray diffraction
RRKJ	Rappe-Rabe-Kaxiras-Joannopoulos pseudoization scheme
PW	Plane-Wave
A_1	single Al-terminated (001) surface of α-Al_2O_3
A_2	O-terminated (001) surface of α-Al_2O_3
A_3	double Al-terminated (001) surface of α-Al_2O_3
T_1	single O-terminated (100) surface of rutile-TiO_2
T_2	Ti-terminated (100) surface of rutile-TiO_2
T_3	double O-terminated (100) surface of rutile-TiO_2

CSL	Coincidence-Site Lattice
PES	Potencial Energy Surface
BFGS	Broyden-Fletcher-Goldfarb-Shanno formula
IF	InterFace
RDF	Radial Distribution Function
BZ	Brillouin Zone
IBZ	Irreducible Brillouin Zone
SL	SuperLattice
AS	Alumina Slab
TS	Titania Slab
PAC	Plane-Averaged Charge distribution
ICT	Integral Charge Transfer
DOS	Density Of States
PDOS	Partial Density Of States
LDOS	Local Density Of States
GN	Grimsditch-Nizzoli method

List of Figures

3.1 The electric current density and the electric field in conductors . . 11
3.2 Unit cube in a homogeneously stressed body 14
3.3 The deformation of an extendible string 15
3.4 The displacement u as a function of x in an extended string . . . 15
3.5 Two-dimensional strain. 16
3.6 Decomposition of a general deformation 17

4.1 Epitaxy of rutile on sapphire 26
4.2 Unit-cell of α-Al_2O_3 28
4.3 Unit-cell of rutile-TiO_2 28
4.4 Atomic layer stacking in α-Al_2O_3 and in rutile-type TiO_2 31

5.1 1D illustration of the *stress balancing* approach 36
5.2 Setup for illustration of the *stress balancing* method 37

6.1 Relaxation of supercell structures 44
6.2 Relaxation profiles of the A_2-T_2 (left) and the A_3-T_3 (right) structures. The sketch of A_3-T_3 (top right) is intentionally compressed along the vertical axis to make the whole figure compact. 46
6.3 Coordination polyhedron: a two-dimensional example 47
6.4 Coordination polyhedra in TiO_2 and Al_2O_3 48
6.5 Calculation of radial distribution function in 2D 49
6.6 Layer-averaged RDF of O-atoms around M-atoms 50
6.7 O-Al-O valence angles in Al_2O_3 51
6.8 Distribution of O-Al-O valence angles 52
6.9 Distribution of O-Ti-O valence angles 52
6.10 Distributions of minimal and maximal angles 53

7.1 The work of separation and the BZ-sampling 58
7.2 The work of separation and the cut-off energy 59
7.3 Components of the relaxation energy 62
7.4 Surface geometries of relaxed rutile 63
7.5 The work of separation and slab thickness (corrected) 64

8.1 Plane-averaged charge of the relaxed structures 68
8.2 Work of separation and integral charge transfer 69
8.3 Total electronic density of states 70
8.4 LDOS of the A_2-T_2 72
8.5 Interface-induced electronic state 73
8.6 Layer-averaged Löwdin charges of A_2-T_2 74
8.7 Hubbard U and the total DOS of A_2-T_2 76

9.1 Dummy strain-response curve 81
9.2 Hydrostatic stress acting on a cube 83
9.3 Volume-pressure dependency calculated for A_2-T_2. 84
9.4 Scatter plot of $\{V_0, B_0\}$ points obtained after fitting 85
9.5 Calculated B_0 and the degree of the fitting polynomial 85
9.6 The result of fitting V-P ab-initio data 86
9.7 Tensile stress acting on a cube 87
9.8 Stress-components versus tensile strain 88
9.9 Scatter plot of $\{\varepsilon_0, E_0\}$ data obtained by fitting 89
9.10 Young's modulus and the degree of a fitting polynomial 90
9.11 Results of fitting the *ab initio* data (Young's modulus) 90
9.12 Shear stress acting on a cube 91
9.13 Stress-components versus shear strain 92
9.14 Scatter plot of $\{\varepsilon_0, G_0\}$ data obtained by fitting 93
9.15 G_0 and the degree of the fitting polynomial 94
9.16 Results of fitting the *ab initio* data (shear modulus) 95

List of Tables

2.1 Properties of metallic hard materials 6
2.2 Properties of covalent hard materials 7
2.3 Properties of ionic (ceramic) hard materials 7

3.1 Some examples of second-rank tensors 12
3.2 Transformation laws for tensors [45] 13
3.3 Relationships between tensor and matrix indices 19

4.1 Computational parameters. 26
4.2 Phases of alumina (Al_2O_3) 27
4.3 Wyckoff positions of atoms in the primitive unit-cell of α-Al_2O_3 . 29
4.4 Lattice parameters of bulk α-Al_2O_3 29
4.5 Elastic constants of bulk α-Al_2O_3 30
4.6 Phases of titania (TiO_2) 30
4.7 Wyckoff positions of atoms in the primitive unit-cell of rutile-TiO_2 30
4.8 Lattice parameters of bulk rutile-TiO_2 31
4.9 Elastic constants of bulk rutile-TiO_2 31

5.1 The lattice misfit at the interface 41
5.2 Supercell parameters leading to minimal strain energy 41

6.1 Optimal inter-slab separations (Δ) for different stacking. 43

7.1 The ideal work of separation 56
7.2 The *static* work of separation and slab thickness 60
7.3 The work of separation and slab thickness 61
7.4 The relaxation energies and slab thickness 62

9.1 Elastic moduli of the A_2-T_2 superlattice 96

Bibliography

[1] K. A. Marino, B. Hinnemann, E. A. Carter, *Proceedings of the National Academy of Sciences* **108**, 5480 (2011).

[2] S. Mileiko, V. Kazmin, V. Kiiko, A. Rudnev, *Composites Science and Technology* **57**, 1363 (1997).

[3] D.-H. Kuo, W. M. Kriven, T. J. Mackin, *Journal of the American Ceramic Society* **80**, 2987 (1997).

[4] T. Radsick, B. Saruhan, H. Schneider, *Journal of the European Ceramic Society* **20**, 545 (2000).

[5] R. J. Kerans, R. S. Hay, T. A. Parthasarathy, M. K. Cinibulk, *Journal of the American Ceramic Society* **85**, 2599 (2002).

[6] N. Browning, D. Wallis, P. Nellist, S. Pennycook, *Micron* **28**, 333 (1997).

[7] Q.-H. Wu, *Critical Reviews in Solid State and Materials Sciences* **36**, 1 (2011).

[8] E. Dickey, V. Dravid, P. Nellist, D. Wallis, S. Pennycook, *Acta Materialia* **46**, 1801 (1998).

[9] E. Dickey, X. Fan, S. Pennycook, *Acta Materialia* **47**, 4061 (1999).

[10] S. Pennycook, E. Dickey, P. Nellist, M. Chisholm, Y. Yan, S. Pantelides, *Journal of the European Ceramic Society* **19**, 2211 (1999).

[11] C.-X. Guo, O. Warschkow, D. E. Ellis, V. P. Dravid, E. C. Dickey, *Journal of the American Ceramic Society* **84**, 2677 (2001).

[12] D. C. Sayle, S. Andrada Maicaneanu, B. Slater, C. Richard A. Catlow, *J. Mater. Chem.* **9**, 2779 (1999).

[13] P. Moller, S. Komolov, E. Lazneva, *Surface Science* **425**, 15 (1999).

[14] P. Casek, F. Finocchi, C. Noguera, *Phys. Rev. B* **72**, 205308 (2005).

[15] V. K. Lazarov, S. A. Chambers, M. Gajdardziska-Josifovska, *Phys. Rev. Lett.* **90**, 216108 (2003).

[16] V. K. Lazarov, M. Weinert, S. A. Chambers, M. Gajdardziska-Josifovska, *Phys. Rev. B* **72**, 195401 (2005).

[17] H. Huang, S. Luo, K. Yao, *Computational Materials Science* **50**, 198 (2010).

[18] K. Pande, M. Gajdardziska-Josifovska, M. Weinert, *Phys. Rev. B* **86**, 035431 (2012).

[19] R. Klie, Y. Zhu, *Micron* **36**, 219 (2005).

[20] E. A. A. Jarvis, E. A. Carter, *Journal of the American Ceramic Society* **86**, 373 (2003).

[21] S. Chambers, J. Williams, M. Henderson, A. Joly, M. Varela, S. Pennycook, *Surface Science* **587**, L197 (2005).

[22] A. V. Ramos, J.-B. Moussy, M.-J. Guittet, M. Gautier-Soyer, C. Gatel, P. Bayle-Guillemaud, B. Warot-Fonrose, E. Snoeck, *Phys. Rev. B* **75**, 224421 (2007).

[23] H. S. Nabi, R. J. Harrison, R. Pentcheva, *Phys. Rev. B* **81**, 214432 (2010).

[24] A. R. Akbashev, V. V. Roddatis, A. L. Vasiliev, S. Lopatin, V. A. Amelichev, A. R. Kaul, *Sci. Rep.* **2** (2012).

[25] N. C. Bristowe, P. B. Littlewood, E. Artacho, *Phys. Rev. B* **83**, 205405 (2011).

[26] C. Cancellieri, D. Fontaine, S. Gariglio, N. Reyren, A. D. Caviglia, A. Fête, S. J. Leake, S. A. Pauli, P. R. Willmott, M. Stengel, P. Ghosez, J.-M. Triscone, *Phys. Rev. Lett.* **107**, 056102 (2011).

[27] W. S. Choi, C. M. Rouleau, S. S. A. Seo, Z. Luo, H. Zhou, T. T. Fister, J. A. Eastman, P. H. Fuoss, D. D. Fong, J. Z. Tischler, G. Eres, M. F. Chisholm, H. N. Lee, *Advanced Materials* **24**, 6423 (2012).

[28] N. C. Bristowe, T. Fix, M. G. Blamire, P. B. Littlewood, E. Artacho, *Phys. Rev. Lett.* **108**, 166802 (2012).

[29] M. Stengel, D. Vanderbilt, *Phys. Rev. B* **80**, 241103 (2009).

[30] P. Zubko, S. Gariglio, M. Gabay, P. Ghosez, J.-M. Triscone, *Annual Review of Condensed Matter Physics* **2**, 141 (2011).

[31] D. Mitchell, D. Attard, K. Finnie, G. Triani, C. Barbe, C. Depagne, J. Bartlett, *Applied Surface Science* **243**, 265 (2005).

[32] P. Laha, A. Panda, S. Mahapatra, P. Barhai, A. Das, I. Banerjee, *Applied Surface Science* **258**, 2275 (2012).

[33] C. A. Freyman, Y.-W. Chung, *Surface and Coatings Technology* **202**, 4702 (2008).

[34] C. E. Kim, I. Yun, *Applied Surface Science* **258**, 3089 (2012).

[35] M. Sanchez-Agudo, L. Soriano, C. Quiros, J. Avila, J. Sanz, *Surface Science* **482 - 485**, 470 (2001).

[36] M. Sanchez-Agudo, L. Soriano, C. Quiros, L. Roca, V. Perez-Dieste, J. Sanz, *Surface Science* **507 - 510**, 672 (2002).

[37] L. Soriano, M. Sanchez-Agudo, R. Mossanek, M. Abbate, G. Fuentes, P. Bressler, L. Alvarez, J. Mendez, A. Gutierrez, J. Sanz, *Surface Science* **605**, 539 (2011).

[38] J. Y. Huang, B. H. Park, D. Jan, X. Q. Pan, Y. T. Zhuk, Q. X. Jia, *Philosophical Magazine A* **82**, 735 (2002).

[39] R. Engel-Herbert, B. Jalan, Jo *Journal of Crystal Growth* **312**, 149 (2009).

[40] M. Grimsditch, *Phys. Rev. B* **31**, 6818 (1985).

[41] M. Grimsditch, F. Nizzoli, *Phys. Rev. B* **33**, 5891 (1986).

[42] R. Bunshah, *Handbook of Hard Coatings: Deposition Technologies, Properties and Applications*, Materials Science and Process Technology Series (Noyes Publications, 2001).

[43] S. Zhang, D. Sun, Y. Fu, H. Du, *Surface and Coatings Technology* **167**, 113 (2003).

[44] H. Holleck, *Journal of Vacuum Science* & *Technology A: Vacuum, Surfaces, and Films* **4**, 2661 (1986).

[45] J. Nye, *Physical properties of crystals: their representation by tensors and matrices*, Oxford science publications (Clarendon Press, 1985).

[46] G. B. Arfken, H. J. Weber, *Mathematical Methods For Physicists* (Academic Press, 2005).

[47] R. Sharipov, *ArXiv Mathematics e-prints* (2004).

[48] W. Kohn, *Rev. Mod. Phys.* **71**, 1253 (1999).

[49] P. Hohenberg, W. Kohn, *Phys. Rev.* **136**, B864 (1964).

[50] W. Kohn, L. J. Sham, *Phys. Rev.* **137**, A1697 (1965).

[51] D. M. Ceperly, *Phys. Rev. B* **18**, 3126 (1978).

[52] D. M. Ceperly, B. J. Alder, *Phys. Rev. Lett.* **45**, 566 (1980).

[53] J. P. Perdew, S. Kurth, *A Primer in Density Functional Theory* (Springer, Berlin, 2003).

[54] J. Perdew, *Electronic Structure of Solids '91* (Akademie Verlag, Berlin, 1991), vol. 17 of *Physical Research*, chap. Unified theory of exchange and correlation beyond the local density approximation, pp. 11–20.

[55] J. P. Perdew, K. Burke, M. Ernzerhof, *Phys. Rev. Lett.* **77**, 3865 (1996).

[56] J. P. Perdew, A. Ruzsinszky, G. I. Csonka, O. A. Vydrov, G. E. Scuseria, L. A. Constantin, X. Zhou, K. Burke, *Phys. Rev. Lett.* **100**, 136406 (2008).

[57] Y. Zhang, W. Yang, *Phys. Rev. Lett.* **80**, 890 (1998).

[58] B. Hammer, L. B. Hansen, J. K. Norskov, *Phys. Rev. B* **59**, 7413 (1999).

[59] A. D. Becke, *Phys. Rev. A* **38**, 3098 (1988).

[60] J. P. Perdew, *Phys. Rev. B* **33**, 8822 (1986).

[61] C. Lee, W. Yang, R. G. Parr, *Phys. Rev. B* **37**, 785 (1988).

[62] J. P. Perdew, J. A. Chevary, S. H. Vosko, K. A. Jackson, M. R. Pederson, D. J. Singh, C. Fiolhais, *Phys. Rev. B* **46**, 6671 (1992).

[63] B. Grabowski, T. Hickel, J. Neugebauer, *Phys. Rev. B* **76**, 024309 (2007).

[64] J. Tao, al., *Phys. Rev. Lett.* **91**, 146401 (2003).

[65] R. Armiento, A. E. Mattsson, *Phys. Rev. B* **72**, 085108 (2005).

[66] J. Heyd, G. E. Scuseria, M. Ernzerhof, *J. Chem. Phys.* **118**, 8207 (2003).

[67] A. D. Becke, *The Journal of Chemical Physics* **98**, 5648 (1993).

[68] P. J. Stephens, F. J. Devlin, C. F. Chabalowski, M. J. Frisch, *The Journal of Physical Chemistry* **98**, 11623 (1994).

[69] Department of Physical Metallurgy and Materials Testing, University of Leoben, Franz-Josef-Straße 18, A-8700 Leoben, Austria.

[70] Chair of Functional Materials and Materials Systems (FMMS), University of Leoben, Franz-Josef-Straße 18, A-8700 Leoben, Austria.

[71] Department of Materials Physics, University of Leoben, Franz-Josef-Straße 18, A-8700 Leoben, Austria.

[72] Erich Schmid Institute for Materials Science, Austrian Academy of Sciences, Jahnstraße 12, A-8700 Leoben, Austria.

[73] M. N. Popov, J. Spitaler, M. Mühlbacher, C. Walter, J. Keckes, C. Mitterer, C. Draxl, *Phys. Rev. B* **86**, 205309 (2012).

[74] A. Kokalj, *Computational Materials Science* **28**, 155 (2003). Proceedings of the Symposium on Software Development for Process and Materials Design.

[75] M. C. Payne, M. P. Teter, D. C. Allan, T. A. Arias, J. D. Joannopoulos, *Rev. Mod. Phys.* **64**, 1045 (1992).

[76] N. W. Ashcroft, *Solid State Physics* (Saunders College Publishing, Forth Worth, Philadelphia, San Diego, USA, 1976). ISBN 0-03-083993-9.

[77] P. Giannozzi, S. Baroni, N. Bonini, M. Calandra, R. Car, C. Cavazzoni, D. Ceresoli, G. L. Chiarotti, M. Cococcioni, I. Dabo, A. D. Corso, S. de Gironcoli, S. Fabris, G. Fratesi, R. Gebauer, U. Gerstmann, C. Gougoussis, A. Kokalj, M. Lazzeri, L. Martin-Samos, N. Marzari, F. Mauri, R. Mazzarello, S. Paolini, A. Pasquarello, L. Paulatto, C. Sbraccia, S. Scandolo, G. Sclauzero, A. P. Seitsonen, A. Smogunov, P. Umari, R. M. Wentzcovitch, *Journal of Physics: Condensed Matter* **21**, 395502 (2009).

[78] J. P. Perdew, K. Burke, M. Ernzerhof, *Phys. Rev. Lett.* **77**, 3865 (1996).

[79] A. M. Rappe, K. M. Rabe, E. Kaxiras, J. D. Joannopoulos, *Phys. Rev. B* **41**, 1227 (1990).

[80] A. M. Rappe, K. M. Rabe, E. Kaxiras, J. D. Joannopoulos, *Phys. Rev. B* **44**, 13175 (1991).

[81] W. Pies, A. Weiss, vol. 7b1 of *Landolt-Börnstein - Group III Condensed Matter*, chap. b108, II.1.1 Simple oxides.

[82] `http://www.cryst.ehu.es/cgi-bin/cryst/programs/nph-wp-list?gnum=167&grha=rhombohedral`.

[83] J. Lewis, D. Schwarzenbach, H. D. Flack, *Acta Crystallographica Section A* **38**, 733 (1982).

[84] M. Oetzel, G. Heger, *Journal of Applied Crystallography* **32**, 799 (1999).

[85] T. Kurita, K. Uchida, A. Oshiyama, *Phys. Rev. B* **82**, 155319 (2010).

[86] R. Yu, J. Zhu, H. Ye, *Computer Physics Communications* **181**, 671 (2010).

[87] H. Yao, L. Ouyang, W.-Y. Ching, *Journal of the American Ceramic Society* **90**, 3194 (2007).

[88] E. H. Kisi, C. J. Howard, J. Zhang, *Journal of Applied Crystallography* **44**, 216 (2011).

[89] J. R. Gladden, J. H. So, J. D. Maynard, P. W. Saxe, Y. L. Page, *Applied Physics Letters* **85**, 392 (2004).

[90] W. Pies, A. Weiss, vol. 7b1 of *Landolt-Börnstein - Group III Condensed Matter*, chap. b726, II.1.1 Simple oxides.

[91] `http://www.cryst.ehu.es/cgi-bin/cryst/programs/nph-wp-list?gnum=136`.

[92] R. Restori, D. Schwarzenbach, J. R. Schneider, *Acta Crystallographica Section B* **43**, 251 (1987).

[93] K. Sugiyama, Y. Takuchi, *Zeitschrift für Kristallographie* **194**, 305 (1991).

[94] H. Perron, C. Domain, J. Roques, R. Drot, E. Simoni, H. Catalette, *Theor. Chem. Acc.* **117**, 565 (2007).

[95] M. H. Grimsditch, A. K. Ramdas, *Phys. Rev. B* **14**, 1670 (1976).

[96] D. Andeen, F. Lange, *Int. J. Mater. Res.* **98**, 1222 (2007).

[97] B. C. Bolding, E. A. Carter, *Molecular Simulation* **9**, 269 (1992).

[98] E. Bauer, J. H. van der Merwe, *Phys. Rev. B* **33**, 3657 (1986).

[99] J. H. van der Merwe, E. Bauer, D. L. Tönsing, P. M. Stoop, *Phys. Rev. B* **49**, 2127 (1994).

[100] J. H. van der Merwe, E. Bauer, D. L. Tönsing, P. M. Stoop, *Phys. Rev. B* **49**, 2137 (1994).

[101] S. C. Erwin, C. Gao, C. Roder, J. Lähnemann, O. Brandt, *Phys. Rev. Lett.* **107**, 026102 (2011).

[102] B. C. Bolding, E. A. Carter, *Molecular Simulation* **9**, 269 (1992).

[103] C. G. Van de Walle, R. M. Martin, *Phys. Rev. B* **34**, 5621 (1986).

[104] R. Fletcher, *Practical Methods of Optimization* (John Wiley and Sons, 1987).

[105] I. G. Batyrev, A. Alavi, M. W. Finnis, *Phys. Rev. B* **62**, 4698 (2000).

[106] H. J. Monkhorst, J. D. Pack, *Phys. Rev. B* **13**, 5188 (1976).

[107] D. Sholl, J. Steckel, *Density Functional Theory: A Practical Introduction* (Wiley, 2009).

[108] P. Löwdin, *J. Chem. Phys.* **18**, 365 (1950).

[109] R. S. Mulliken, *The Journal of Chemical Physics* **23**, 1833 (1955).

[110] R. F. W. Bader, *Atoms in Molecules: A Quantum Theory (International Series of Monographs on Chemistry)* (Oxford University Press, USA, 1994).

[111] K. C. Gross, P. G. Seybold, C. M. Hadad, *International Journal of Quantum Chemistry* **90**, 445 (2002).

[112] V. I. Anisimov, J. Zaanen, O. K. Andersen, *Phys. Rev. B* **44**, 943 (1991).

[113] V. I. Anisimov, I. V. Solovyev, M. A. Korotin, M. T. Czyżyk, G. A. Sawatzky, *Phys. Rev. B* **48**, 16929 (1993).

[114] I. V. Solovyev, P. H. Dederichs, V. I. Anisimov, *Phys. Rev. B* **50**, 16861 (1994).

[115] A. I. Liechtenstein, V. I. Anisimov, J. Zaanen, *Phys. Rev. B* **52**, R5467 (1995).

[116] V. I. Anisimov, F. Aryasetiawan, A. I. Lichtenstein, *Journal of Physics: Condensed Matter* **9**, 767 (1997).

[117] W. E. Pickett, S. C. Erwin, E. C. Ethridge, *Phys. Rev. B* **58**, 1201 (1998).

[118] M. Cococcioni, S. de Gironcoli, *Phys. Rev. B* **71**, 035105 (2005).

[119] M. E. A. de Dompablo, A. Morales-García, M. Taravillo, *The Journal of Chemical Physics* **135**, 054503 (2011).

[120] J. Stausholm-Møller, H. H. Kristoffersen, B. Hinnemann, G. K. H. Madsen, B. Hammer, *The Journal of Chemical Physics* **133**, 144708 (2010).

[121] G. Mattioli, P. Alippi, F. Filippone, R. Caminiti, A. Amore Bonapasta, *The Journal of Physical Chemistry C* **114**, 21694 (2010).

[122] M. Farnesi Camellone, P. M. Kowalski, D. Marx, *Phys. Rev. B* **84**, 035413 (2011).

[123] B. M. Davis, D. N. Seidman, A. Moreau, J. B. Ketterson, J. Mattson, M. Grimsditch, *Phys. Rev. B* **43**, 9304 (1991).

[124] R. S. Jones, J. A. Slotwinski, J. W. Mintmire, *Phys. Rev. B* **45**, 13624 (1992).

[125] C. Arcangeli, F. Nizzoli, A. I. Liechtenstein, *Phys. Rev. B* **51**, 4497 (1995).

[126] S. Papadia-Einarsson, *Phys. Rev. B* **55**, 10057 (1997).

[127] F. Martin, C. Jaouen, J. Pacaud, G. Abadias, P. Djemia, F. Ganot, *Phys. Rev. B* **71**, 045422 (2005).

[128] A. de Bernabe, R. Jimenez, M. Garcia-Hernandez, C. Prieto, *Thin Solid Films* **317**, 255 (1998).

[129] A. de Bernabe, C. Prieto, D. Caceres, I. Vergara, A. Every, H. Fischer, *physica status solidi (a)* **188**, 1023 (2001).

[130] D. Wolf, J. F. Lutsko, *Phys. Rev. Lett.* **60**, 1170 (1988).

[131] R. Golesorkhtabar, P. Pavone, J. Spitaler, P. Puschnig, C. Draxl, *Comp. Phys. Comm.* (submitted).

[132] R. R. Picard, R. D. Cook, *Journal of the American Statistical Association* **79**, 575 (1984).

[133] H. A. Martens, P. Dardenne, *Chemometrics and Intelligent Laboratory Systems* **44**, 99 (1998).

[134] R. Golesorkhtabar, P. Pavone, J. Spitaler, P. Puschnig, C. Draxl, *Computer Physics Communications* (2013).

[135] R. M. Wentzcovitch, *Phys. Rev. B* **44**, 2358 (1991).

List of Publications

The list comprises a number of publications that have been written during the development of this thesis. They can be considered as a supplementary material to the results presented in the thesis.

[P-1] M.N. Popov, J. Spitaler, M. Mühlbacher, C. Walter, J. Keckes, C. Mitterer, C. Draxl, *Phys. Rev. B* **86**, 205309 (2012).

The results of this work have also been presented at the following conferences:

[C-1] ECCOMAS, Vienna, Austria, 2012

[C-2] 15th International Workshop on Computational Physics & Materials Science: Total Energy & Force Methods, Trieste, Italy, 2011

[C-3] Psi-k Conference, Berlin, Germany, 2010

[C-4] DPG Spring meeting, Regensburg, Germany, 2010